THE EFFECTS OF TRAILING EDGE BLUNTNESS ON AIRFOIL PERFORMANCE AS CALCULATED APPROXIMATELY BY A VISCID-INVISCID VORTEX PANEL METHOD

by

Michael R. D'Angelo

B.S., Mechanical Engineering

University of New Hampshire, 1985

SUBMITTED TO THE DEPARTMENT OF AERONAUTICS AND ASTRONAUTICS

IN PARTIAL FULFILLMENT OF THE REQUIREMENTS FOR THE DEGREE OF

MASTER OF SCIENCE

in

AERONAUTICS AND ASTRONAUTICS

at the

MASSACHUSETTS INSTITUTE OF TECHNOLOGY

DECEMBER 1988

Signature of Author _____

Department of Aeronautics and Astronautics
December 20, 1988

Certified by _____

Professor Eugene E. Covert
Head, Department of Aeronautics and Astronautics
Thesis Supervisor

Accepted by _____

Professor Harold Y. Wachman
Chairman, Department Graduate Committee

THE EFFECTS OF TRAILING EDGE BLUNTNESS ON AIRFOIL PERFORMANCE AS CALCULATED APPROXIMATELY BY A VISCID-INVISCID VORTEX PANEL METHOD

by

Michael R. D'Angelo

SUBMITTED TO THE DEPARTMENT OF AERONAUTICS AND ASTRONAUTICS
IN PARTIAL FULFILLMENT OF THE REQUIREMENTS FOR THE DEGREE OF
MASTER OF SCIENCE IN AERONAUTICS AND ASTRONAUTICS

ABSTRACT

Recognizing that sharp/cusped trailing edge geometries are often physically impracticle from a manufacturing and maintenance viewpoint, the current analysis examines the alternative case of blunt trailing edge geometry and shows that by introducing moderate degrees of trailing edge bluntness to a reference airfoil section, the lift is not significantly reduced.

The analysis is carried out with a two-dimensional viscid-inviscid vortex panel method designed to model the structure of the laminar and turbulent flow regions, including transition, separation, reattachment and wake closure, for low Reynolds-number cases. The approximate integral methods due to Thwaites and Head are employed in the calculation of the laminar and turbulent boundary layers, respectively. Laminar separation-reattachment criteria due to Owen and Klanfer and transition criteria due to Michel are also employed.

The results show that at a chord based Reynolds-number of 700,000, A NACA 0012 airfoil section cut off at 95 percent of the chord experiences only fractional losses in lift for angles-of-attack between 0 and 10 degrees. The resulting trailing edge thickness is increased from 0.252 percent of the chord to 1.614 percent, yielding a physically more practical airfoil design.

Thesis Supervisor: Professor Eugene E. Covert
Head, Department of Aeronautics and Astronautics

To the memory

of my grandparents

John & Anna

Acknowledgements

I would like to thank Professor Eugene E. Covert, my thesis advisor, for his continued support and guidance during the preparation of my thesis. I appreciate the time he has taken to provide me with this opportunity as well as his willingness and availability to discuss my work.

In addition, I would like to thank Professor Judson R. Baron, my academic advisor, for his time and efforts in addressing matters related to the baseline flow model.

Acknowledgements should also be extended to Don Robinson for introducing me to the core program from which I initiated my research.

Finally, I would like to thank Professor Baron and Mr. Frank H. Durgin for providing me with the opportunity to work as a research assistant at the Wright Brothers Wind Tunnel. I was able to learn a great deal from their expertise in experimental methods.

Contents

List of Figures

15. Convergence of the skin friction coefficient, c_f, method of steepest descent, NACA 0012, AOA= 4°, Re=700,000, at mid-chord point.

16. Sensitivity of shape factor, H, to Thwaites' lambda, λ, from CEBECI & BRADSHAW [ref 5].

17. Effect of smoothing on laminar displacement thickness, δ^*, NACA 0012, AOA= 4°, Re=700,000.

18. Sensitivity of lift coefficient, c_ℓ, to varying numbers of uniformly distributed wing-wake panels, NACA 0012, AOA= 4°, Re=700,000, fully attached.

19. Sensitivity of lift coefficient, c_ℓ, to varying numbers of uniformly distributed wing-wake panels, NACA 0012, AOA= 4°, Re=700,000, forced separation at 90 % of the chord.

20. *Wake factor* as a function of airfoil thickness, from MASKEW & DVORACK [ref 17].

21. Reference sketch for the calculation of wake length.

22. Typical jet boundary.

23. Jet boundary analogy to leading-trailing edge flow sepration.

24. Panelled body surface with separation.

25. Lift coefficient, c_ℓ, sensitivity to maximum panel through-flow.

26. Final wing-wake panel configuration.

27. Predicted curve of lift coefficient, c_ℓ, versus angle-of-attack, NACA 0012, Re=125,000.

28. Predicted curve of lift coefficient, c_ℓ, versus angle-of-attack, NACA 0012, Re=400,000.

29. Predicted and experimental curves of lift coefficient, c_ℓ, versus angle-of-attack, NACA 0012, Re=700,000.

30. Predicted and experimental curves of lift coefficient, c_ℓ, versus angle-of-attack, NACA 0012, Re=1,000,000.

31. Predicted curves of lift coefficient, c_ℓ, versus angle-of-attack, NACA 0012, Re=125,000, 400,000, 7000,000 and 1,000,000.

32. Chordwise distribution of shape factor, H, NACA 0012, AOA= 10°, Re=700,000.

33. Chordwise distribution of momentum thickness, θ, NACA 0012, AOA= 10°, Re=700,000.

34. Chordwise distribution of displacement thickness, δ^*, NACA 0012, AOA= 4°, Re=700,000.

35. Wake shape, NACA 0012, AOA= 16°, Re=700,000.

36. Pressure distribution, NACA 0012, AOA= 16°, Re=700,000.

37. Effect of reattaching laminar separation bubble on pressure distribution, NACA 0012, AOA= 2°, Re=700,000.

38. Pressure distribution with trailing edge separation, NACA 0012, AOA= 10°, Re=1,000,000.

39. Pressure distribution with leading edge separation, NACA 0012, AOA= 16°, Re=1,000,000.

40. Chordwise separation location, x_{sep}, versus angle-of-attack as a function of Reynolds number, NACA 0012.

41. Distribution of displacement thickness, δ^*, as a function of Reynolds number, NACA 0012, AOA= 2°.

42. Lift coefficient, $[c_\ell]_{ref-100}$, (referenced to full section) versus angle-of-attack as a function of trailing edge bluntness, NACA 0012 reference, Re=700,000.

43. Moment coefficient, $[c_{m_{l.e.}}]_{ref-100}$, (referenced to full section) versus angle-of-attack as a function of trailing edge bluntness, NACA 0012 reference, Re=700,000.

44. Lift coefficient, c_ℓ, (referenced to reduced chord) versus angle-of-attack as a function of trailing edge bluntness, NACA 0012 reference, Re=700,000.

45. Moment coefficient, $c_{m_{l.e.}}$, (referenced to reduced chord) versus angle-of-attack as a function of trailing edge bluntness, NACA 0012 reference, Re=700,000.

46. Separation location, $x[_{sep}]_{ref-100}$, (referenced to full section) versus angle-of-attack as a function of trailing edge bluntness, NACA 0012 reference, Re=700,000.

47. Separation location, x_{sep}, (referenced to actual reduced chord) versus angle-of-attack as a function of trailing edge bluntness, NACA 0012 reference, Re=700,000.

48. Wake shapes, NACA 0012, Re=700,000, AOA= 2° - 16°.

49. Pressure distributions, $c_p(x)$, NACA 0012, Re=700,000, AOA= 2° - 16°.

50. Wake shapes, NACA 0012, Re=1,000,000, AOA= 2° - 16°.

51. Pressure distributions, $c_p(x)$, NACA 0012, Re=1,000,000, AOA= 2° - 16°.

52. Laminar-Turbulent intermittency function, γ, for proposed transition model.

53. Experimental curves of lift coefficient, c_ℓ, versus angle-of-attack, NACA 0012, Re=700,000, from references [13] and [21].

54. Experimental curves of lift coefficient, c_ℓ, versus angle-of-attack, NACA 0012, Re=1,000,000, from references [13] and [30].

55. Lift coefficient, c_ℓ, versus Reynolds number, NACA 0012, AOA= 4°, sources as specified.

56. Lift coefficient, c_ℓ, versus Reynolds number, NACA 0012, AOA= 10°, sources as specified.

57. Lift coefficient, c_ℓ, versus Reynolds number, NACA 0012, AOA= 16°, sources as specified.

58. Flow chart of global viscid-inviscid flow model.

59. Flow chart of boundary layer routine.

Nomenclature

δ	total boundary layer thickness
δ^*	displacement thickness, $\delta^* = \int_0^\delta (1 - \frac{u}{U})dy$
H	shape factor, $H = \frac{\delta^*}{\theta}$
H_1	modified shape factor, $H_1 = \frac{\delta - \delta^*}{\theta}$
c_f	skin friction coefficient, $c_f = \frac{\tau_{wall}}{Q}$
θ	momentum thickness, $\theta = \int_0^\delta \frac{u}{U}(1 - \frac{u}{U})dy$
θ	panel rotation
τ_{wall}	wall shear stress
x, z(or y)	coordinate system
x'	distance in x direction
U_∞	undisturbed free stream velocity
U	tangential edge velocity
u, $w(orv)$	boundary layer velocities
u_ℓ, w_ℓ	local panel edge velocities
u'	perturbation velocity
γ	vortex strength per unit length
γ	intermittency function
Q	dynamic pressure, $Q = \frac{1}{2}\rho U^2$
Q	volume flow rate per unit span, $Q(x) = \int_0^\delta u dy$
ν	kinematic viscosity
λ	Thwaites lambda, $\lambda = \frac{\theta^2}{\nu}\frac{dU_{edge}}{dx}$
ℓ	Thwaites ell, $\ell = \frac{c_f U_{edge}\theta}{2\nu}$
ρ	density
p	pressure

$\mathcal{F}$	arbitrary empirical function
$\mathcal{G}$	arbitrary empirical function
Re	Reynolds number based on chord length
Re_θ	Reynolds number based on momentum thickness
Re_{δ^*}	Reynolds number based on displacement thickness
Re_x	Reynolds number based on x
V_E	turbulent entrainment velocity
D_1, D_2	distance between adjacent panel nodes
α	angle-of-attack
κ	relaxation parameter
t	airfoil thickness
c	airfoil chord
c_ℓ	section lift coefficient
$[c_\ell]_{ref-100}$	section lift coefficient referenced to 100 % section
$c_{m_{l.e.}}$	moment coefficient [leading edge]
$[c_{m_{l.e.}}]_{ref-100}$	moment coefficient [leading edge] referenced to 100 % section
x_{sep}	chordwise separation location
$[x_{sep}]_{ref-100}$	chordwise separation location referenced to 100 % section
wf	wake factor, $wf =$ [wake length]/[wake height]
$F(x)$	Stratford ratio
β	Stratford coefficient
c_p	pressure coefficient, $c_p = \frac{p-p_\infty}{Q_\infty}$
$\bar{c_p}$	equivalent pressure coefficient, $\bar{c_p} = \frac{c_p - c_{p_0}}{c_{p_0}}$
c_{p_0}	pressure coefficient at point of minimum pressure

Chapter 1

Introduction

In modelling two-dimensional, incompressible flows over common airfoil sections using classical potential flow theory, various interpretations of the Kutta condition are invoked to fix the flow condition at the trailing edge. Due to the difficulties in specifying the Kutta condition for blunt trailing edge geometries, analysis is often carried out under the assumption of a sharp trailing edge, fixing the location of the rear stagnation streamline.

When sharp trailing edge geometries are enforced, severe constraints in manufacturing and maintenance are introduced. In many cases it is physically impossible to construct the desired airfoil section resulting in varying degrees of mismatch between the predicted [theoretical] and demonstrated [experimental] performance.

Recognizing the benefits from blunt trailing edge geometries, the current paper shows that by introducing moderate degrees of trailing edge bluntness to a reference airfoil section, the lift is not significantly reduced.

The analysis is carried out with a two-dimensional vortex panel method coupled to a integral viscous boundary layer routine. Allowances are made for the development of the laminar and turbulent boundary layers, transition, laminar separation-reattachment, turbulent separation and wake length/closure. The study is conducted for moderately low

chord based Reynolds numbers [$\approx$ 700,000].

Details of the viscous solution are provided within the context of this paper while the inviscid solution is only briefly discussed.

Chapter 2

Some Comments On Boundary Layer Interactions

2.1 Effect of Viscosity on Circulation

For a typical airfoil at angle-of-attack, the boundary layer effectively imparts negative camber to the airfoil section yielding less lift at a given incidence. The negative camber, which reduces circulation, results from an uneven build-up of boundary layer displacement thickness on the upper and lower airfoil surfaces, especially in the region of the trailing edge. Fluid flowing over the body surface is displaced by an amount determined by the boundary layer displacement thickness and it is this resulting displacement surface which sets the aerodynamic performance.

2.2 Trailing Edge Flows and the Kutta Condition

The Kutta condition in steady, inviscid, two-dimensional, incompressible flow plays an important role in the theoretical analysis of lifting-type bodies. Since varying interpretations

can lead to significantly different results when applied to the same airfoil section, care must be taken to properly state the condition for each class of trailing edge geometries, [1] sharp [finite internal trailing edge angle], [2] cusped or [3] blunt. Futher, it will be shown that by introducing viscosity, a single trailing edge condition can be adopted which satisfies each class, eliminating ambiguity between the different interpretations.

For sharp trailing edge geometries in true potential flow, one normally states that the trailing edge velocity must remain finite. This ensures that there there is no flow around the trailing edge and fixes the location of the rear stagnation streamline. The condition is extended by stating that the trailing edge velocities on the upper and lower surfaces be equal in magnitude, implying zero pressure gradient or zero loading at the trailing edge. Futher, one recognizes that the velocity at a sharp trailing edge [in true potential flow] must approach zero in order to avoid the discontinuity associated with the discrete change in streamwise direction at the point where the upper and lower surface streamlines meet, Figure 1.

For a cusped trailing edge in an inviscid flow, Figure 2, a similar argument holds with the exception that the upper and lower surface trailing edge velocities no longer must tend towards zero. The cusp provides a smooth, continuous joining of the upper and lower surface streamlines, thus avoiding the discrete change in direction associated with the sharp trailing edge.

Finally, for blunt trailing edges, Figure 3, the interpretation of the Kutta condition becomes somewhat more complicated for true potential flows. Since it is not possible to fix the location of the rear stagnation streamline, an infinite number of flow solutions can result.

The introduction of viscosity physically alters the trailing edge condition for each class considered by allowing the development of upper and lower surface boundary layers with separation occurring upstream from the actual trailing edge.

By allowing for the existance of a boundary layer, Sears [ref 24] offers an alternative trailing edge condition for airfoils with sharp/cusped geometries, also holding true for airfoils with rounded trailing edges, as detailed by Howarth [ref 12]. The ultimate conclusion is that the vortex strengths at the upper and lower surface points of boundary layer separation are equal in magnitude and opposite in direction.

The analysis is based on vorticity production in the boundary layer and is presented here for a fixed airfoil in steady flow.

For upper/lower surface separation points A and B [Figure 4] the vorticity flux in the boundary layer for a surface of negligible curvature is given as

$$\int_0^{\delta} u \frac{\partial u}{\partial y} dy \tag{2.1}$$

where δ is the total boundary layer thickness and u is the tangential velocity component through the boundary layer, both at separation.

Howarth's criteria for determining the circulation about a two-dimensional body is generalized as

> THE AVERAGE FLUX OF VORTICITY OUT OF ANY FIXED CIRCUIT IS ZERO, AND THEREFORE THE AVERAGE RATE AT WHICH POSITIVE VORTICITY IS TRANSPORTED FROM THE UPPER SURFACE INTO THE WAKE IS EQUAL TO THE AVERAGE RATE AT WHICH NEGATIVE VORTICITY IS TRANSPORTED FROM THE LOWER SURFACE.

Integrating the above expression for vorticity flux, while applying Howarth's criteria, yields a relationship between the upper and lower surface fluxes.

$$\frac{1}{2}u_A^2 - \frac{1}{2}u_B^2 = 0 \tag{2.2}$$

where u_A and u_B are the tangential velocities at the outer edges of the upper and lower surface boundary layers [at separation]. As Howarth points out, the velocities, and therefore the pressures, are the same at the points of separation on the upper and lower surfaces. For cases of trailing edge separation, it is important to note that Howarths criteria essentially reduces to the more familiar Kutta condition of zero pressure gradient across the trailing edge.

Sears expresses the upper and lower surface velocity components as perturbations of the undisturbed free stream

$$u_A = U + u'_A \tag{2.3}$$

and

$$u_B = U + u'_B \tag{2.4}$$

and shows that, to a first order approximation, the above expression of equal and opposite fluxes reduces to an expression equating the upper and lower surface vortex strengths.

$$U(u'_A - u'_B) = 0 = U\gamma_{t.e.} = U\gamma_{sep} \tag{2.5}$$

or

$$\gamma_A + \gamma_B = 0 \tag{2.6}$$

implying that the vortex strength of the airfoil [and wake] must be equal in magnitude and opposite in orientation at the trailing edge [or upper and lower surface points of separation].

Sears concludes his arguement by stating that

> " WHAT IS UNIQUE TO STEADY FLOW IS THAT HERE THE FLUXES ARE EQUAL AND OPPOSITE ABOVE AND BELOW THE TRAILING EDGE, AND THE VORTEX STRENGTH IS ZERO BOTH ON THE AIRFOIL AT THE TRAILING EDGE AND IN THE WAKE. "

The trailing edge condition, alternately stated as zero net vorticity discharge into the downstream wake, is thus valid for sharp, cusped and blunt trailing edge geometries when the effects of viscosity are considered. Allowing the existance of a boundary layer, the surface streamlines will be displaced by an amount corresponding to the boundary layer displacement thickness, giving even the true sharp/cusped trailing edge a finite thickness. Batchelor [ref 1] states that

> " IN PRACTICE IT IS DIFFICULT TO MAKE CUSPED TRAILING EDGES, BUT THE PRESENCE OF THE BOUNDARY LAYER AND WAKE DISPLACES THE IR-ROTATIONAL FLOW AWAY FROM THE AEROFOIL BY A SMALL DISTANCE WHICH IS NON-ZERO NEAR THE REAR EDGE, AND THE INNER BOUNDARY TO THE REGION OF IRROTATIONAL FLOW IS MADE CUSP-LIKE EVEN WHEN THE TRAILING EDGE OF THE AEROFOIL IS A WEDGE OF A SMALL ANGLE. "

In real flows with real fluids, the trailing edge condition should always be that of zero net vorticity discharge into the downstream wake.

Figure 5 shows a NACA 0012 airfoil section and it's predicted displacement surface at 6 degrees angle-of-attack for a chord based Reynolds number of 700,000. Figure 6 shows the corresponding pressure distribution where the effect on the rear stagnation point is clearly seen.

2.2.1 Laminar/Turbulent Boundary Layer Separation and Stall

In analysing the performance of airfoil-type bodies in two-dimensional, steady, incompressible flows, a fundamental understanding of the mechanisms responsible for boundary layer separation, the flow conditions at separation and the structure of the separated regions are considered crucial.

A boundary layer is assumed to have separated from a body surface when the retarding force associated with the streamwise adverse pressure gradient overcomes the inherent streamwise momentum of the laminar/turbulent boundary layer. When this occurs, the surface streamline separates from the body surface forming a local pocket of highly unsteady, recirculating flow. At the point of separation, the velocity profile within the boundary layer will display a zero normal gradient and the skin friction coefficient will go identically to zero.

For an airfoil possessing a finite trailing edge angle, the presence of a rear stagnation point forces an infinite adverse pressure gradient at the rear junction of the upper and lower surface streamlines. As a result, a small region of separated flow is observed to encompass several percent of the chord just upstream from the finite angle of the trailing edge.

Turbulent boundary layers generally possess higher levels of streamwise momentum than laminar layers as a result of the turbulent entrainment of high energy, outer-flow fluid into the boundary layer. Turbulent layers are therefore capable of withstanding larger adverse pressure gradients than typical laminar layers.

Boundary layer separation occurring over airfoil-type bodies eventually leads to stall. As the angle-of-attack is increased and the streamwise pressure gradient is driven to higher adverse levels, the airfoil displays a unique stall sequence depending on it's chord based Reynolds number and leading edge radius of curvature.

Four physically identifiable airfoil stall classes are recognized, [1] thin airfoil, [2] leading edge, [3] trailing edge and [4] combined. Figure 7 illustrates the distinct growth and decay in lift versus angle-of-attack for each stall class while Figure 8 provides an empirical correlation for stall class as a function of Reynolds number and nose radius for smooth airfoils (from Schlichting [ref 23]).

2.3 Transition at Low Reynolds Numbers

For weakly adverse pressure gradients, the transition process at low Reynolds numbers can be a randomly intermittent event occurring over a large portion of the body chord. Although typical transition models which address flow stability through the Orr-Sommerfeld equations do provide a prediction for the onset of transition, few methods address the problem of intermittently varying laminar/turbulent flow over a finite transition length. In order to truely capture the flow physics, or at least to explain model discrepencies, such a process should be taken into consideration.

2.4 Wake Shape

When viscosity is introduced to the steady, incompressible flow over airfoil-type bodies, a wake region invariably results. The shape, length and rate of closure strongly effect the resulting performance [ref 28]. The turbulent mixing occurring within the shear layer largely governs the wake behavior, but unfortunately, such a process is difficult to model. As a result, the wake length, shape and rate of closure are often arbirtarily specified to provide the best match to experiment.

Of particular concern is the *shape* of the wake region and whether the reunion of the upper and lower surface separation streamlines forms a cusp or a finite angle, Figure 9.

Lighthill [ref 15] answers affirmitave to the question of whether two free streamlines can meet in a cusp in pure potential flow. Tran-Cong [ref 28] suggests that

> " THERE IS ONLY ONE INFLECTION POINT ON THE TRAILING FREE STREAMLINES. THIS INFLECTION POINT IS ON THE UPPER FREE STREAMLINE

WHEN THE FLOW IS OPEN AND IS ON THE LOWER ONE WHEN THE FLOW IS CLOSED. "

implying that the separation streamlines rejoin in a cusp rather than a finite angle, for a closed wake.

The influence of wake shape on airfoil performance is significant. Panel-type flow models generally predict finite angles at the point of reunion, implying the presence of a downstream stagnation point. The question remains as to which case is physically recognizable for real separated flows.

2.5 Reynolds Number Effects

Typically, airfoil performance shows an extreme dependence on Reynolds number. Schlichting [ref 23] states that

" THE MOST IMPORTANT QUANTITY CHARACTERIZING VISCOSITY EFFECTS IS THE REYNOLDS NUMBER. FOR A GIVEN PROFILE GEOMETRY, THIS NONDIMENSIONAL QUANTITY DETERMINES DECISIVELY THE AERODYNAMIC COEFFICIENTS OF A WING. "

Although there is much to be said on this subject, the current section only briefly address the effects on lift for low Reynolds number flows. More detailed reviews can be found in references 22, 23 and 29.

As already pointed out, the presence of a boundary layer reduces the circulation around an airfoil section at angle-of-attack. The effect becomes more pronounced as the boundary layer thickens at lower Reynolds numbers. Futher, for extremely low Reynolds number

cases, intermittently laminar and turbulent flow with sporadic separation/reattachment is observed to occur, resulting in a highly non-linear, somewhat unpredictable aerodynamic performance. Bushnell [ref 4] points out that

> " ... [L/D]MAX FOR SMOOTH AIRFOILS CAN VARY BY ORDERS OF MAGNITUDE IN THE CHORD REYNOLDS NUMBER RANGE FROM 50,000 TO 200,000 ... "

He goes on to state that low Reynolds number airfoils are extremely sensitive to the disturbance environment and that device imperfections can compound the sensitivity.

Correlating the output from low Reynolds number flow models to experiment presents a unique challenge in itself due to the inconsistencies in measured performance observed to occur between test facilities. Appendix III provides a partial compilation of low Reynolds number data from several sources. The data clearly shows an increasing degree of scatter for lower Reynolds numbers, Figures 53 through 57.

2.6 Effect of Free-Stream Turbulence

The effect of free stream turbulence on the aerodynamic coefficients for airfoil-type bodies is important to the understanding and interpretation of experimental data as well as the accurate modelling of such flows.

Free stream turbulence effectively enhances the mixing process between the high momentum outer-flow fluid and the retarded boundary layer fluid. As a result of the increased mixing, the structure of the boundary layer flow can be considerably altered.

Consider an airfoil at angle-of-attack experiencing an intermediate sized laminar sep-

aration bubble in a clean, turbulence-free environment. By introducing turbulence to the approach flow, an increased momentum exchange is likely to occur between the initially attached laminar boundary and the high momentum outer flow. The increased momentum can be sufficient to overcome the adverse pressure gradients which originally lead to separation. The resulting effect could range from a slight downstream shift in the point of laminar separation to the elimination of the separation bubble entirely.

Observations indicate that transition occurs within the downstream portion of reattaching laminar separation bubbles. It is the turbulent mixing, following transition, that re-energizes the boundary layer to a high enough level for reattachment to occur. It is well known that free stream turbulence acts to promote transition in a laminar boundary layer [ref 29]. Similarly, it is believed that free stream turbulence acts to induce early transition within a laminar separation bubble, moving the point of turbulent reattachment upstream [not proven].

It can then be concluded that the net effect of free-stream turbulence on a laminar separation bubble is to shift the start of bubble downstream while decreasing the overall length. For extreme cases the bubble may be eliminated entirely and replaced by a fully attached turbulent boundary layer. The magnitude of the effect is likely to be a function of Reynolds number, surface roughness, local pressure gradient and free stream turbulence intensity/spectrum.

Chapter 3

Two Dimensional Boundary Layer Equations

In the analysis of boundary layers developed in two-dimensional, incompressible, steady flows, a logical starting point is with the well established integral momentum relation of Karman, valid for both laminar and time-averaged turbulent flows [ref 29].

$$\frac{d\theta}{dx} + [2 + H]\frac{\theta}{U_{edge}}\frac{dU_{edge}}{dx} = \frac{c_f}{2} \tag{3.1}$$

It's derivation is based upon the integration of the mass conservation and x-momentum equations from the body surface to an arbitrary distance outside the boundary layer. Substitution then eliminates all terms containing the normal velocity component.

The governing parameters which surface in the analysis of boundary layer flows and are inherent in the Karman integral relation are the displacement thickness, δ^*

$$\delta^* = \int_0^\delta [1 - \frac{u}{U}]dy \tag{3.2}$$

momentum thickness, θ

$$\theta = \int_0^\delta \frac{u}{U}[1 - \frac{u}{U}]dy \tag{3.3}$$

shape factor, H

$$H = \frac{\delta^*}{\theta} \tag{3.4}$$

and skin friction coefficient, c_f

$$c_f = \frac{\tau_{wall}}{Q} \tag{3.5}$$

Assuming a known outer flow solution [velocity or pressure distribution], the momentum integral relation of Karman contains three variables, θ, H and c_f. The solution depends on the availability of additional auxiliary equations relating the unknowns. For both laminar and turbulent flows, unique relations do exist. A wide variety of empirical expressions are often invoked to provide closure. Differing models tend towards varying results making the selection of such models somewhat dependent on the particular application.

Chapter 4

An Ideal Boundary Layer Model

Analysing the two-dimensional, incompressible, steady boundary layer not only requires accurate modelling of both the laminar and turbulent layers, but also requires an adequate transition model allowing for the coupling of the two regimes.

Ideally, the laminar boundary layer model should provide an accurate prediction method for the onset of laminar separation. Criteria should be made available which distinguishes between separation bubbles of negligible [short] and non-negligible [intermediate & long] length. The model should be capable of predicting whether the flow downstream of the bubble is fully separated or if turbulent reattachment occurs. Care should be taken to properly model the structure of the laminar separation bubble, including transition within the bubble. Allowances should be made for the stagnation point location near the leading edge.

The turbulent boundary layer model should be capable of accurately predicting the onset of turbulent separation. Ideally, the model should be capable of predicting whether the flow remains separated or reattaches futher downstream. Allowances should be made for the finite distance over which separation occurs.

Both the laminar and turbulent models should be capable of handling relaxing adverse

pressure gradients.

The transition model should not only be capable of predicting the onset of transition but should be capable of determining the finite distance over which it takes place. In addition, proper coupling between the laminar and turbulent boundary layer parameters [through transition] should be provided.

In practice the ideal model is rarely achieved. Instead a series of compromises are made based on the particular application. Issues of trade-off between desired accuracy, available computer time, degree of model complexity and ease of numerical implementation must be addressed.

Chapter 5

Current Boundary Layer Modelling Technique

5.1 Summary

For the current calculation, the method of Thwaites [ref's 2,5,19,22,29] is employed to model the structure of the laminar boundary layer. Inherent in Thwaites' model is a technique for predicting the onset of laminar separation. However, once separation is predicted, the model no longer holds valid and the structure of the separation region is lost.

For modelling simplicity, regions of laminar separation are assumed to be either of the short or long bubble-type, as governed by the criteria of Owen & Klanfer [ref 20]. The resulting model is greatly simplified since knowledge of the structure of intermediate sized laminar separation bubbles is no longer required.

Predictions for the distributions of displacement thickness, momentum thickness, shape factor and skin-friction coefficient are inherently provided.

Analysis of the turbulent boundary layer is conducted in accordance with the turbulent

entrainment model of Head [ref's 2,5,10,11,19]. Here a method is provided for calculating the structure of the turbulent boundary layer up to the singularity occurring at the point of turbulent separation. Head's model allows for predictions of displacement thickness, momentum thickness, shape factor and skin-friction coefficient as well as the chordwise points of turbulent separation.

Prior to the selection of Head's entrainment model, Stratford's separation criteria was used to predict the point of turbulent separation along the airfoil surface, assuming an entirely inviscid flow. Since early boundary layer separation was consistently predicted, the alternate technique of Head was adopted. Appendix I outlines Stratford's method and briefly discusses some of the problems encountered.

Transition is modelled in accordance with the criteria of Michel [ref's 5,19]. Here an expression is provided for predicting the point where the flow is fully turbulent. A significant downfall of Michel's model is that it assumes a negligible length of transition.

In an attempt to capture the finite length of transition, a somewhat more comprehensive transition model is proposed, although not used. The point of e^9 perturbation growth is first calculated from the Orr-Sommerfeld laminar stability equations. Granville's correlation is then invoked to calculate the finite length of transition. Finally, an intermittency function is introduced describing the relationship between the laminar and turbulent boundary layers within the finite transition length. Although the procedure is outlined in Appendix II, it's implementation has not yet been carried out.

5.2 Laminar Boundary Layer Model - Thwaites

Thwaites' model provides a one parameter approximate integral method for modelling a laminar boundary layer over a two-dimensional surface in an incompressible, steady flow

field. Here a set of one-parameter functions are fit to a collection of know analytical and experimental data in order to provide the necessary expressions for relating the unknowns of the Karman integral momentum relation.

The variables λ and ℓ are first introduced

$$\lambda = \frac{\theta^2}{\nu}\frac{dU_{edge}}{dx} \tag{5.1}$$

and

$$\ell = \frac{c_f U_{edge}\theta}{2\nu} \tag{5.2}$$

by imposing the following boundary conditions

$$[\frac{\partial^2 u}{\partial y^2}]_{y=0} = -\frac{U_{edge}}{\theta^2}\lambda \tag{5.3}$$

and

$$[\frac{\partial u}{\partial y}]_{y=0} = \frac{U_{edge}}{\theta}\ell \tag{5.4}$$

on the steady, two-dimensional boundary layer equations, mass,

$$\frac{\partial u}{\partial x} + \frac{\partial v}{\partial y} = 0 \tag{5.5}$$

and momentum

$$u\frac{\partial u}{\partial x} + v\frac{\partial u}{\partial y} = -\frac{1}{\rho}\frac{dp}{dx} + \nu\frac{\partial^2 u}{\partial y^2} \tag{5.6}$$

It is postulated that the remaining unknowns of the Karman integral relation c_f [or ℓ] and H, are functions of λ only

$$\ell = \mathcal{F}(\lambda) \tag{5.7}$$

$$H = \mathcal{G}(\lambda) \tag{5.8}$$

and the following empirically derived expressions are introduced, providing the necessary auxiliary equations for solving the Karman integral momentum relation.

For $0 \leq \lambda \leq 0.1$

$$\ell = 0.22 + 1.57\lambda - 1.8\lambda^2 \tag{5.9}$$

$$H = 2.61 - 3.75\lambda + 5.24\lambda^2 \tag{5.10}$$

and for $-0.1 \leq \lambda \leq 0$

$$\ell = 0.22 + 1.402\lambda + \frac{0.018\lambda}{0.107 + \lambda} \tag{5.11}$$

$$H = \frac{0.0731}{0.14 + \lambda} + 2.088 \tag{5.12}$$

Thwaites shows that θ, the momentum thickness, can be calculated for all types of laminar boundary layers (assuming a known outer flow solution) by the following integral expression.

$$\theta^2 = \frac{0.45\nu}{U_{edge}^6} \int_0^x U_{edge}^5 dx \tag{5.13}$$

Knowing θ, and hence λ and ℓ, the two remaining unknowns of the Karman integral momentum relation, H, the shape factor and c_f, the skin-friction coefficient, can be calculated.

5.2.1 Laminar Separation

Thwaites shows that the onset of laminar separation typically occurs when λ drops below the value of -0.09.

$$\lambda_{separation} = -0.09 \tag{5.14}$$

Due to the complexities involved in accurately modelling the structure of the laminar separation bubble, the assumption is made that regions of laminar separation assume only one of two forms.

The first allows for the existance of a short laminar separation bubble followed by point turbulent reattachment. Here, the event of laminar separation is interpreted as a mechanism which triggers turbulence, nothing more. Any thickening of the momentum thickness associated with the reattachment process is ignored, although probably not neglible.

The alternate form for the laminar separation region assumes the existance of a large separation bubble, dominating the entire chord without turbulent reattachment. Here the onset of laminar separation leads to a fully separated flow.

The foregoing assumptions are consistent with the observed structure of laminar separation bubbles at moderate Reynolds numbers. For low angles-of-attack, separation regions are generally of the short bubble type and do not force separation without turbulent reattachment. As the incidence is increased beyond a limiting value, the bubble rapidly grows in size and subsequent breakdown or bursting occurs, preventing turbulent reattachment. The intermediate state of medium sized bubbles takes place at an extremely rapid rate as the incidence is increased and stall is approached. The errors introduced by ignoring the structure of the intermediate laminar separation bubbles are therefore believed to be confined to a very small range in angle-of-attack [although not proven].

5.2.2 Stagnation

For the case of two-dimensional stagnation point flow, the boundary layer parameters are shown to be constant functions of the local velocity gradient in the streamwise direction. Schlichting [ref 22] outlines the case of stagnation in plane flow [Hiemenz flow] and ultimately concludes that the shape factor at stagnation is equal to the constant value of 2.21. Knowing H, Thwaites' λ is formed

$$\lambda_{H=2.21} = 0.125 \tag{5.15}$$

and the calculation of the momentum thickness and displacement thickness follow.

$$\theta = \sqrt{\lambda \nu / \frac{dU_{edge}}{dx}} \tag{5.16}$$

and

$$\delta^* = H\theta \tag{5.17}$$

The calculation of the stagnation point velocity gradient is carried out by assuming a proportional relationship to the inverse of the local radius of curvature. Futher, by assuming the leading edge stagnation flow to be analogous to the stagnation flow impinging on a cylinder, the Rayleigh-Janzen procedure [ref 29] gives a simple first order approximation for the local velocity gradient as a function of the approach Mach number, free-stream velocity and local radius of curvature.

$$\frac{dU_{edge}}{dx} \approx \frac{4U_\infty}{D} + h.o.t's \tag{5.18}$$

5.2.3 The Criteria of Owen & Klanfer

Owen & Klanfer provide a simple, one-step technique for determining whether the onset of laminar separation is followed by a short bubble with immediate turbulent reattachment or a long bubble with an extended separation zone. Owen & Klanfer state that

> " ... THE LENGTH OF THE BUBBLE DEPENDS PRIMARILY ON THE REYNOLDS-NUMBER (Re_{δ^*}) BASED ON THE DISPLACEMENT THICKNESS AT THE SEPARATION POINT " and that " ... IF Re_{δ^*} EXCEEDS 400-500, THE BUBBLE IS SHORT. "

Gastner [ref 9] indicates better agreement with experiment with a value of 450. For the current application, a brief study is conducted to determine an acceptable limiting value by varying Re_{δ^*} and comparing the predicted output in lift coefficient to that demonstrated experimentally. It is found that for values of Re_{δ^*} [at separation] less than 500, the assumption of a long separation bubble without reattachment provides a physically realistic model. Hence, for reattachment to occur, it is assumed that the following criteria must be satisfied.

$$[Re_{\delta^*}]_{separation} \geq 500 \tag{5.19}$$

5.3 Transition Model - Michel

The empirically derived criteria of Michel provides a simple one-step method for approximating the point of transition along two-dimensional airfoil-type bodies in steady, incompressible flows. By examining a wide body of experimental data, Michel shows that transition can be assumed to have occurred upon satisfying the following expression.

$$Re_\theta > 1.174(1 + \frac{22,400}{Re_x})Re_x^{0.46} \tag{5.20}$$

where

$$Re_\theta = \frac{U_\infty \theta}{\nu} \tag{5.21}$$

and

$$Re_x = \frac{U_\infty x}{\nu} \tag{5.22}$$

One concern with Michel's criteria is that it does not allow for a finite length of transition but rather models it as a point change in state. It follows that errors are likely to to occur for critical low Reynolds number flows where the transition process can take place over an extended portion of the chord.

5.4 Turbulent Boundary Layer Model - Head

Head's turbulent entrainment model provides an approximate integral method for predicting the mean structure of a two-dimensional turbulent boundary layer with arbitrary pressure gradient in a steady, incompressible flow field. Two empirical expressions are introduced relating the turbulent entrainment velocity to the local boundary layer shape factors which, when combined with the Karman integral momentum equation and the Ludwieg-Tillman skin-friction law, yield a system of four non-linear equations in four unknowns.

The turbulent entrainment velocity, V_E, is defined as the component of velocity normal to the edge of the boundary layer, or, similarly, as the rate at which the volume flow rate per unit span changes with respect to the streamwise direction within the turbulent boundary layer, shown below.

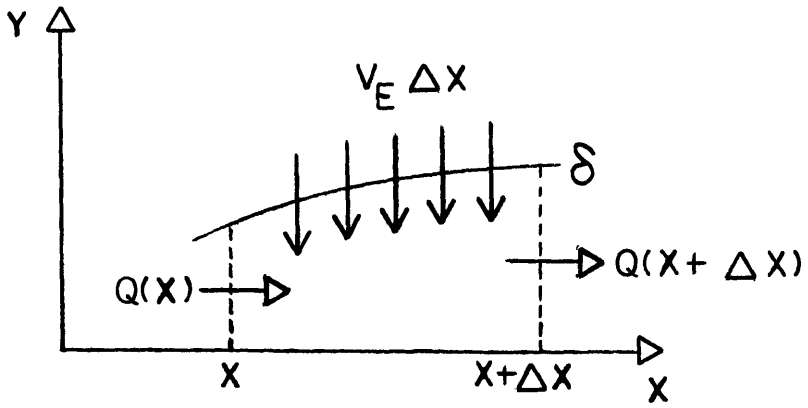

By first defining the volume flow rate per unit span

$$Q(x) = \int_0^\delta u dy \tag{5.23}$$

the turbulent entrainment velocity can be stated as

$$\frac{V_E}{U_{edge}} = \frac{1}{U_{edge}} \frac{dQ}{dx} \tag{5.24}$$

Integrating the expression for δ^* and rearranging terms gives

$$\int_0^\delta u dy = U_{edge}[\delta - \delta^*] \tag{5.25}$$

Substitution then yields

$$\frac{V_E}{U_{edge}} = \frac{1}{U_{edge}} \frac{d}{dx}(U_{edge}(\delta - \delta^*)) \tag{5.26}$$

Head first assumes that the turbulent entrainment velocity is a function of the modified shape factor, H_1.

$$\frac{V_E}{U_{edge}} = \mathcal{F}(H_1) \tag{5.27}$$

where

$$H_1 = \frac{\delta - \delta^*}{\theta} \tag{5.28}$$

and rearranging terms gives

$$\frac{d}{dx}(U_{edge}(\delta - \delta^*)) = \frac{d}{dx}(U_{edge}\theta H_1) \tag{5.29}$$

or

$$\frac{d}{dx}(U_{edge}\theta H_1) = \mathcal{F}(H_1) \tag{5.30}$$

Head then assumes that the modified shape factor H_1 is a direct function of the true shape factor, H.

$$H_1 = \mathcal{G}(H) \tag{5.31}$$

where

$$H = \frac{\delta^*}{\theta} \tag{5.32}$$

The functions $\mathcal{F}(H_1)$ and $\mathcal{G}(H)$ are then empirically determined through a best fit correlation to experiment [ref 5].

$$\mathcal{F}(H_1) = 0.0306(H_1 - 3.0)^{-0.6169} \tag{5.33}$$

$$\mathcal{G}(H) = 0.8234(H - 1.10)^{-1.287} + 3.3 \quad H \leq 1.6 \tag{5.34}$$

$$\mathcal{G}(H) = 1.5501(H - 0.6778)^{-3.064} + 3.3 \quad H \geq 1.6 \tag{5.35}$$

Closure is provided by invoking the Ludwieg-Tillman skin-friction law, assuming knowledge of the external flow field.

$$c_f = 0.246 \times 10^{-0.678H} Re_\theta^{-0.268} \tag{5.36}$$

The three unknowns of the integral momentum relation, θ, H and c_f, are coupled through the given set of equations. An iterative method can then be to determine the distributions of the boundary layer parameters along the body surface.

5.4.1 Laminar-Turbulent Coupling through Transition

Allowances are made to specify the boundary layer parameters through transition to ensure proper initiation of the turbulent boundary layer calculation. For the current application, the shape factor and momentum thickness are specifed while the skin-friction coefficient is directly obtained from the Ludwieg-Tillman correlation.

Cebeci and Bradshaw [ref 5] and Chang [ref 7] suggest that θ, the momemtum thickness, remain contintinous through transition. Chang states that

> " WHEN TURBULENCE IS INTRODUCED, AN INCREASED MIXING OCCURS IN A VERY SHORT DISTANCE, SO THAT THETA MAY BE REGARDED UNCHANGED. "

Regarding H, the shape factor, Chang [ref 7] suggests that the displacement thickness [and therefore shape factor] depends on the spatial extent and distribution of turbulent mixing within the boundary layer. He suggests that because $\frac{\partial u}{\partial y}$, the normal gradient of the streamwise velocity, of the turbulent layer is considerably larger than that of the laminar layer, the bulk of the mixing occurs in a region closer to the body surface, driving the displacement thickness, δ^* [and hence shape factor], to a lower value. Figure 10 illustrates the process, although somewhat exaggerated.

For cases of natural transition, Chang suggests that the shape factor assume the constant value of 1.3 at the start of the turbulent boundary layer calculation while Moran [ref 19] and Cebeci & Bradshaw [ref 5] suggest values between 1.3 and 1.4. For the current calculation a value of 1.35 is used. Since transition is assumed to occur over a negligible length, the boundary layer parameters are simply switched from the laminar to turbulent values once Michel's criteria is satisfied.

$$[\theta_{turbulent}]_{at\ transition} = [\theta_{laminar}]_{at\ transition} \tag{5.37}$$

$$[H_{turbulent}]_{at\ transition} = 1.35 \tag{5.38}$$

For the case of laminar separation with point turbulent reattachment, the process of defining the boundary layer parameters through transition is not addressed in the literature which was examined. Chang [ref 7] does however point out that

> " WHEN A LAMINAR BOUNDARY LAYER SEPARATES AND REATTACHES TO THE SURFACE AS A TURBULENT BOUNDARY LAYER, IT IS DIFFICULT TO FIX THE INITIAL CONDITION FOR THE COMPUTATION OF THE TURBULENT BOUNDARY LAYER. "

For lack of a better method, the transition process associated with a reattaching short laminar separation bubble is considered analogous to the natural transition process where the momentum thickness remains continuous and the shape factor makes a discrete jump to the constant value of 1.35.

The foregoing assumptions may appear to be somewhat inconsistent with the expected physical behavior of such flows. For example, following a laminar separation bubble of assumed negligible length, it is likely that the momentum thickness will be increased upon turbulent reattachment. Futher, both the transition shape factor and momentum thickness are likely to show a dependence on the local Reynolds number, pressure gradient, surface roughness, etc ...

5.4.2 Turbulent Separation

Since the Ludwieg-Tillman skin-friction law only provids zero skin friction as H tends towards infinity, predictions based on the skin-friction distribution are not possible. Instead, by examining the streamwise distribution of shape factor, the point of turbulent separation can be inferred.

Cebeci & Bradshaw [ref 5] state that it is not possible to specify an exact value for the shape factor corresponding to separation but instead suggest that for values of H between 1.8 and 2.4, the flow can be assumed to have detached from the body surface. Since the gradient of H with respect to the streamwise direction generally shows a rapid rate of increase as the point of separation is approached, the difference between the upper and lower values only weakly effects the end result. For this reason the following turbulent separation criteria is employed.

$$H_{sep} = 2.2 \tag{5.39}$$

It is recommended that an investigation be carried out to determine the sensitivity of the predicted separation location to values of H_{sep} between 1.8 and 2.4. It is futher suggested that a single value of H_{sep} be universally adopted, thus eliminating any variations in the results, however small they may be.

Finally, it should be pointed out that the physical process of turbulent separation is observed to occur over a finite distance rather than at a discrete point. Kline [ref 14] states that

> "... TWO DIMENSIONAL TURBULENT FLOW DETACHMENT FROM A FAIRED SURFACE IS NOT A SINGLE EVENT, BUT RATHER A PROCESS, A TRANSITION FORM ATTACHED TO DETACHED FLOW. TURBULENT DETACHMENT WITH STEADY TIME MEAN FLOW OCCURS OVER A ZONE, NOT ALONG A SINGLE LINE NORMAL TO THE FLOW, AS IN THE LAMINAR CASE. "

Since the current model entirely ignores the existance of this finite region of intermittent flow detachment, care should be taken in the interpretation of the results.

Chapter 6

The Inviscid Vortex Panel Method

The calculation of the inviscid solution is based upon the classical method of singularities. For the current application, the body surface and wake are broken up into a finite number of panels defined by a leading and trailing edge node. Each panel node is then assigned an unknown vortex strength, assumed to vary linearly in the streamwise direction across each panel, simulating a continuous vortex sheet. Superposition of the translational flow with that induced by the unknown vorticity distribution yields a set of n linear equations in n unknowns which can be directly solved through Gaussian elimination by imposing the boundary conditions of flow tangency and zero net vorticity discharge into the wake. Figure 11 details the wing configuration for a typical two-dimensional vortex panel method.

Applying the Biot-Savart law to a given piecewise linear distribution of vorticity per unit length, Figure 11, the induced velocities in the tangential and normal direction can be calculated.

$$u(x,z) = \frac{1}{2\pi}\int_0^c \gamma(x')\frac{z}{(x-x')^2+z^2}dx' \tag{6.1}$$

and

$$w(x,z) = -\frac{1}{2\pi}\int_0^c \gamma(x')\frac{x-x'}{(x-x')^2+z^2}dx' \tag{6.2}$$

The boundary conditions of zero panel through flow and zero vorticity discharge allow a unique solution for a given body geometry and approach velocity.

$$[\gamma_{separation}]_{upper} = [\gamma_{separation}]_{lower} \tag{6.3}$$

and

$$w(x,z) = 0 \quad everywhere \tag{6.4}$$

Futher details on the actual numerics can be found in Burn's [ref 3] thesis dealing with a 3-D tunnel correction vortex panel method.

Chapter 7

Computational Algorithm

Figure 12 shows a flow chart which illustrates the local & global boundary layer iterations as well as the governing convergence criteria.

Starting from the initial potential flow solution, the two-dimensional boundary layer is successively recalculated until a specified set of convergence criteria is met. Following any one calculation of the boundary layer, the airfoil geometry is adjusted to account for the effect of the displacement thickness. The potential flow solution is then recalculated for the new displacement surface and the iteration is repeated until convergence is achieved.

Aside from the potential flow convergence criteria that the resulting flow velocity normal to each wing/wake panel does not excede 0.8 % of the free-stream value, the additional criteria that the predicted separation location does not move from one boundary layer iteration to the next, is introduced.

$$\Delta x_{sep} = 0 \tag{7.1}$$

and

$$w(x,z) \leq 0.008 U_{\infty} \tag{7.2}$$

Beginning at the leading edge stagnation point and proceding in the streamwise direction

over the upper and lower airfoil surfaces, the boundary layer analysis is carried out until either separation is predicted or the trailing edge is reached. Depending on the Reynolds number, airfoil section and angle-of-attack, one of six sequences of events will occur.

- Fully attached laminar flow.
- Fully attached turbulent flow following short laminar separation bubble with point turbulent reattachment.
- Fully attached turbulent flow following natural transition.
- Laminar separation without reattachment.
- Turbulent separation following short laminar separation bubble with point turbulent reattachment.
- Turbulent separation following natural transition.

The outputs from the boundary layer routine are the streamwise distributions of displacement thickness δ^*, momentum thickness θ and shape factor H, as well as the upper and lower surface chordwise points of turbulent separation, $[x_{sep}]_{upper}$ and $[x_{sep}]_{lower}$.

Regarding turbulent separation, it is found that at moderate angles-of-attack, as the structure of the boundary layer is sequentially recalculated, the predicted point of turbulent separation reaches a point where it oscillates about some mean chordwise position. To prevent the oscillation and allow solution convergence, the constraint is enforced that the point of turbulent separation may procede in the upstream direction only. Errors associated with this constraint are expected to be small at low angles-of-attack but are likely to increase as stall is approached where the sensitivity of section lift coefficient to separation location becomes more pronounced.

Chapter 8

Numerical Implementation

The boundary layer formulations are implemented in a logical, modularized, straightforward manner and should be easily decipherable by the user. Several areas require the use of approximations or techniques which may not be so readily obvious and are threrefore discussed here.

8.1 Derivatives

Solutions to the integral boundary layer equations as outlined in the preceding sections require the calculation of first order derivatives. Knowledge of $\frac{du}{dx}$, the gradient in velocity with respect to the streamwise direction along the airfoil surface, is necessary. For this calculation, a weighted, central-differencing scheme for non-uniform grids is employed.

$$\frac{du}{dx} = \frac{D_2}{D_1 + D_2}\frac{u_i - u_{i-1}}{D_1} + \frac{D_1}{D_1 + D_2}\frac{u_{i+1} - ui}{D_2} \tag{8.1}$$

8.2 Turbulent Boundary Layer Calculation

Under the modelling technique of Head, four equations are provided which relate the unknowns c_f, H, H_1 and θ.

$$\frac{d\theta}{dx} + [H+2]\frac{\theta}{U_{edge}}\frac{dU_{edge}}{dx} = \frac{c_f}{2} \tag{8.2}$$

$$\frac{d}{dx}[U_{edge}\theta H_1] = U_{edge}\mathcal{F}(H_1) \tag{8.3}$$

$$H_1 = \mathcal{G}(H) \tag{8.4}$$

$$c_f = 0.246 \times 10^{-0.678H} Re_\theta^{-0.268} \tag{8.5}$$

To simplify the discussion, the expressions are written in reduced form.

$$\mathcal{F}_1(\theta, H, c_f, H_1, U_{edge}) = 0 \tag{8.6}$$

$$\mathcal{F}_2(\theta, H, c_f, H_1, U_{edge}) = 0 \tag{8.7}$$

$$\mathcal{F}_3(\theta, H, c_f, H_1, U_{edge}) = 0 \tag{8.8}$$

$$\mathcal{F}_4(\theta, H, c_f, H_1, U_{edge}) = 0 \tag{8.9}$$

The above system is solved for each panel control point up to the predicted point of separation, assuming a known outer-flow [edge] solution. The iterative method of steepest descent is employed to march the solution forward in space.

Beginning with known values of H, θ and c_f, the Karman integral relation is first used to to calculate $\frac{d\theta}{dx}$, the gradient of theta with respect to the streamwise direction.

$$[\frac{d\theta}{dx}]_i = \frac{c_{f_i}}{2} - [H_i + 2]\frac{\theta_i}{U_{edge_i}}[\frac{dU_{edge}}{dx}]_i \tag{8.10}$$

This allows for the approximation of θ at the adjacent downstream panel control point where the remaining equations are iteratively solved for H, H_1 and c_f.

$$\theta_{i+1} = [\frac{d\theta}{dx}]_i(x_{i+1} - x_i) + \theta_i \tag{8.11}$$

Knowing θ, H and c_f at the new control point, $\frac{d\theta}{dx}$ is recalculated and a new approximation is made for θ_{i+1} at the next control point. From here the process repeats until either separation is predicted or the trailing edge is reached.

8.3 Method of Steepest Descent

The method of steepest descent [ref 26] provides an approximate solution to n non-linear equations in n unknowns. Although several sources suggest that more complicated schemes such as Newton or Newton-Rapson provide a more rapid rate of convergence, the selection of the method of steepest descent was based on it's relative ease of implementation.

For the three non-linear equations containing unknowns H, H_1 and c_f, the method can be stated as follows.

$$H_1^{n+1} = H_1^n - \kappa \mathcal{F}_2^n \tag{8.12}$$

$$H^{n+1} = H^n - \kappa \mathcal{F}_3^n \tag{8.13}$$

$$c_f^{n+1} = c_f^n - \kappa \mathcal{F}_4^n \tag{8.14}$$

By setting κ to the value of 0.1 and by introducing the convergence criteria that the levels for H, H_1 and c_f shall differ by not more that 0.01 % from one iteration level to the next, solution convergence is typically achieved in roughly 100 iterations.

Figures 13, 14 and 15 show the convergence histories for H, H_1 and c_f at the mid-chord point along the upper surface of a NACA 0012 airfoil at 4 degrees angle-of-attack for a chord based Reynolds number of 700,000.

8.4 Integration

Solutions to the two-dimensional boundary layer equations require the integration of flow variables in the streamwise direction. Futher, integration is required in the reduction of pressure distributions to corresponding aerodynamic coefficients. Discretization is carried out with the trapezoidal rule.

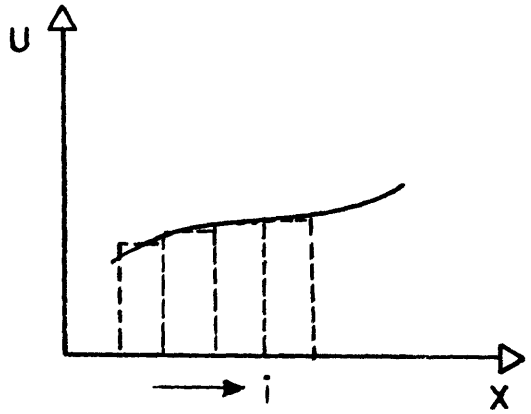

$$\int_0^x U\ dx = \sum_{i=1}^{n} [U_{i+1} - U_i] \frac{dx}{2} \tag{8.15}$$

8.5 Smoothing

Thwaites' integral boundary layer calculation near the point of laminar separation initially produced a distribution of displacement thickness that was not entirely smooth or continuous. Figure 16 shows the extreme sensitivity of shape factor to Thwaites' λ, especially near separation.

In an effort to minimize the errors associated with the jagged distribution, a polynomial

curve fitting routine was used to locally smooth the outer flow velocity distribution prior to the execution of Thwaites' model. Figure 17 shows the effect on the distribution of the shape factor over the upper surface of a NACA 0012 airfoil at 4 degrees angle of attack for a chord based Reynolds number of 700,000.

Chapter 9

Model Configuration and Sensitivity

It is necessary to define a proper panelling distribution and wake-length correlation prior to the execution of the viscid/inviscid flow model. Good overall resolution ensures [1] accurate predictions for the point of separation and [2] accurate modelling of the concentrated leading edge pressure peak while an accurate wake-length correlation ensures proper modelling of the separation zone and downstream rate of wake closure.

It is observed that the flow model displays varying degrees of sensitivity to the following:

- number & distribution of wing/wake panels
- wake-length (point of closure)
- initial wake shape
- chordwise separation location
- degree of leading-edge panel clustering

In an effort to define an optimum model configuration, a partial sensitivity analysis is conducted using a NACA 0012 profile as a baseline reference section.

9.1 Number & Distribution of Wing/Wake Panels

By simply varying the number of panels used to model the airfoil section and wake, a moderately large variation in the predicted lift coefficient, c_ℓ, is observed for cases of both separated and attached flow.

Figure 18 shows the sensitivity of c_ℓ to an increasing number of uniformly distributed panels at 4 degrees angle-of-attack, fully attached. Also shown is the theoretical value for the c_ℓ calculated according to

$$c_\ell = 2\pi[1 + 0.77\frac{t}{c}]\alpha \tag{9.1}$$

There appears to be a consistent upward trend in c_ℓ as the number of panels is increased. Between 50 and 100 panels, excellent agreement between the theoretical and predicted lift coefficient is obtained. The projection beyond 100 panels, however, indicates a considerable overshoot in c_ℓ, the source of which is presently unknown. Contributions from round-off and truncation errors are assumed to be small.

Figure 19 illustrates the sensitivity of lift coefficient to an increasing number of uniformly distributed panels at 4 degrees angle-of-attack, with separation forced at 90 % of the chord. The larger, non-uniform variations in c_ℓ are most likely a result of the separated region where the wake assumes a slightly different shape depending on the local panelling density.

By forcing excessively dense leading edge clustering, the model predictions become somewhat unstable. The predicted lift coefficient randomly jumps between high and low values, not necessarily converging to the theoretical value. The source of the instability is unknown, althought believed to be the result of higher-order modelling approximations made in the

inviscid model.

The underprediction of the lift coefficient for coarser panel distributions results from inadequate representation of the actual airfoil geometry.

9.2 Wake Length

When flow separation occurs upstream from the airfoil trailing edge, the wake-length and rate of wake closure have a marked effect on the predicted performance. For short wake lengths, the separation streamline is observed to assume an extremely high degree of curvature and the wake region forms a tight, rapidly closing loop. For longer wake lengths, the rate of wake closure is much more gradual and the separation streamline appears somewhat more relaxed (less curvature).

In an effort to provide some degree of control over the specified wake-length, an approximate wake closure scheme developed by Maskew & Dvorack [ref 17] is employed. Here an expression relating body thickness to a *wake factor* is provided, Figure 20. Knowledge of the body geometry, angle-of-attack and distribution of displacement thickness provide the necessary inputs, Figure 21.

Finally, it should be noted that for cases of fully attached flow, the performance predictions are only weakly effected by the wake length.

9.3 Jet Boundary Analogy

Recognizing the physical similarity between a separated turbulent flow and a turbulent jet boundary, an alternative to Dvorack's model is suggested. Schlichting [ref 22] discusses the process of turbulent mixing within the shear layer of a jet boundary and ultimately shows that the extent of the mixing zone follows a 6.5 degree line relative to the undisturbed free stream. For the case of leading edge flow separation, by forcing the separation streamline

along a 6.5 degree path as measured relative to the free stream direction at the point of separation, an approximate model for the wake shape and point of closure can be obtained. Figures 22 and 23 illustrate the process although the method has not yet been implemented or tested.

9.4 Initial Wake Shape/Position

For separated flows, the model shows a moderate degree of sensitivity to the initial wake shape which starts the calculation. It is believed that the inconsistency results from the rotation/translation process by which each wake panel is adjusted to satisfy the flow-tangency boundary constraint.

Figure 24 shows a panelled body surface with a separated wake. In adjusting the wake, the objective is to align each panel with a commom streamline, satisfying the boundary condition of flow tangency. The first wake panel (at separation) is rotated through an angle determined by

$$\theta_i = TAN^{-1}[\frac{w_\ell}{u_\ell}]_i \tag{9.2}$$

where u_ℓ and w_ℓ are the local panel flow velocities in the tangential and normal directions. The specified rotation exactly satisfies the zero through-flow boundary condition. For the remaining portion of the wake, each panel is first rotated, then translated so that the wake remains continuous.

Following each wake adjustment, the inviscid solution is recalculated, and the process repeated until each panel through-flow is less that 0.8 percent of the free-stream velocity. Due to the translation/rotation process, the boundary condition of zero panel through-flow is never met. It is observed that as the solution is successively recalculated, the wake reaches a point where it fluctuates about some mean level. Final convergence is achieved as the maximum wake panel through-flow randomly drops below the specified limit.

Figure 25 shows a representative trace of the maximum wake panel through-flow versus the corresponding lift coefficient for a NACA 0012 airfoil at 4 degrees angle-of-attack for a chord based Reynolds-number of 700,000 [with forced separation]. The dependence on panel through-flow is clearly seen.

9.5 Separation Location

The predicted airfoil performance is naturally a strong function of the chordwise separation location. Since separation is allowed to occur at panel nodes only, it is necessary to provide a dense enough overall panel distribution to minimize the effect of discrete jumps between adjacent panel nodes.

The sensitivity of c_ℓ to separation location is observed to vary with angle-of-attack, the most extreme case occurring near stall. Beyond stall and for trailing edge separation, the effect is less pronounced.

9.6 Final Configuration

The final panel configuration, shown in Figure 26, consists of 55 wing panels and 5 wake panels. A half cosine distribution is used to set the distribution of the first ten panels over the first ten percent of the chord, providing the desired degree of clustering towards the leading edge. Over the remaining 90 percent of the chord, 45 panels are evenly spaced, confining the movement of the separation location to discrete chordwise jumps of 2 %.

When separation is predicted to occur between two panel nodes, adjustments are allowed to procede in the upstream direction only, thus avoiding the singularity associated with the rapidly increasing shape factor at separation.

The wake length is allowed to vary with the point of separation according to the criteria of Dvorack. For the first iteration (fully attached), in order to initiate the boundary layer

routine, the wake length is set to five percent of the chord.

When an airfoil section is cut short to form a blunt trailing edge, the wing panels of the cut section are simply switched to wake panels. In performing the switch, the total number of wing & wake panels is maintained.

Chapter 10

Results

10.1 Full Airfoil Section - Comparison to Experiment

In an effort to validate the current numerical model, a comparison to experiment is made. Unfortunately, for low Reynolds number flows, large variations in the aerodynamic coefficients for airfoil-type bodies are observed to occur between different test facilities. Appendix III looks at data from six sources and attempts to generate baseline reference curves for Reynolds numbers of 700,000 and 1,000,000.

Figures 27 through 30 show the predicted [and measured when available] lift coefficients as functions of angle-of-attack for chord based Reynolds numbers of 125,000, 400,000, 700,000 and 1,000,000. Figure 31 shows the predicted lift curves for each of the four Reynolds numbers.

10.2 Full Airfoil Section - General Flow Features

Aside from addressing the accuracy of the global predictions for the lift and moment coefficients, c_ℓ and $c_{m_{l.e.}}$, the capacity for predicting the local flow characteristics must

be examined. Of particular concern are the distributions of momentum thickness, displacement thickness and shape factor through the laminar and turbulent boundary layers. Inherent in these distributions are predictions for the points of transition, laminar separation-rettachment and turbulent separation. Unfortunately, few experimental studies agree on the measurements of chordwise distributions. McCroskey [ref 18] states that

> "... IT WAS FOUND THAT THERE IS INSUFFICIENT OVERLAP IN THE EXPERIMENTS TO MAKE MANY MEANINGFUL, DIRECT COMPARISONS OF MORE DETAILED QUANTITIES, SUCH AS PRESSURE DISTRIBUTION ... "

For this reason, the detailed distributions of pressure and the boundary layer parameters are discussed from a qualitative viewpoint only.

Figures 32, 33 and 34 show traces of the calculated shape factor, H, momentum thickness, θ, and displacement thickness, δ^*, for a NACA 0012 airfoil section at 10 degrees angle-of-attack for a chord based Reynolds number of 700,000. Of particular interest are the increasing streamwise gradients near the points of laminar and turbulent separation and the discrete jumps occurring at the point of reattaching short laminar separation bubbles.

Due to the singularity occurring at the point of separation, the calculation of the shape factor cannot be carried out over the entire airfoil section. Other methods, such as that of Kline [ref 14], avoid the singularity by employing alternate modelling techniques. For the current application, the calculation of the boundary layer is terminated when either laminar separation [without reattachment] or turbulent separation is predicted.

When transition is predicted, the shape factor is assumed to make a discrete jump from it's current level to the constant value of 1.35, Figure 32. Cebeci & Bradshaw [ref 5] point out that choosing an exact value for $H_{transition}$ is not crucial since the turbulent boundary layer calculation will soon smooth out any errors introduced.

Except for extreme cases where laminar separation is predicted to occur at one of the forward wing panels, the leading edge pressure peak is generally adequately captured. For a NACA 0012 section at 16 degrees angle-of-attack and a chord based Reynolds number of 700,000, the converged pressure distribution fails to show a leading pressure peak due to the inadequacy in local panel resolution, Figures 35 and 36. It is believed however, that the pressure peak for such cases is sufficiently concentrated so that by ignoring it's existance, only minimal errors are introduced.

Since the airfoil geometry is adjusted in accordance with the calculated displacement thickness, the points of natural transition and reattaching laminar separation bubbles are generally identifiable in the resulting pressure distributions, Figure 37.

Finally, for cases of leading & trailing edge separation, the predicted pressure distributions consistently show the physically recognizable constant pressure region associated with the separation zone, Figures 38 and 39.

10.2.1 Laminar Separation

For Reynolds numbers below 1,000,000, laminar separation is consistently predicted near the leading edge of a NACA 0012 airfoil section. Whether the flow undergoes point turbulent reattachment or remains fully separated is dependent on the airfoil section, angle-of-attack and chord based Reynolds number. In the event of a reattaching laminar separation region, the turbulent boundary layer may subsequently detach from the airfoil surface as determined by the application of Head's turbulent entrainment model, Section 5.

Figure 40 shows the predicted separation locations for a NACA 0012 section at Reynolds numbers of 125,000, 400,000, 700,000 and 1,000,000. The sudden jump from leading to trailing edge separation occur when the flow fails to reattach following the onset of laminar separation. The limiting angle-of-attack where point turbulent reattachment [following

laminar separation] fails to occurs appears to decrease with Reynolds number. For example, at a Reynolds number of 125,000 and an angle-of-attack of 4 degrees, the laminar separation region encompasses the entire chord, without turbulent reattachment while at a Reynolds number of 1,000,000, laminar separation is immediatly followed by point turbulent reattachment for all angles-of-attack up to 16 degrees.

As discussed in section 5, regions of laminar separation are modelled in one of two forms, either short bubble with point turbulent reattachment or long bubble without reattachment. The formation of intermediate sized bubbles can lead to substantial increases in lift. However, since intermediate sized laminar separation bubbles are not modelled, errors are to be expected in the critical angle-of-attack range where the bubble experiences rapid growth.

For a Reynolds number of 125,000, Figure 40, leading edge laminar separation with point turbulent reattachment occurs at 2 degrees angle-of-attack. As the incidence is increased to 4 degrees, reattachment fails to occur and the flow remains fully detached. Between 2 and 4 degrees, where the transition between short and long bubbles takes place, errors are to be expected.

The range in angle-of-attack where the short-long bubble transition takes place is believed to decrease with increasing Reynolds number.

10.2.2 Turbulent Separation

As the chord based Reynolds number is increased, the stall-type experienced by a NACA 0012 airfoil section changes from [1] leading edge to [2] combined and finally to [3] trailing edge.

For a Reynolds number of 1,000,000, the onset of trailing edge separation occurs at 10

degrees angle-of-attack and as the incidence is increased, the point of turbulent separation gradually moves upstream. The resulting curve of lift coefficient versus angle-of-attack is considerably different from that predicted to occur at lower, more critical Reynolds numbers.

10.2.3 Reynolds Number Effects

Figure 31 shows the dependence of lift coefficient on Reynolds number. As the Reynolds number is lowered, the displacement thickness increases, Figure 41, reducing the circulation and yielding less lift at a given incidence. Similarly, it is observed that the Reynolds number strongly effects the laminar separation region. For example, at a Reynolds number of 700,000, laminar separation without reattachment occurs beyond 12 degrees angle-of-attack, while at a Reynolds number of 1,000,000, point turbulent reattachment occurs for angles-of-attack up to 16 degrees.

10.3 Effect of Trailing Edge Bluntness

Taking a NACA 0012 airfoil as a baseline reference section, the effect of trailing edge bluntness is addressed by cutting short the airfoil section at chordwise locations of 96, 92 and 88 %.

The comparison between different airfoil sections is made by referencing the lift and moment coefficients to [1] the 100 percent section and [2] the actual reduced chord length. The calculation is carried out for incidence angles between 2 and 16 degrees, in two degree increments. The wake is allowed to vary as a function of separation location and displacement thickness as outlined in Section 5. Convergence is achieved when the maximum wake panel through-flow is less than 0.8 % of the free stream velocity and when the separation location does not change from one boundary layer iteration to the next.

Figures 42 and 43 show the predicted lift and moment polars as a function of trailing edge bluntness referenced to the 100 percent section, while Figures 44 and 45 show the coefficients referenced to the actual reduced chord lengths [0.96, 0.92 or 0.88]. Figures 46 and 47 show the predicted separation locations versus angle-of-attack as a function of trailing edge bluntness referenced to the 100 percent section and the reduced chords, respectively.

It is observed that substantial losses in lift result for the 88 and 92 percent sections while only fraction losses are experienced for the 96 percent section for angles-of-attack between 0 and 10 degrees.

For cases of fully attached flow, introducing trailing edge bluntness to the reference airfoil section effectively reduced the area over which the pressure acts. It is observed that only a small portion of the lift is generated near the trailing edge and that by introducing small degrees of trailing edge bluntness, the lift can be maintained.

The boundary condition of equal and opposite shed vorticity on the upper and lower airfoil surfaces near the trailing edge ensures that the distributions of upper & lower surface vorticity approach constant levels [equal and opposite] as the trailing edge is neared. It is observed that by cutting short [up to 4 %] the airfoil section the circulation is essentially maintained since the upper and lower surface vorticity in this region essentially sums to zero.

Finally, it should be pointed out that the separation locus remains relatively uneffected by the introduction of trailing edge bluntness, Figures 46 and 47.

10.4 Documentation of Wake Shape and Chordwise Distributions

In an effort to provide an extended documentation of the model predictions, Figures 48 through 51 show the [1] wake shapes and [2] pressure distributions for a NACA 0012 section at angles-of-attack between 2 and 16 degrees for chord based Reynolds numbers of 700,000 and 1,000,000.

Chapter 11

Conclusions

The current viscid-inviscid vortex panel method provides a reasonably accurate low Reynolds number flow model as shown in the comparisons with experimental data at Reynolds numbers of 700,000 and 1,000,000. Although provisions are not made for capturing [1] the structure of intermediate sized laminar separation bubbles and [2] the finite length of transition, the overall flow features were successfully modelled.

For a chord based Reynolds number of 700,000, it is shown that by removing the trailing 4 percent of a NACA 0012 airfoil section, the lift is reduced by only fractional amounts for angles-of-attack between 0 and 10 degrees. The resulting increase in trailing edge thickness relaxes the manufacturing and maintenance constraints associated with the more common sharp/cusped trailing edges.

It is also shown that for real flows with real fluids, the trailing edge conditions should always be that of zero net vorticity discharge into the downstream wake. Futher, it is shown that for sharp/cusped trailing edges, the trailing edge condition of zero net vorticity discharge essentially reduces to the more familiar Kutta condition of equal pressures at trailing edge upper and lower surfaces.

11.1 Recommendations

Future development should include extensions for modelling the structure of laminar separation bubbles and the finite length of transition. Futher provisions should be made for carrying out the boundary layer calculation through the point of separation and into the wake. A physically more realistic method of coupling the boundary layer parameters through transition would also enhance the model accuracy.

Appendix I

Application of Stratford's Criteria for Turbulent Separation

Stratford [ref 27] provides a technique for predicting the point of turbulent boundary layer separation from two-dimensional bodies in steady, incompressible flows.

At the point where the following equality is satisfied, the turbulent boundary layer is assumed to have separated form the body surface.

$$F(x) = N\beta \tag{0.1}$$

where the Stratford ratio, $F(x)$, is given as

$$F(x) = \frac{[2\bar{c_p}]^{\frac{1}{4}(n-2)}[\bar{x}\frac{d\bar{c_p}}{dx}]^{\frac{1}{2}}}{[10^{-6}\bar{R}e]^{\frac{1}{10}}} \tag{0.2}$$

only valid for

$$\bar{c_p} \leq \frac{4}{7} \tag{0.3}$$

The equivalent pressure coefficient, $\bar{c_p}$, is defined as

$$\bar{c_p} = \frac{p - p_0}{Q_0} = \frac{c_p - c_{p_0}}{c_{p_0}} \tag{0.4}$$

where suffix 0 refers to conditions at the point of minimum pressure and maximum velocity.

The variable $\bar{x}$ is defined as the equivalent distance over a constant pressure surface on which a turbulent boundary layer would develope a momentum thickness equal to that developed by laminar, then turbulent, boundary layer of the actual surface.

Thwaites provides an expression for the equivalent flat plate distance within the laminar boundary layer, valid up to the point of transition.

$$\bar{x}_1 = \int_{stag}^{x_1} [\frac{U}{U_1}]^5 dx \tag{0.5}$$

where the subscript $[]_1$ denotes an arbitrary point within the laminar layer. The corresponding momentum thickness, θ, can then be calculated according to

$$\theta_1 = \int_{stag}^{x_1} \frac{c_f}{2} d\bar{x} = \int_{stag}^{x_1} \frac{0.664}{2\sqrt{U\bar{x}_1/\nu}} d\bar{x} = 0.664[\frac{\nu}{U}\bar{x}_1]^{\frac{1}{2}} \tag{0.6}$$

Substitution yields an expression for the equivalent flat plate momentum thickness along the arbitrary two-dimensional surface within the laminar layer.

$$\theta_1 = 0.664[\frac{\nu}{U_1}\int_{stag}^{x_1} (\frac{U}{U_1})^5 dx]^{\frac{1}{2}} \tag{0.7}$$

The momentum thickness is taken as continuous through the point of transition so that, at transition, the initial equivalent momentum thickness [at the start of the turbulent layer] is given as

$$\theta_{trans} = 0.664[\frac{\nu}{U_{trans}}\int_{stag}^{x_{trans}} (\frac{U}{U_{trans}})^5 dx]^{\frac{1}{2}} \tag{0.8}$$

The equivalent turbulent distance up to the point of transition is calculated by invoking the expression for the turbulent momentum thickness developed over a flat plate.

$$\theta = 0.036\bar{x}_1^{\frac{4}{5}}[\frac{U_1}{\nu}]^{-\frac{1}{5}} \tag{0.9}$$

Finally, rearranging terms gives an expression for the equivalent turbulent distance up to the point of transition.

$$\bar{x}_{trans} = [\frac{\theta_{trans}}{0.036}]^{\frac{5}{4}}[\frac{U_{trans}}{\nu}]^{\frac{1}{4}} \tag{0.10}$$

Updating the equivalent turbulent distance beyond the point of transition depends on the proximity of the point of transition in relation to the minimum pressure point. If transition

occurs upstream from the minimum pressure point, the equivalent distance is updated according to

$$\bar{x}_1 = \bar{x}_{trans} + \int_{trans}^{X_1} [\frac{U}{U_1}]^3 dx \tag{0.11}$$

Downstream from the minimum pressure point, the equivalent turbulent distance is updated according to the actual body streamwise distance. The final expression becomes

$$\bar{x} = [\frac{0.664}{0.036}[\frac{\nu}{U_{trans}} \int_{stag}^{trans} (\frac{U}{U_{trans}})^5 dx]^{\frac{1}{2}}]^{\frac{5}{4}} [\frac{U_{trans}}{\nu}]^{\frac{1}{4}} + \int_{trans}^{0} (\frac{U}{U_0})^3 dx + \int_0^{separation} dx \tag{0.12}$$

Recalling the original Stratford criteria, N is defined as

$$N = 11.36 \frac{[n-2]^{\frac{n-2}{4}}}{[n+1]^{\frac{n+1}{4}} [n+2]^{\frac{1}{2}}} \tag{0.13}$$

where n is given as

$$n = log_{10} Re_s \tag{0.14}$$

and

$$Re_s = \frac{U_0 x_s}{\nu} \tag{0.15}$$

The variable x_s is continuously updated over the body surface as each panel control point is checked for separation.

The quantity $\bar{Re}$ is the equivalent Reynolds number based on U_0, the velocity at the minimum pressure point and the local equivalent turbulent distance.

$$\bar{Re} = \frac{U_0 x_s}{\nu} \tag{0.16}$$

Stratford points out that if a steep pressure rise occurs immediatley following transition, separation may be incorrectly predicted since the turbulent boundary layer may not be fully developed, rendering the the relations invalid.

Stratford gives two empirically derived values for beta depending on the local gradient of pressure in the streamwise direction.

$$\beta = 0.35 \quad for \quad \frac{d^2 p}{dx^2} \leq 0 \tag{0.17}$$

$$\beta = 0.39 \quad for \quad \frac{d^2p}{dx^2} > 0 \tag{0.18}$$

He shows that the criteria presented consistently underpredicts the point of separation by roughly five percent. He also points out that in regions of high, positive pressure gradients, acceptable predictions for the point of separation could only be obtained for increased values of beta (up to twenty percent).

Cebeci [ref 6] claims better agreement with experiment if a single value for beta is used without provisions for extreme gradients in pressure.

$$\beta = 0.5 \tag{0.19}$$

Empirical Determination of Beta

Stratford stresses the strong dependency of the parameter beta on the local streamwise gradient in pressure. He claims to about halve the error with his criteria for positive/negative gradients but suggests that a more extensive correlation be developed.

For a fixed Reynolds number, by varying the point of separation until the predicted lift coefficient matches that recognized by experiment, the dependency of beta on the local streamwise gradient in pressure can be defined. It is first necessary to set a baseline reference curve of lift coefficient versus angle-of-attack as a function of Reynolds number. Defining the curve at low Reynolds numbers is difficult since experimental data for low Reynolds number flows generally show unusually large amounts of scatter.

General Concerns

Stratford's method is intended to be used in conjunction with existing experimental data. In a single sweep, the criteria is to be applied to an already separated pressure distribution to determine the location of turbulent separation. Although predictions consistently fall

short of the experimental values by about five percent, the model maintaines it's popularity due to it's relative ease of numerical implementation.

For the current application, Stratford's separation criteria is coupled to a fully inviscid vortex panel method in an effort to provide an interactive separation model.

For each iteration, Stratford's criteria is first applied to the most current pressure distribution to determine the point of turbulent separation. With the new separation location defined, the inviscid solution is recalculated and the process repeated until a given set of convergence criteria is met.

It is observed that the scheme produces somewhat inconsistent output as a result of the inherent model underprediction for the point of separation. In the successive application of the separation criteria, the separation location shows a continuous upstream movement. The convergence criteria is eventually satisfied at a point considerably upstream from (and in error of) that recognized by experiment.

Inconsistencies also result from the model-enforced rear stagnation point, where the local trailing edge pressure gradients are unrealistically large and positive, leading to early predictions for the point of turbulent separation.

It is believed that Stratford's criteria should be reserved for real flows or viscous flow models. The criteria should not be applied in succession to the same pressure distribution due to the accumulation of errors associated with the inherent underprediction of the separation location.

Appendix II

Modelling the Finite Length of Transition

Consider a low Reynolds number flow with a weakly adverse pressure gradient. It is reasonable to assume that transition occurs before laminar separation sets in and that the process of transition from fully laminar flow to fully turbulent flow takes place out over a non-negligible distance. The resulting finite transition length, consisting of randomly intermittent pockets of laminar and turbulent flow, can have a large effect on airfoil performance.

Traditional modelling techniques normally assume either fully laminar or fully turbulent flow with transition occurring at a discrete point. In an effort to provide an improved low Reynolds number flow model, the following section suggests an alternate technique.

The proposed model is implemented in four steps.

1. Calculate the point of instability, where unstable two-dimensional Tollmien-Schlichting waves first appear.
2. Calculate the point where the flow becomes fully turbulent, thus defining the finite length of transition.
3. Assume a laminar-turbulent intermittency function over the finite length of transition.
4. Calculate the resulting bounday layer parameters through the finite transition length.

Onset of Transition

Assuming knowledge the external flow field, for each streamwise station along the body surface, Re_{δ^*}, the Reynolds number based on the local displacement thickness, is compared to the local value for $[Re_{\delta^*}]_{critical}$ to determine the onset of transition. The point of instability occurs when

$$Re_{\delta^*} = [Re_{\delta^*}]_{critical} \tag{0.20}$$

The quantity $[Re_{\delta^*}]_{critical}$ can be obtained from the results of Schlichting & Ulrich as outlined by White [ref 29]. Here the critical values for Re_{δ^*} are tabulated against Thwaites' λ.

$$\lambda = \frac{\theta^2}{\nu}\frac{dU_{edge}}{dx} \tag{0.21}$$

White also suggests an alternative method, derived from the Falkner-Skan profiles, employing the tabulated values of $[Re_{\delta^*}]_{critical}$ as a function of the parameter β.

$$\beta = \frac{2m}{1+m} \tag{0.22}$$

where

$$m = \frac{x}{U_{edge}}\frac{dU_{edge}}{dx} \tag{0.23}$$

Finite Length of Transition

Knowing the point of initial laminar boundary layer instability, the finite length of transition is calculated by invoking White's curve-fit to the experimental correlations of Granville [ref 29].

$$Re_\theta^{transition} \approx Re_\theta^{onset} + 450 + 400e^{60\lambda_m} \tag{0.24}$$

where λ_m is updated according to

$$\lambda_m = \frac{1}{x_{transition} - x_{onset}} \int_{x_{onset}}^{x_{transition}} \lambda(x)dx \tag{0.25}$$

and Re_θ is the Reynolds number based on the local momentum thickness.

$$Re_\theta = \frac{U_\infty \theta}{\nu} \tag{0.26}$$

White points out that for increasingly favorable pressure gadients (positive λ_m), the last term of Granville's correlation is large and the predicted lengths of transition increase. This agrees with observations that favorable pressure gradients generally possess higher degrees of inherent stability. Conversley, for the more adverse gradients associated with separated flows (negative λ_m), the last term in Granville's correlation is driven towards zero and the length of transition decreases.

The Intermittency Function

An intermittency function is introduced in an effort to provide a correlation between the laminar and turbulent flows within the finite length of transition. The function essentially provides a means for weighing the individual laminar-turbulent contributions to the resulting displacement thickness.

As a starting point, a symmetric distribution is suggested, Figure 80, although it may be discovered that other non-symmetric distributions provide a more realistic model. The only constraint is that the function ensures a 100 % laminar contribution at the onset of transition and a 0 % laminar contribution (100 % turbulent) at the end of the finite transition length.

Final Boundary Layer Calculation Through Transition

The turbulent boundary calculation is initiated at the onset of laminar instability. The laminar boundary layer calculation continues through transition and is carried out over the entire transition length. From the individual laminar and turbulent boundary layer

parameters, a weighted average is formed from the assumed intermittency function γ.

$$\delta^* = \gamma[\delta^*]_{laminar} + [1-\gamma][\delta^*]_{turbulent} \tag{0.27}$$

$$\theta = \gamma\theta_{laminar} + [1-\gamma]\theta_{turbulent} \tag{0.28}$$

$$H = \gamma H_{laminar} + [1-\gamma]H_{turbulent} \tag{0.29}$$

The new displacement thickness is then incorporated into the viscous boundary layer routine and the process repeated until convergence is achieved.

Implementation of the foregoing model was not carried out and the accuracy with which it models the true flow is presently unknown. It is believed, however, that the technique offers a physically more realistic approach to the modelling of the transition process at low Reynolds numbers, than the current model.

Appendix III

Compilation of Experimental Data [low Re]

In modelling steady flows over two-dimensional, airfoil-type bodies, it is important to have a good understanding of the physical processes involved, ensuring proper modelling of all flow regions. The baseline reference performance curves for typical two-dimensional bodies are often defined through wind tunnel tests. Without accurate experimental data, development and substantiation of numerical modelling techniques becomes a futile effort. McCroskey [ref 18] points out that

> " AERODYNAMIC RESULTS ARE SELDOM DUPLICATED IN DIFFERENT FACILITIES TO THE LEVEL OF ACCURACY THAT IS REQUIRED EITHER FOR RISK-FREE ENGINEERING DEVELOPMENT OR THE TRUE VERIFICATION OF THEORETICAL AND NUMERICAL MODELS. "

The wide scatter in data can be attributed to varying contributions from wind tunnel wall effects, support interference, free stream turbulence, surface roughness, acoustic virbation, approach-flow quality and/or data acquisition & reduction techniques.

Experimental Data

For a NACA 0012 airfoil section, it is found that as the chord based Reynolds number is reduced, the variability in data between test facilities is increased. The current section looks only at lift coefficient, c_ℓ, as a function of angle-of-attack for Reynolds numbers in the 125,000 to 1,000,000 range.

Of the data [ref's 8,13,16,18,19,21,25,30] which were examined, two were extracted form the reference list of Schlichting & Truckonbrodt's *Aerodynamics of the Airplane* [ref 23] while the remaining came from McCrosky's survey on NACA 0012 wind tunnel experiments [ref 18].

Figures 53 and 54 show the experimentally measured lift coefficients as a function of angle-of-attack for chord based Reynolds numbers of 700,000 and 1,000,000. Figures 55, 56 and 57 show the section lift coefficients as functions of Reynolds number for 4, 10 and 16 degrees angle-of-attack from a number of different sources, including the current model predictions. The variation between test facilities is visually large, especially for lower chord based Reynolds numbers.

Appendix IV

Code Documentation

The following section provides a brief guide for running the current version of the program **LFLY**. The inviscid model is adapted from the masters thesis of Burns [ref 3] while the viscous routine is developed entirely by the author.

The program **LFLY** and the support plotting routines **CPS**, **SHP** and **HPLOT** are stored on magnetic tape [labeled **LFLY**] which may be obtained from Professor Covert.

Flow Charts

Figure 58 shows a flow chart of the global viscid/inviscid computational algorithm while Figure 59 specifically details the boundary layer routine. It should be noted that only the larger subroutines are shown in the charts. The smaller routines performing a more simple task are not mentioned since their functions are usually described in the routine which calls them.

Defining the Input Files

Prior to the execution of the viscid-inviscid model, five input files must be set:

1. **LFLY.xxx**
2. **LFLY.NUM**
3. **LFLY.SEP**

4. **LFLY.INC**

5. **TEDGE.INC**

where the extension xxx refers to the current run number which may range from 001 to 999.

The first input file **LFLY.xxx** [reproduced below] sets such parameters as airfoil type, Reynolds number, chord length, number of wing and wake panels, etc ... It is the main input file and must be created for each run executed.

```
001          ! run number xxx this file is lfly.xxx
0.7          ! Reynolds number based on root wing chord
1            ! nw number of wings
0012         ! stype (naca xxxx airfoil) -10 for tunnel
0,0          ! x0, z0 input for wing number 1
2.0          ! angle of attack
0            ! dihedral
0            ! om1 sweep of le
0            ! om2 sweep of te
1.0          ! c root chord
1000.0       ! s (b/2) 1/2 span
1            ! ns spanwise panels
55           ! nc chordwise panels
5            ! ncwak chordwise wake panels
0.05         ! initial wake length in units of chord
```

The programs are currently set for investigating the effects of trailing edge bluntness on airfoil performance. If the input chord length is set to a value less than one, the program

will cut off the specified airfoil section at the requested chord length. For a full airfoil section, the users must set the chord length to the value of 1. This feature may be adjusted by re-coding subroutines **LGEOM** and **LWING**.

The ***distribution*** of wing and wake panels is current set for a cosine distribution over the first ten percent of the wing chord and a uniform distribution thereafter. To set the ***number*** of panels, the input file **LFLY.xxx** must be adjusted along with the parameters **itpan** and **tchord** found within file **TEDEG.INC**. **Itpan** is taken as the number of uniform panels [excluding wake] aft of **tchord**, the point where the leading edge cosine distribution ends.

Adjustments to the ***distribution*** of wing/wake panels may be carried out by re-coding the subroutines **LGEOM, LPOSX** and **LCPOUT** as well as the support plotting routine **CPS**.

The input file **LFLY.SEP** sets the initial upper surface separation location. It's value sets the panel number on which separation occurs as counted upstream from the upper surface trailing edge.

The input file **LFLY.NUM** sets the run number. The number in it must coincide with the run number specified in **LFLY.xxx** or an error message will result and the program will be aborted.

The input file **LFLY.INC** sets the array sizes for the calculation. In particular, it sets the maximum number of [1] panels, [2] wings, [3] spanwise stations, [4] chordwise stations and [5] number of iterations.

Common Blocks

Since the program **LFLY** relies heavily on the use of common blocks, a brief description of each follows.

BLDAT.CMN	boundary layer data
LHIST.CMN	iteration history of c_ℓ and $c_{m_{l.e.}}$
LCHAR.CMN	title and run
LWING1.CMN	wing input data
TEDGE.INC	panel number/distribution
EPS1.INC	maximum panel through-flow
LFLY.INC	array sizes
LWING2.VAR	wing input data

Description of Subroutines

The following list describing the main subroutines of program **LFLY** is a supplement to the flow charts of Figures 58 and 59.

LFLY	main program
LFLY1	wing configuration and set-up
LFLY2	velocity matrix calculation
LFLY3	viscous analysis
L1INPU	reads input files
L2INPU	reads input files
L3INPU	reads input files
LGEOM	wing and tunnel geometry
LWING	calculates wing profile
LTUN	calculates tunnel geometry
LWNGCO	calculates wing vorticities
LVELOC	calculates local panel velocities

CONV	checks for convergence
LBLTX	main boundary layer routine
BLSHIFT	adjusts displacement surface
WKSHIFT	adjusts wake length
LAMDEL	upper surface laminar boundary layer
LLAMDEL	lower surface laminar boundary layer
BL_UPPER	upper surface turbulent boundary layer
BL_LOWER	lower surface turbulent boundary layer
UGRX	calculates velocity gradients [stagnation]
UGRAD	calculates velocity gradients
LPOSX	calculates chordwise panel location
LGLOB	writes output parameters to disk

Compiling and Linking

The four main programs have auxiliary command files for compiling and linking the subroutines [and graphics package, when applicable]. To compile or link a program with it's subroutines simple type the name of the program preceded by an @ sign and followed by a c [for compile] or an l [for link]. For example, the program **LFLY** is compiled and linked by typing the following two commands: [1] **@LFLYC** and [2] **@LFLYL**. The same holds true for programs **CPS**, **SHP** and **HPLOT**.

Running a Batch Job

Running the program **LFLY** on batch on the microVAX or VAX systems while maintaining a log on your disk without going to the line printer, is carried out by typing the following command sequence:

submit FILENAME/keep/noprinter

where **FILENAME** is the name of the input command file **FILENAME.COM**, containing the command sequence similar to the one shown below.

```
$ @zero              ! sets the separation location to the trailing edge
$ run inc            ! increments the run number forward by one
$ run lfly           ! runs the main program
$ purge lfly.num     ! purges old files
$ purge lcl1.*       ! purges old files
$ purge lcm1.*       ! purges old files
$ purge seploc.*     ! purges old files
$ del lfly1u.*;*     ! deletes old files
```

Output Files

The outputs from the flow model are the upper and lower surface chordwise distributions of pressure coefficient, $c_p(x)$, displacement thickness, $\delta^*(x)$, momentum thickness, $\theta(x)$ and shape factor, $H(x)$. Also included are the upper and lower surface chordwise points of laminar separation-reattachment, transition and turbulent separation. In addition, the airfoil geometry and wake shape are output along with the iteration histories of lift coefficient and moment coefficient. The following list summarizes the output files.

LCP111.xxx	upper surface distribution of pressure coefficient, $c_p(x)$
LCP112.xxx	lower surface distribution of pressure coefficient, $c_p(x)$

DELXHI.xxx	upper surface distribution of displacement thickness, $\delta^*(x)$
DELXLO.xxx	lower surface distribution of displacement thickness, $\delta^*(x)$
XMOMHI.xxx	upper surface distribution of momentum thickness, $\theta(x)$
XMOMLO.xxx	lower surface distribution of momentum thickness, $\theta(x)$
HFACHI.xxx	upper surface distribution of shape factor, $H(x)$
HFACLO.xxx	lower surface distribution of shape factor, $H(x)$
LSHAPE1.xxx	airfoil geometry
LSHAPEX.xxx	displacement surface
LCL1.xxx	lift coefficient, c_ℓ, versus iteration
LCM1.xxx	moment coefficient, $c_{m_{l.e.}}$, versus iteration
LCLF.xxx	average of last four lift coefficients, c_ℓ
SEPLOC.xxx	upper and lower surface separation locations, x_{sep}, versus iteration
SEPDAT.xxx	stagnation point location
	upper and lower surface chordwise locations for:
	[1] point of laminar separation
	[2] point of reattachment [if occurs]
	[3] point of turbulent separation

In addition, the upper and lowers surface distributions of vorticity are internally calculated and may be accessed by re-coding subroutine **LGLOB**.

Plotting Packages

Three plotting packages [which access the Aero/Astro system graphics routine **GRAFIC**] are provided, **CPS**, **SHP** and **HPLOT**.

Program **CPS** allows for the plotting of the upper and lower surface distributions of pressure coefficient. The only inputs requested by the user are the run number and whether

$c_p(x)$ or $\Delta c_p(x)$ is to be plotted.

Program **SHP** allows for the plotting of the airfoil with it's current displacement surface. The only required input is the run number.

Program **HPLOT** is a generic plotting routing used for displaying the distributions of momentum thickness, displacement thickness, shape factor, etc ...

Extensions

The inviscid code was originally designed to operate in three dimensions with the inclusion of wind tunnel walls. The addition of the boundary layer routine constrained the model to isolated airfoils in two dimensions. Wind tunnel walls can be added with only slight modifications to the subroutine . The final extension of the viscous routine to three dimensions will be a somewhat more involved process, but can surely be completed in several weeks time. Burn's [ref 3] thesis would be beneficial in performing this task.

Reference List

1. Batchelor, G.K., AN INTRODUCTION TO FLUID DYNAMICS, Cambridge University Press, 1967.

2. Bradshaw, P., Cebeci, T. and Whitelaw, J.H., ENGINEERING CALCULATION METHODS FOR TURBULENT FLOWS, Academic Press, 1981.

3. Burns, J.H., *"A 3-D Tunnel Correction Panel Method for Swept Tapered Airfoils with Separation,"* MIT Thesis, Department of Aeronautics and Astronautics, 1988.

4. Bushnell, D.M., Lazos, B.S. and Wilkinson, S.P., *" Turbulent Drag Reduction Research at NASA Langley: Progress and Plans,"* Int. J. Heat and Fluid Flow, Vol. 9, No. 3, September 1988, pp. 266-277.

5. Cebeci, T. and Bradshaw, P., MOMENTUM TRANSFER IN BOUNDARY LAYERS, Hemisphere Publishing Co., 1977.

6. Cebeci, T., Mosinskis, G.J. and Smith, A.M.O., *" Calculation of Separation Points in Incompressible Turbulent Flows,"* Journal of Aircraft, Vol. 9, No. 9, 1971, pp.618-624.

7. Chang, P.K., SEPARATION OF FLOW, Pergamon Press, 1970

8. Critzos, C.C., Heyson, H.H. and Boswinkle, R.W., *" Aerodynamic Characteristics of NACA 0012 Airfoil Section at angles-of-attack from zero to 180 degrees,"* NACA TN 3361, 1955.

9. Gastner, M., *" The Structure and Behavior of laminar Separation Bubbles,"* ARC R & M 3595, 1969.

10. Head, M.R., " *Entrainment in the Turbulent Boundary Layers,* " ARC R & M 3152, 1958.

11. Head, M.R. and Patel, V.C., " *Improved Entrainment Method for Calculating Turbulent Boundary Layer Development,* " ARC R & M 3643, 1969.

12. Howarth, L., " *The Theoretical Determination of the Lift Coefficient for a Thin Elliptic Cylinder,* " Procedings of the Royal Society of London, Vol. 149A, 1935, pp. 558-586.

13. Jacob, E.N. and Sherman, A., " *Airfoil Section Characteristics as Affected by Variations of the Reynolds Number,* " NACA Report 586, 1937.

14. Kline, S.J., P., Bardina J.G. and Strawn, R.C., " *Correlation of the Detachment of Two-Dimensional Turbulent Boundary Layers,* " AIAA Journal, Vol. 21, No. 1, January 1983, pp. 68-73.

15. Lighthill, M.J., " *A Note on Cusped Cavities,* " ARC R & M 2328, 1945.

16. Loftin, L.K. and Smith, H.A., " *Aerodynamic Characteristics of Fifteen NACA Airfoil Sections at Seven Reynolds Number from 700,000 to 9,000,000,* " NACA TN 1945, 1949.

17. Maskew, B. and Dvorack, F.A., " *The Prediction of Clmax Using a Separated Flow Model,* " Journal of American Helicopter Society, April 1978.

18. McCroskey, W.J., " *A Critical Assessment of Wind Tunnel Results for the NACA 0012 Airfoil,* " NASA TM 100019, October 1987.

19. Moran, J., AN INTRODUCTION TO THEORETICAL AND COMPUTATIONAL AERODYNAMICS, John Wiley & Sons, 1984.

20. Owen, P.R. and Klanfer, L., " *On the laminar Boundary layer Separation from the Leading Edge of a Thin Aerofoil,* " ARC CP 220, 1950.

21. Pinkerton, R.M., *" The Variation with Reynolds Number on the Pressure Distribution over Airfoil Sections, "* NACA Report 613, 1938.

22. Schlichting, H., BOUNDARY LAYER THEORY, McGraw-Hill, 1979.

23. Schlichting, H. and Truckenbrodt, E., AERODYNAMICS OF THE AIRPLANE, McGraw-Hill, 1979.

24. Sears, W.R., *" Unsteady Motion of Airfoils with Boundary-Layer Separation, "* AIAA Journal, Vol. 14, No. 2, February 1976, pp. 216-220.

25. Sheldahl, R.E. and Klimas, P.C., *" Aerodynamic Characteristics of Seven Symmetrical Airfoil Sections through 180 degrees angle-of-attack for use in Aerodynamic Analysis of Vertical Axis Wind Turbines, "* Sandia Nat. Labs Report, SAND80-2114, 1981.

26. Strang, G., INTRODUCTION TO APPLIED MATHEMATICS, Wellesley-Cambridge Press, 1986.

27. Stratford, B.S., *" The Prediction of Separation of the Turbulent Boundary Layer, "* National Gas Turbine Establishment, Farnborough, 1958.

28. Tran-Cong, T., *" A Potential Theory for the Steady Separated Flow about an Aerofoil Section, "* Ingenieur-Archiv 58, 1988, pp. 285-294.

29. White, F.M., VISCOUS FLUID FLOW, McGraw-Hill, 1974.

30. Wortmann, F.X., *" Design of Airfoils with High Lift at Low and Medium Subsonic Mach Numbers, "* AGARD CP-102, 1972.

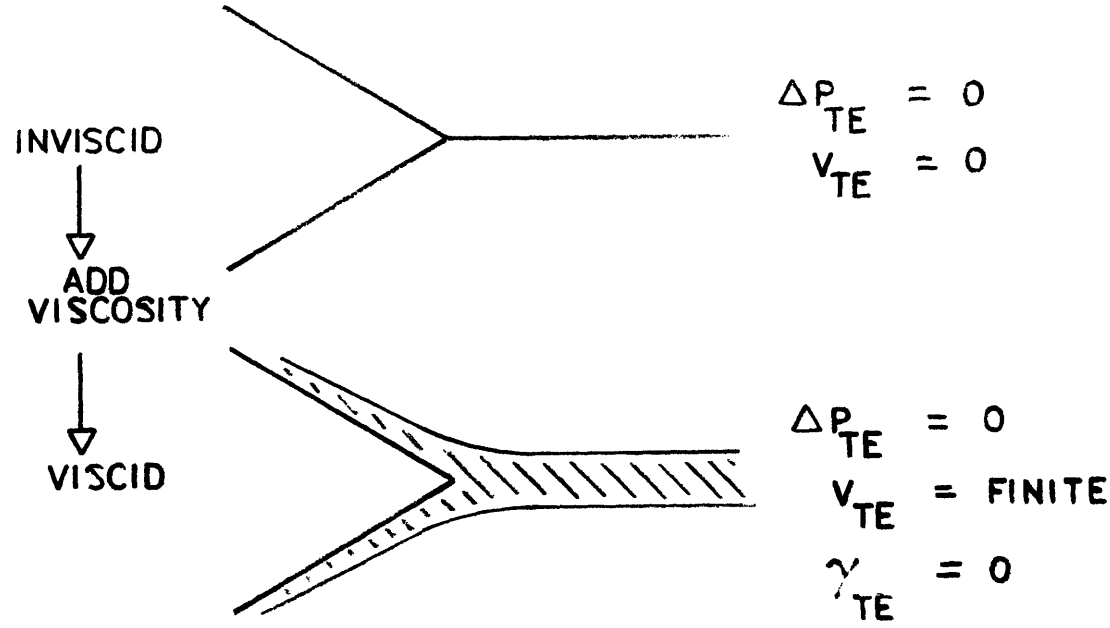

Figure 1: Sharp trailing edge and the effect of viscosity.

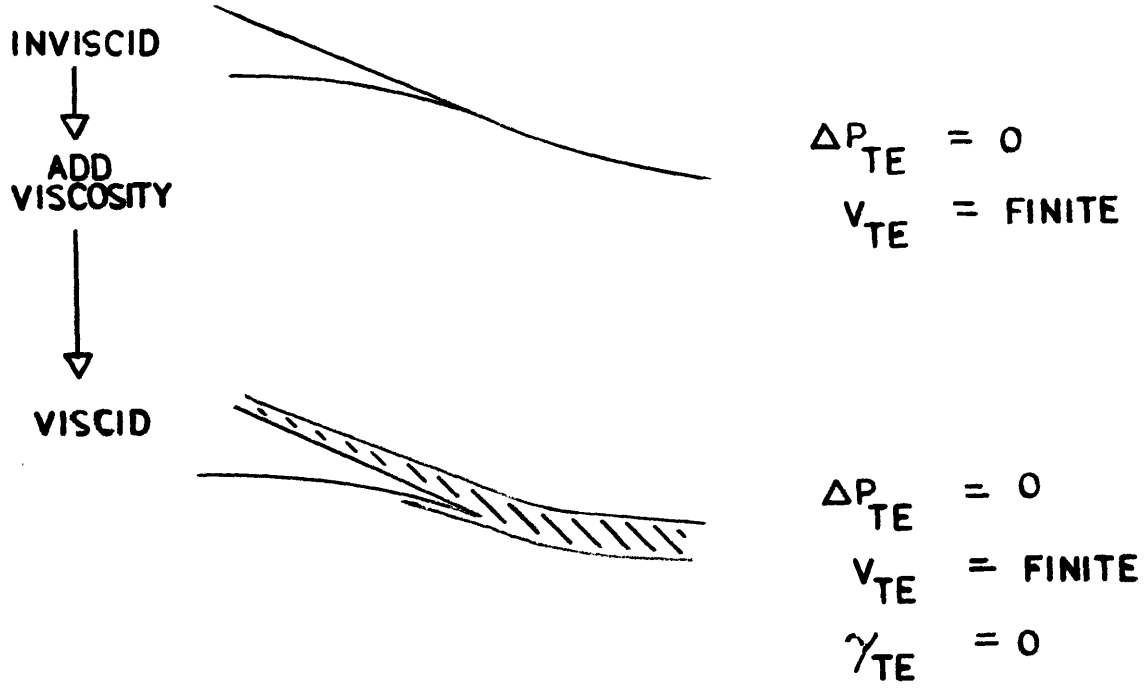

Figure 2: Cusped trailing edge and the effect of viscosity

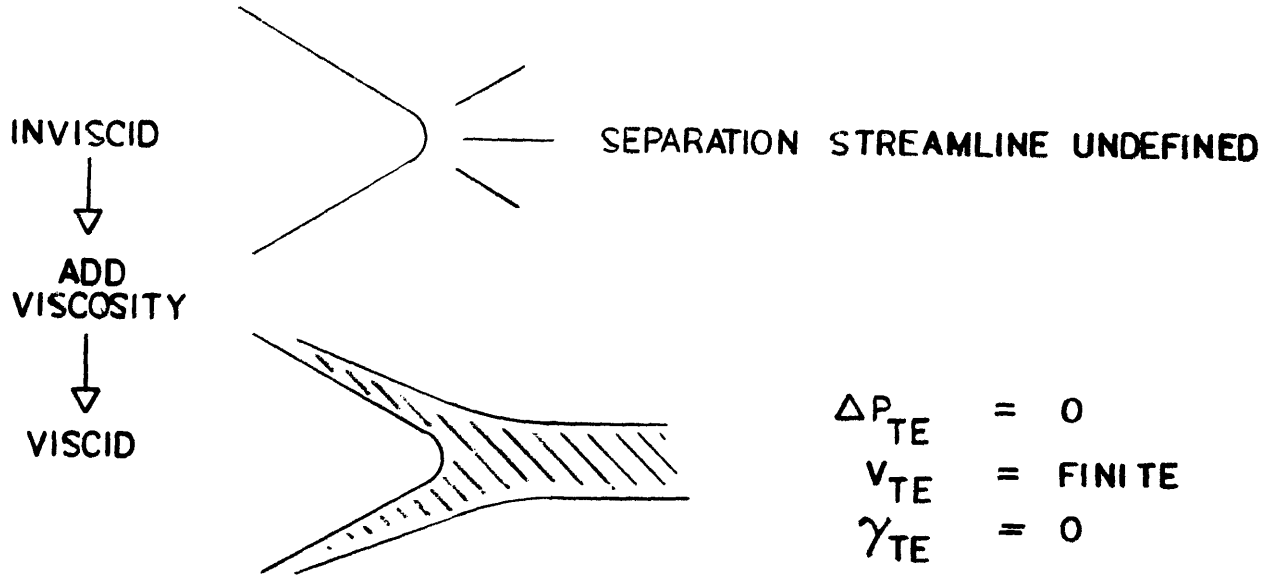

Figure 3: Blunt trailing edge and the effect of viscosity.

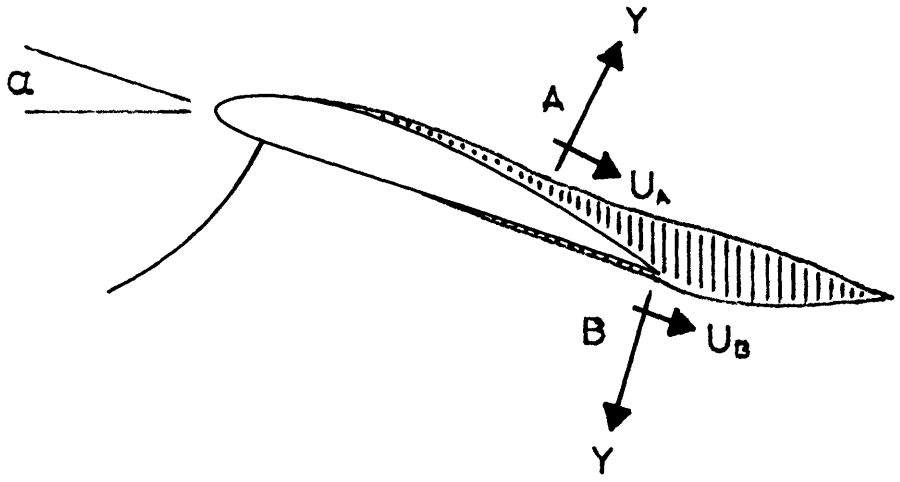

Figure 4: Fixed airfoil in steady flow with upper and lower surface boundary layer separation at points A and B.

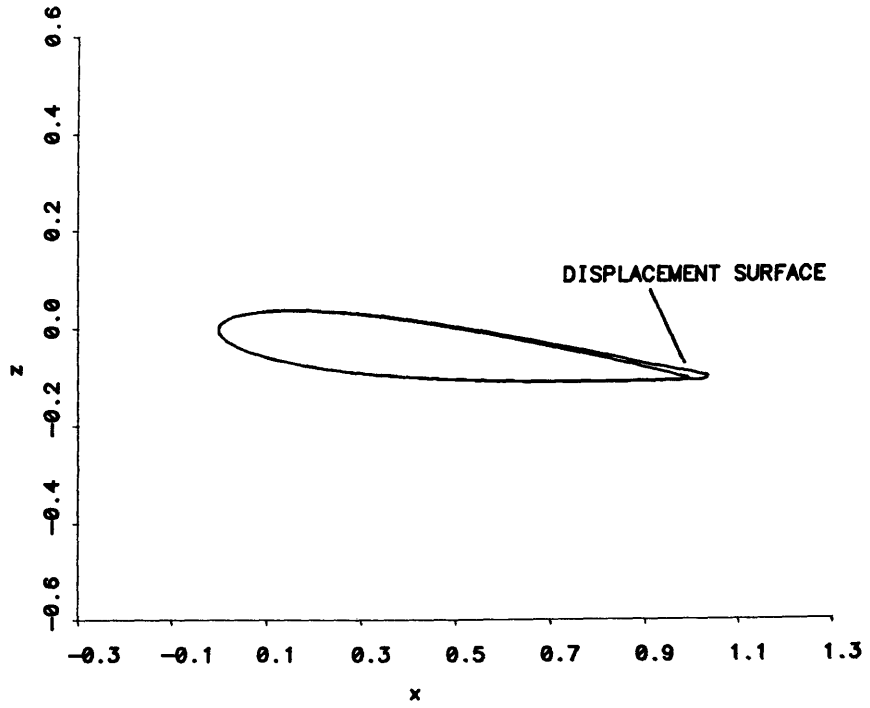

Figure 5: Displacement surface, NACA 0012, AOA= 4°, Re=700,000.

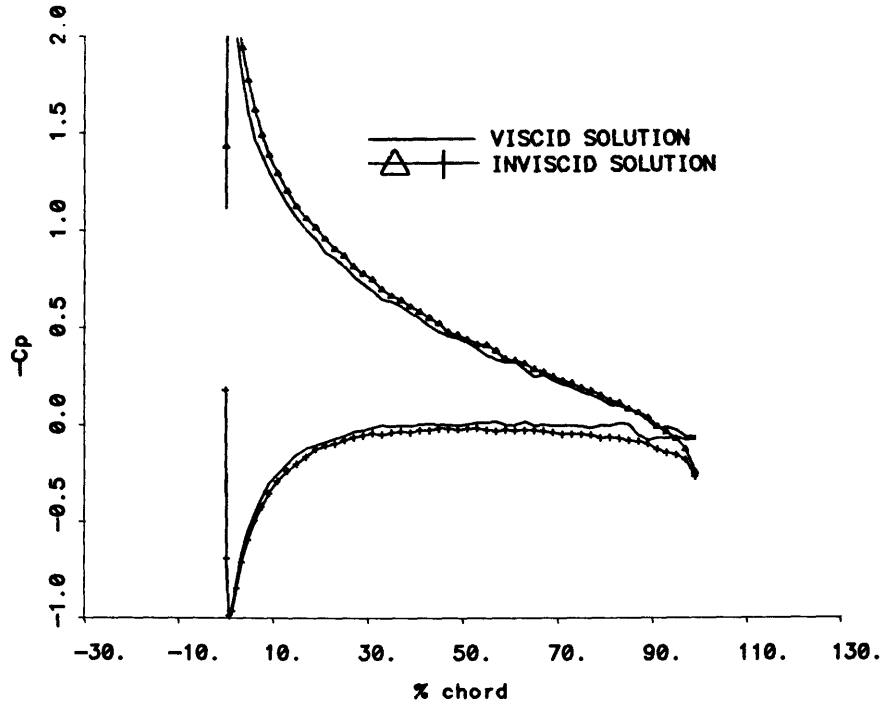

Figure 6: Viscid and inviscid pressure distributions, NACA 0012, AOA= 4°, Re=700,000.

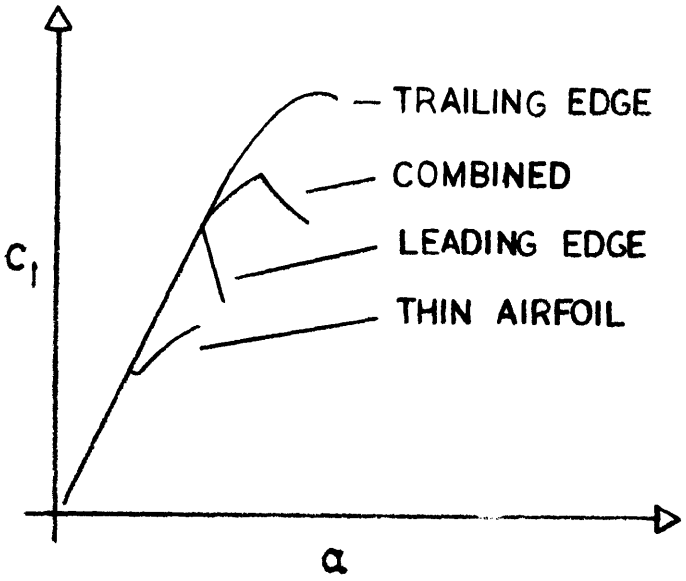

Figure 7: Decay in lift coefficient, c_ℓ, for each stall class [1] leading edge, [2] trailing edge, [3] thin airfoil and [4] combined.

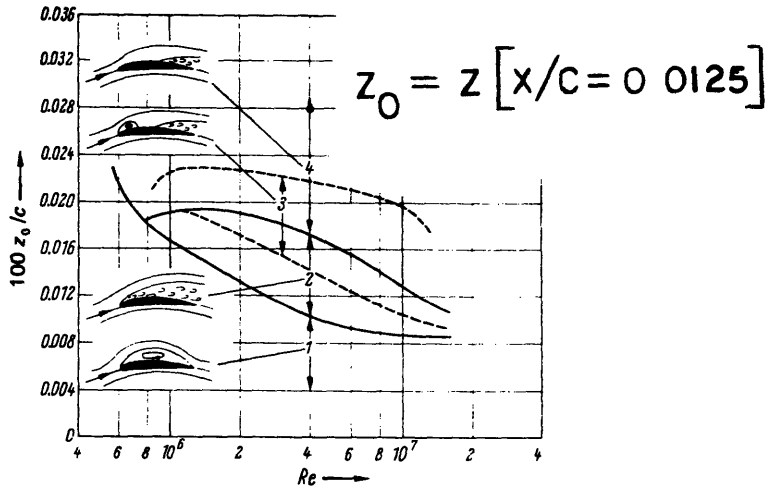

Figure 8: Stall type classification as a function of Reynolds number and leading edge radius of curvature, from SCHLICHTING [ref 23].

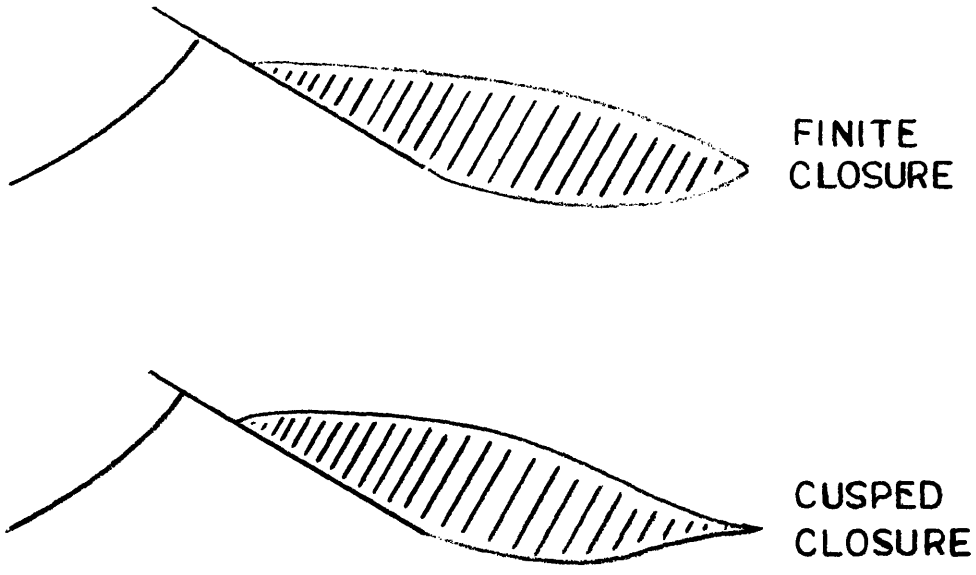

Figure 9: Allowable wake shapes, cusp and finite angle.

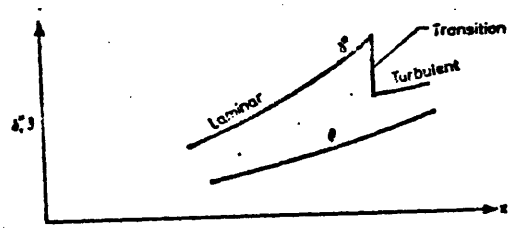

Figure 10: Progression of displacement thickness, δ^*, and momentum thickness, θ, through transition, from CHANG [ref 7].

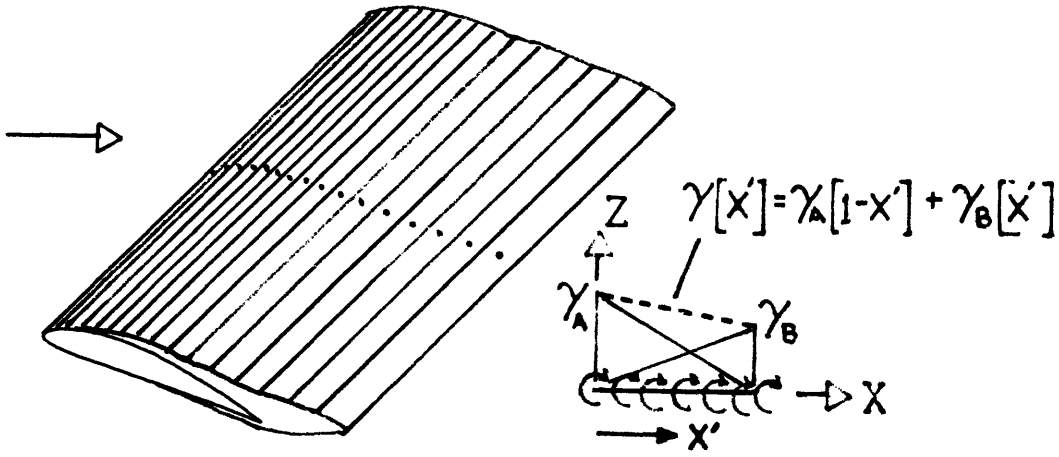

Figure 11: Wing configuration, 2-d vortex panel method.

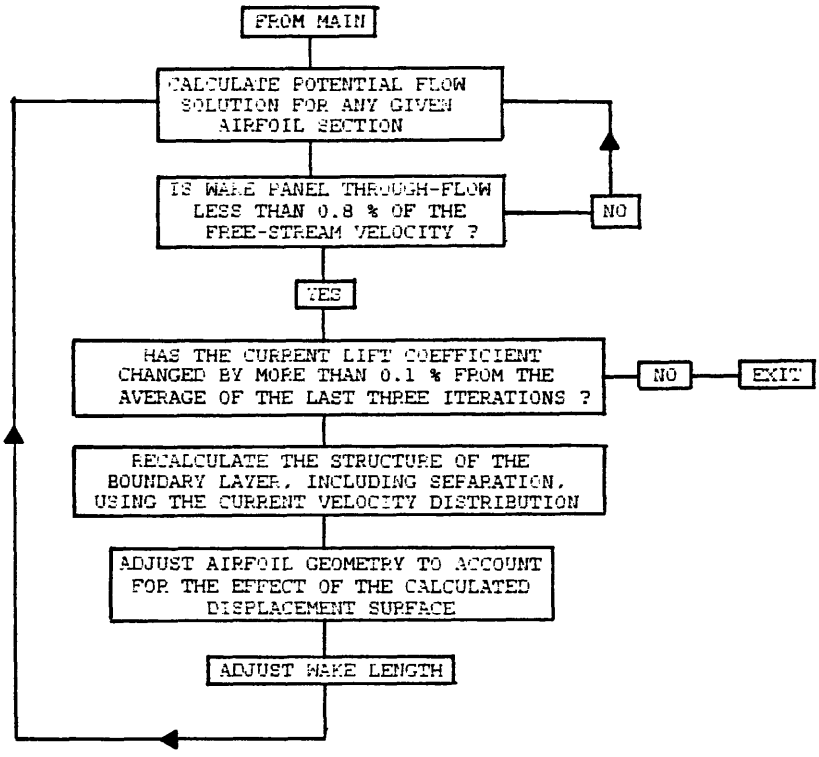

Figure 12: Flow chart of computational algorithm.

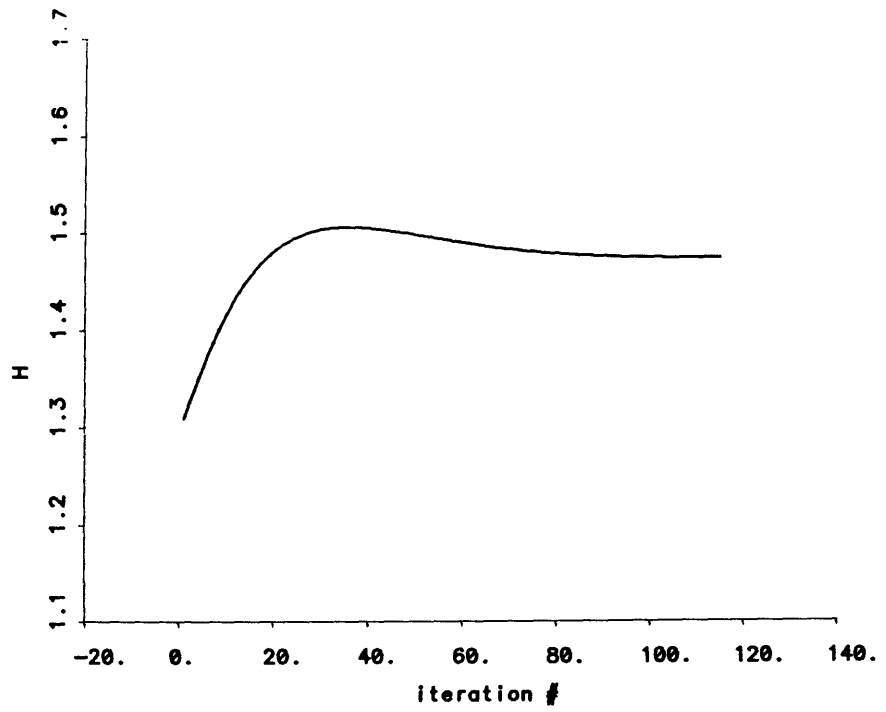

Figure 13: Convergence of the true shape factor, H, method of steepest descent, NACA 0012, AOA= 4°, Re=700,000, at mid-chord point.

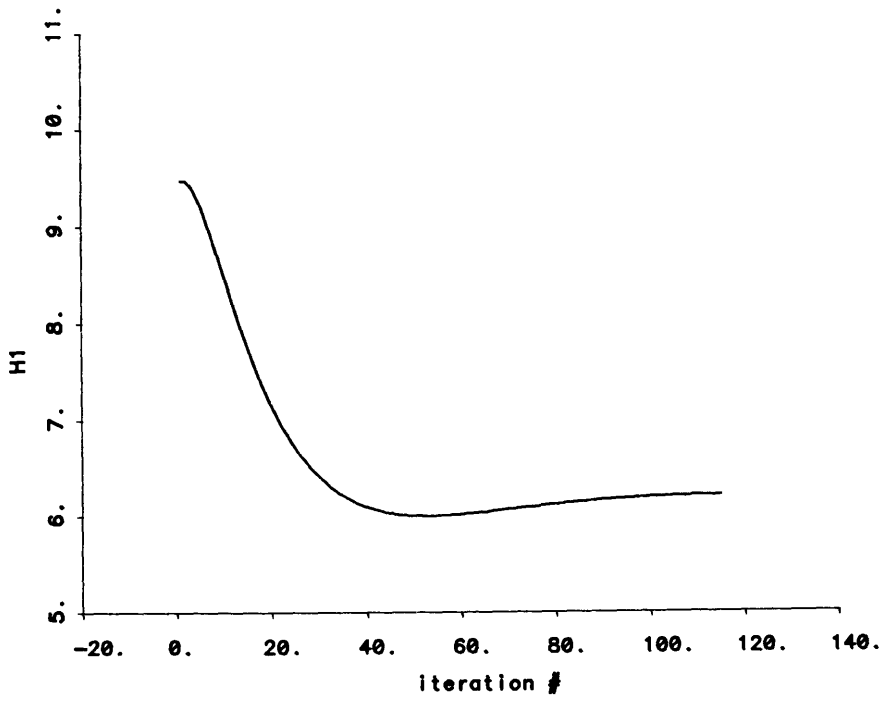

Figure 14: Convergence of the modified shape factor, H_1, method of steepest descent, NACA 0012, AOA= 4°, Re=700,000, at mid-chord point.

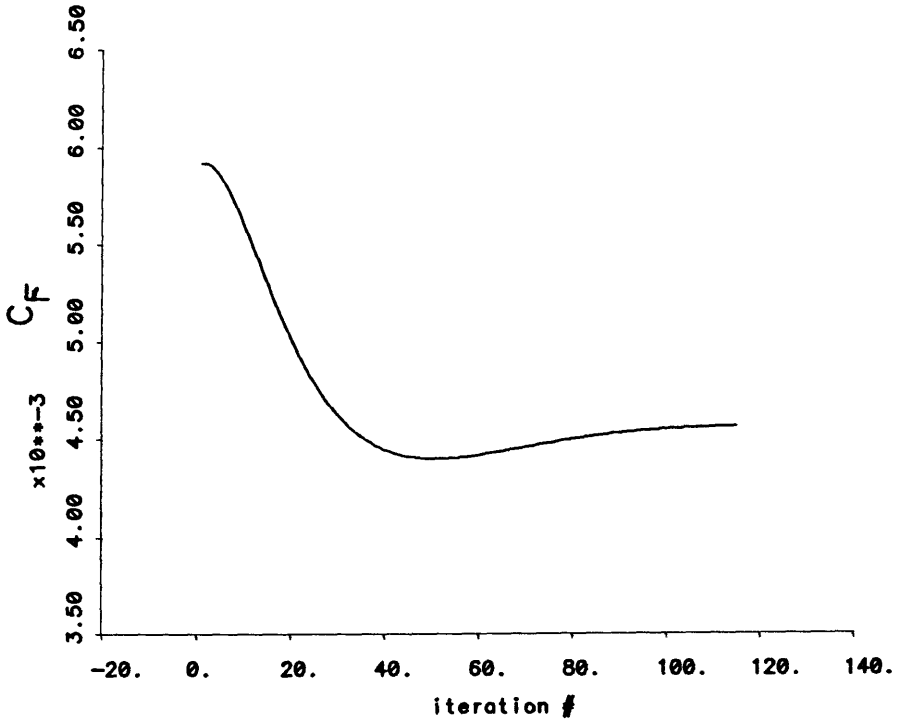

Figure 15: Convergence of the skin friction coefficient, c_f, method of steepest descent, NACA 0012, AOA= 4°, Re=700,000, at mid-chord point.

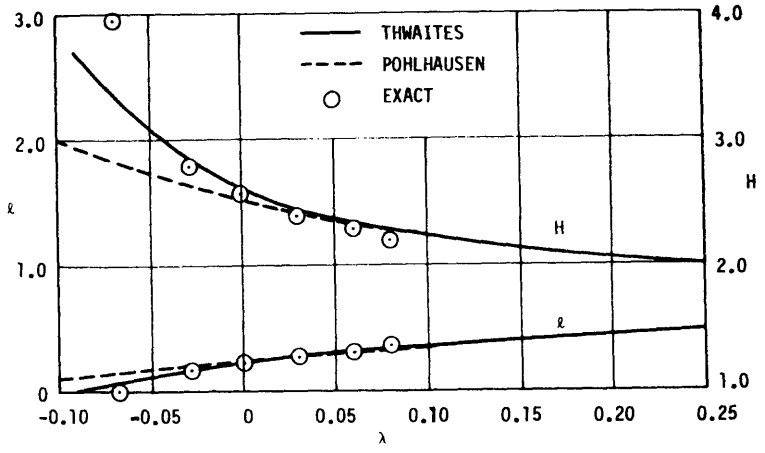

Figure 16: Sensitivity of shape factor, H, to Thwaites' lambda, λ, from CEBECI & BRADSHAW [ref 5].

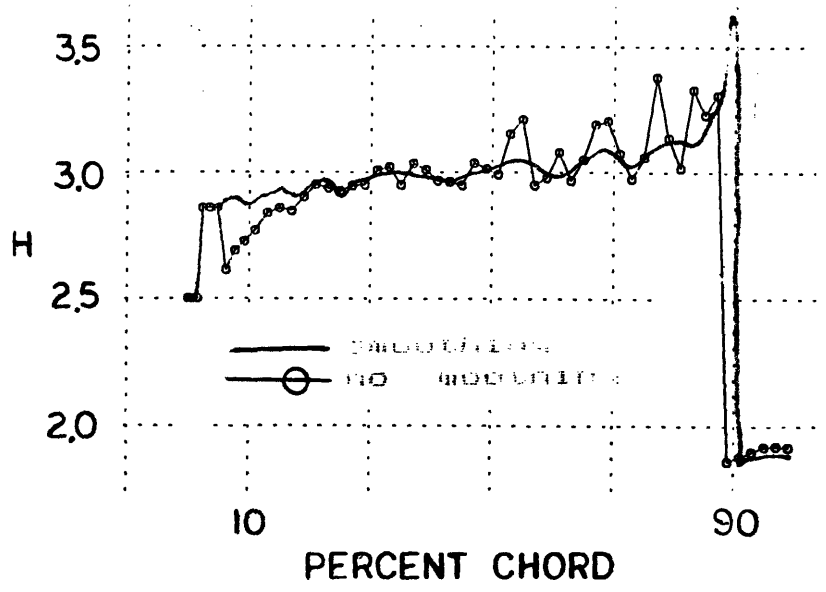

Figure 17: Effect of smoothing on laminar displacement thickness, δ^*, NACA 0012, AOA= 4°, Re=700,000.

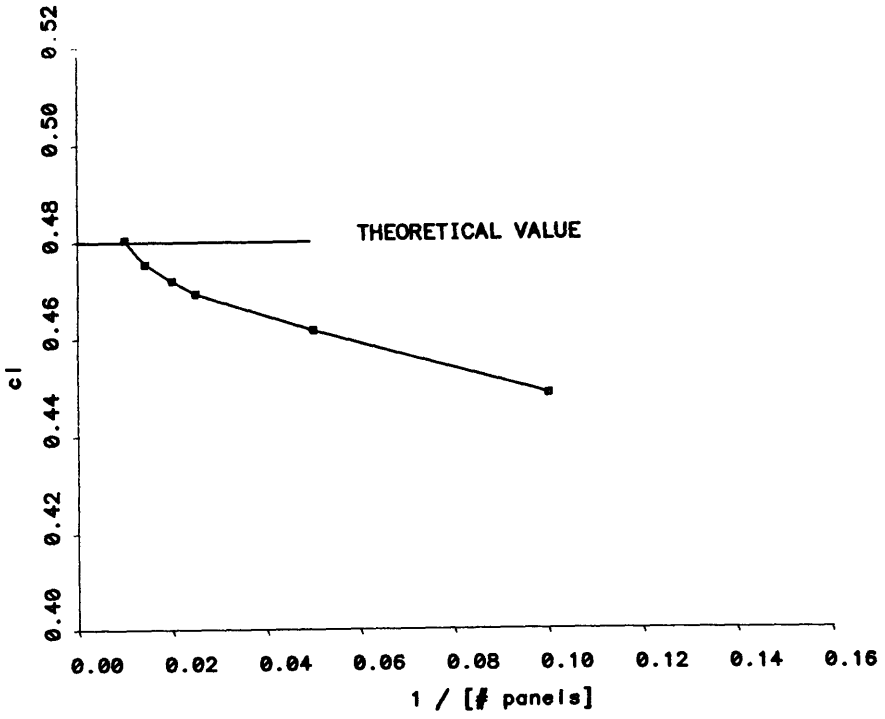

Figure 18: Sensitivity of lift coefficient, c_ℓ, to varying numbers of uniformly distributed wing-wake panels, NACA 0012, AOA= 4°, Re=700,000, fully attached.

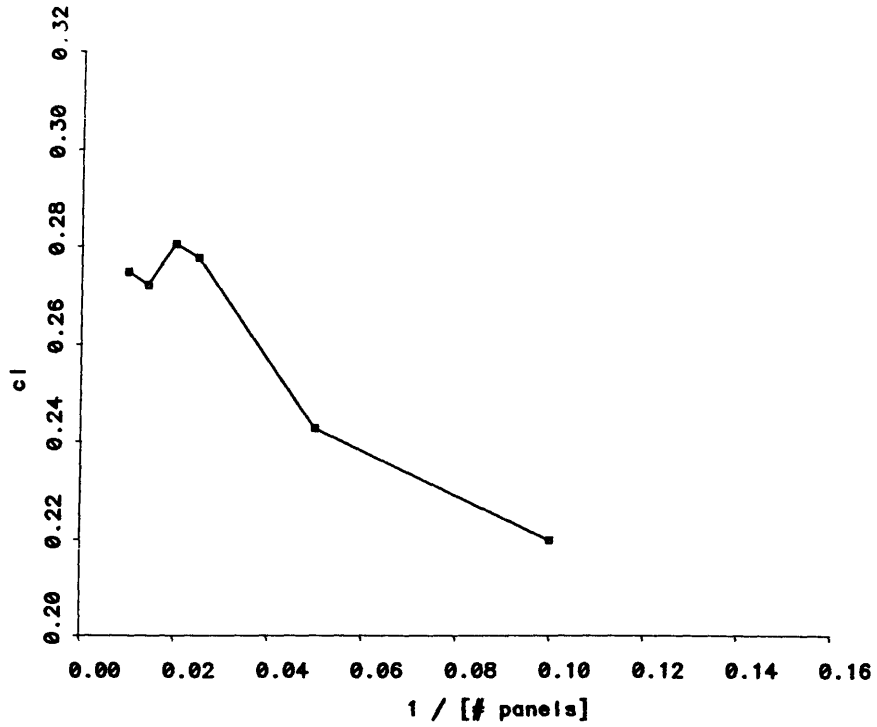

Figure 19: Sensitivity of lift coefficient, c_ℓ, to varying numbers of uniformly distributed wing-wake panels, NACA 0012, AOA= 4°, Re=700,000, separation at 90 %.

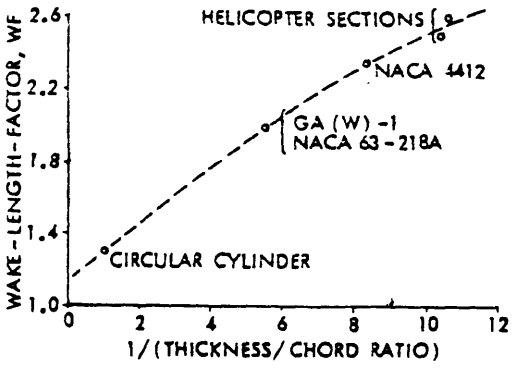

Figure 20: *WAKE FACTOR* as a function of airfoil thickness, from MASKEW & DVORACK [ref 17].

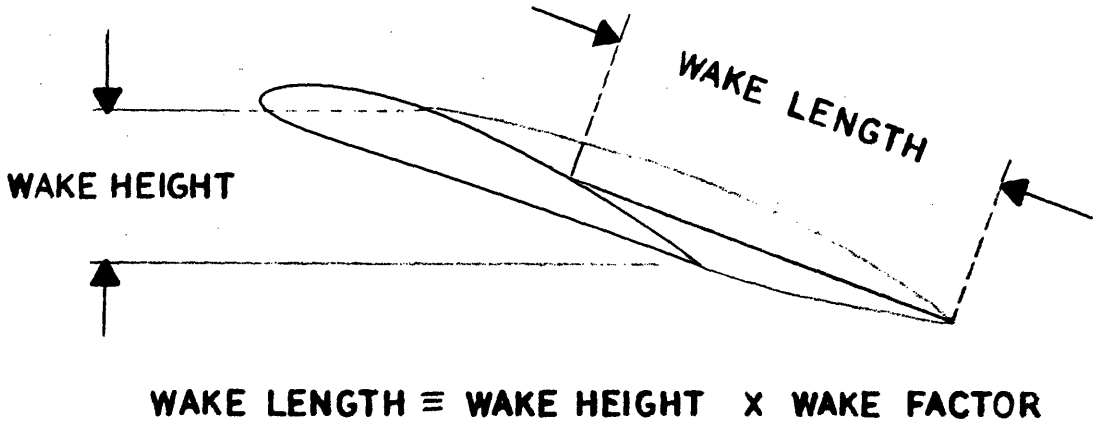

Figure 21: Reference sketch for the calculation of wake length.

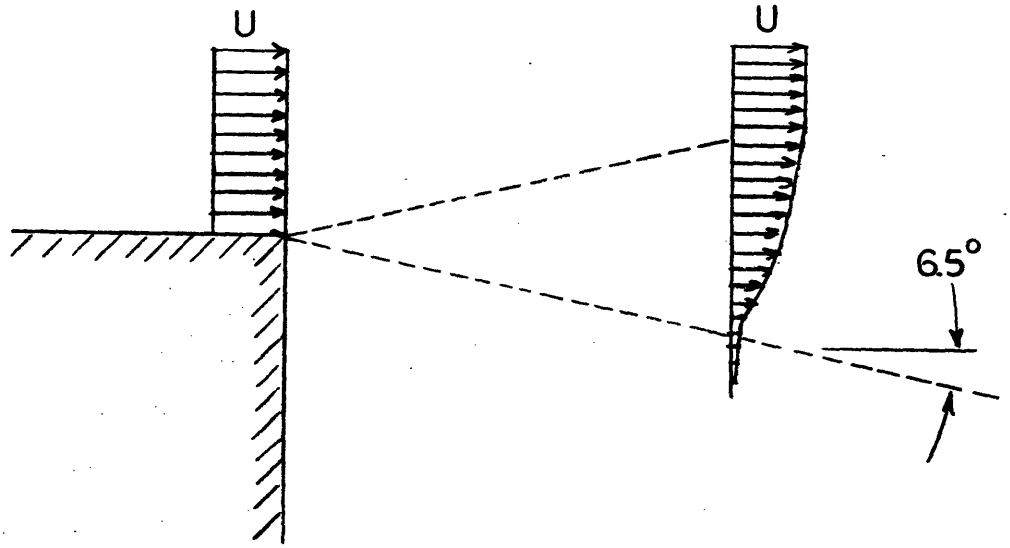

Figure 22: Typical jet boundary.

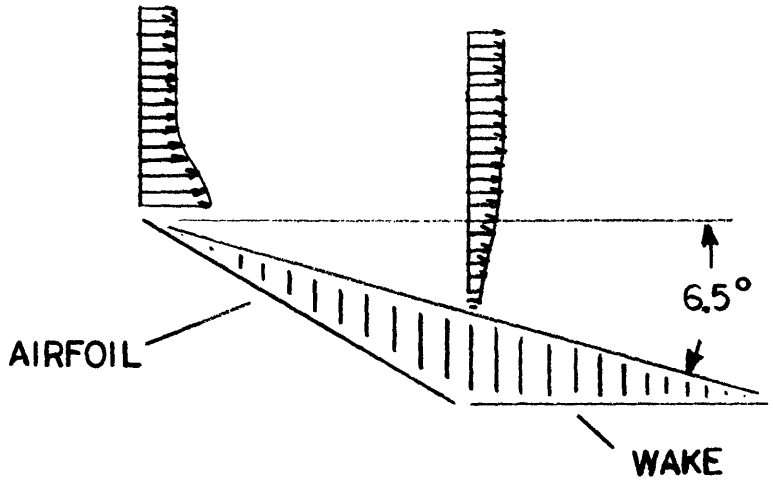

Figure 23: Jet boundary analogy to leading-trailing edge flow sepration.

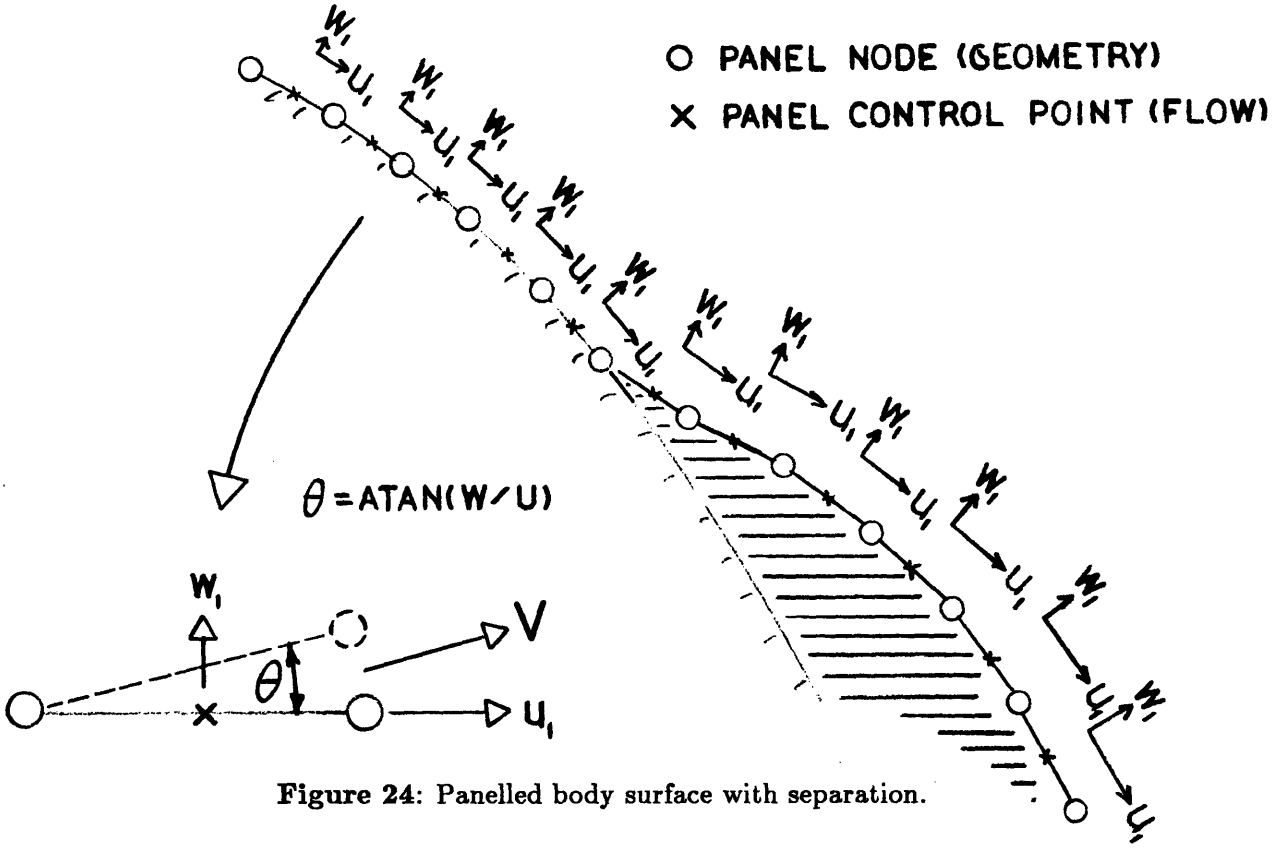

Figure 24: Panelled body surface with separation.

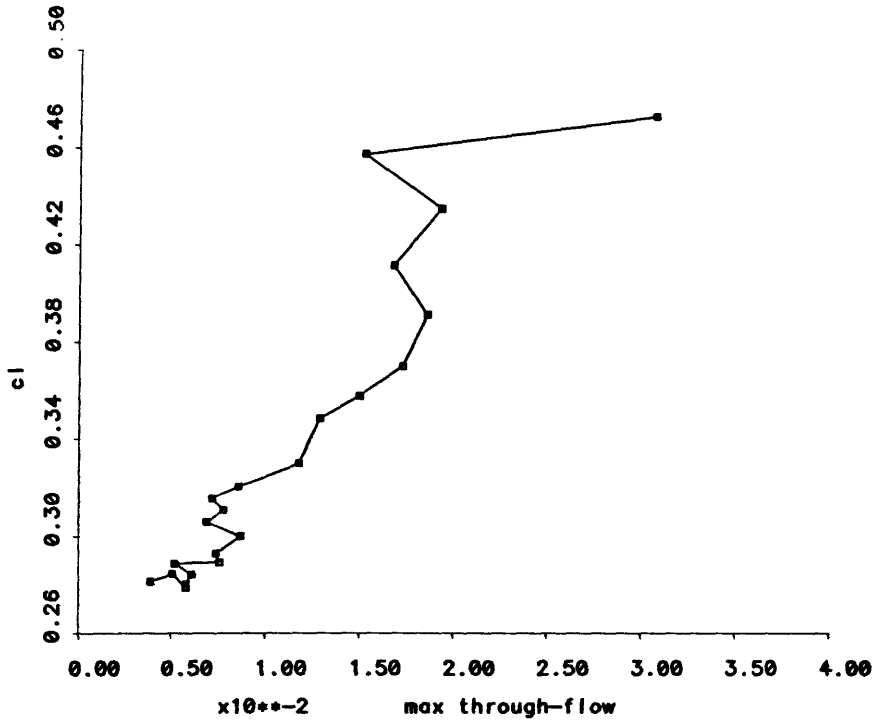

Figure 25: Lift coefficient, c_ℓ, sensitivity to maximum panel through-flow.

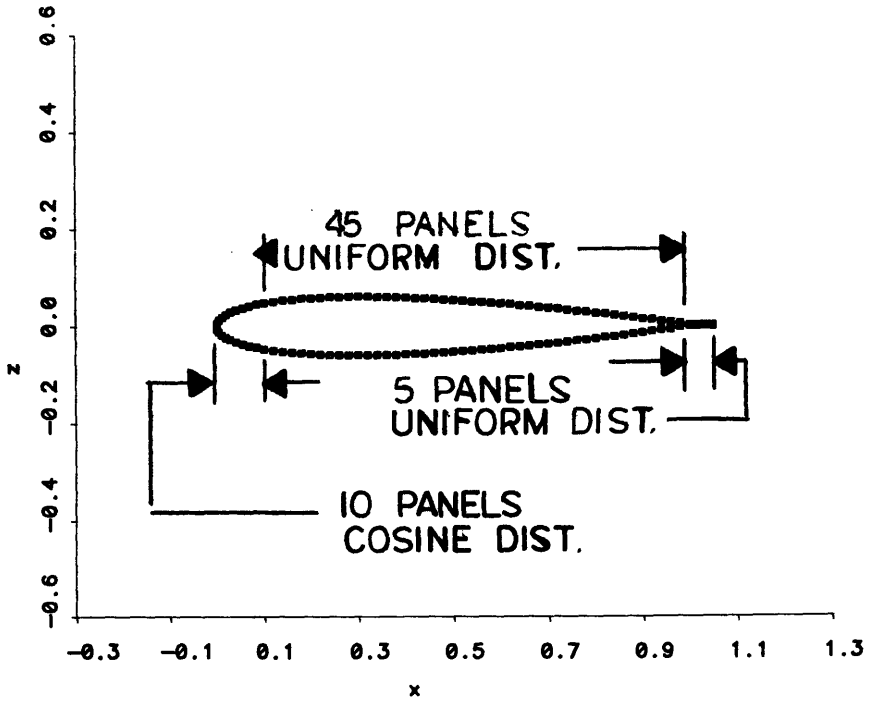

Figure 26: Final wing-wake panel configuration.

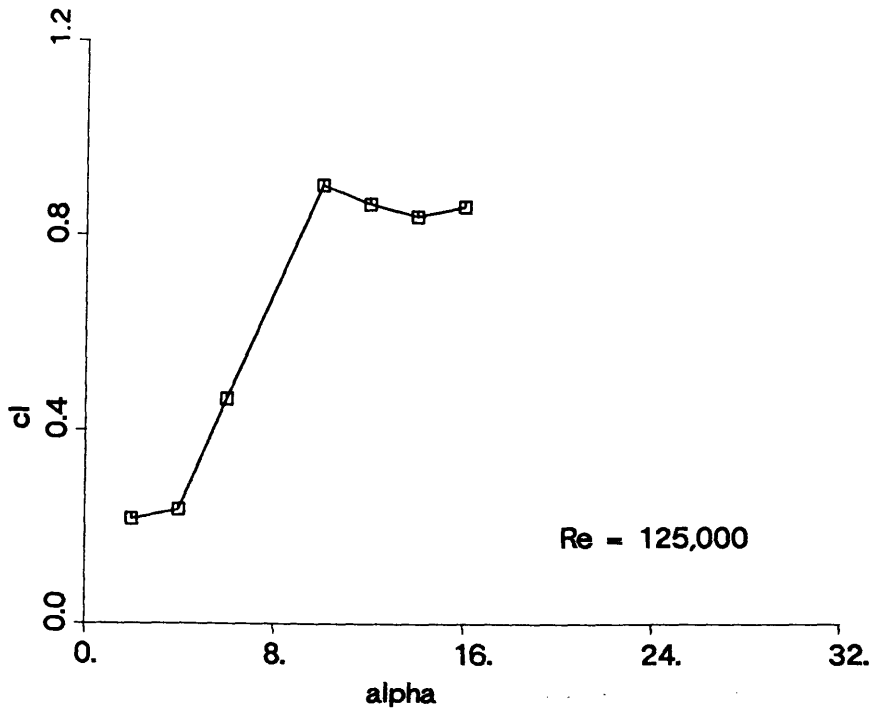

Figure 27: Predicted curve of lift coefficient, c_ℓ, versus angle-of-attack, NACA 0012, Re=125,000.

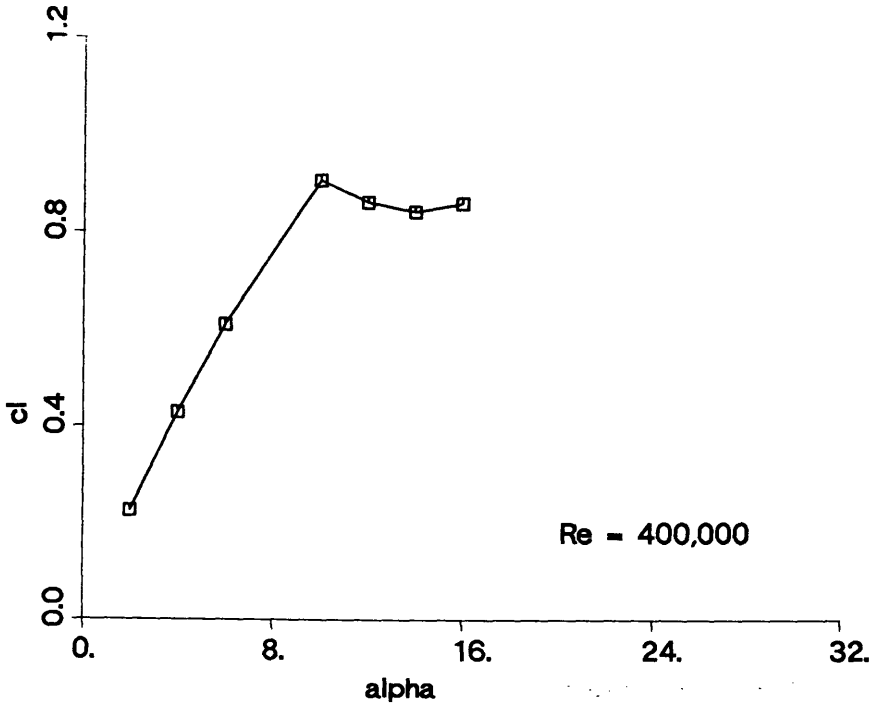

Figure 28: Predicted curve of lift coefficient, c_ℓ, versus angle-of-attack, NACA 0012, Re=400,000.

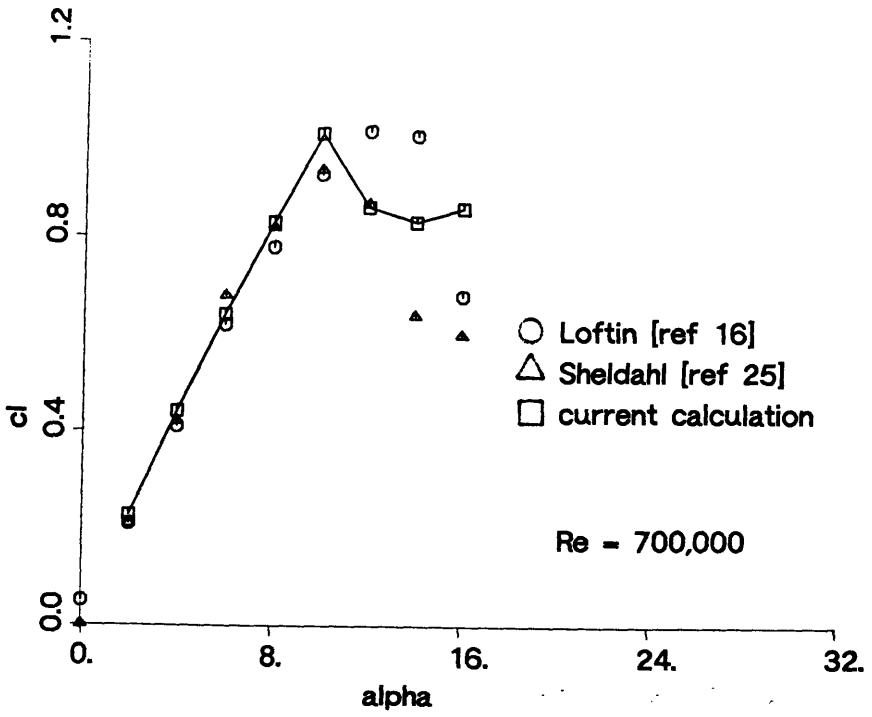

Figure 29: Predicted and experimental curves of lift coefficient, c_ℓ, versus angle-of-attack, NACA 0012, Re=700,000.

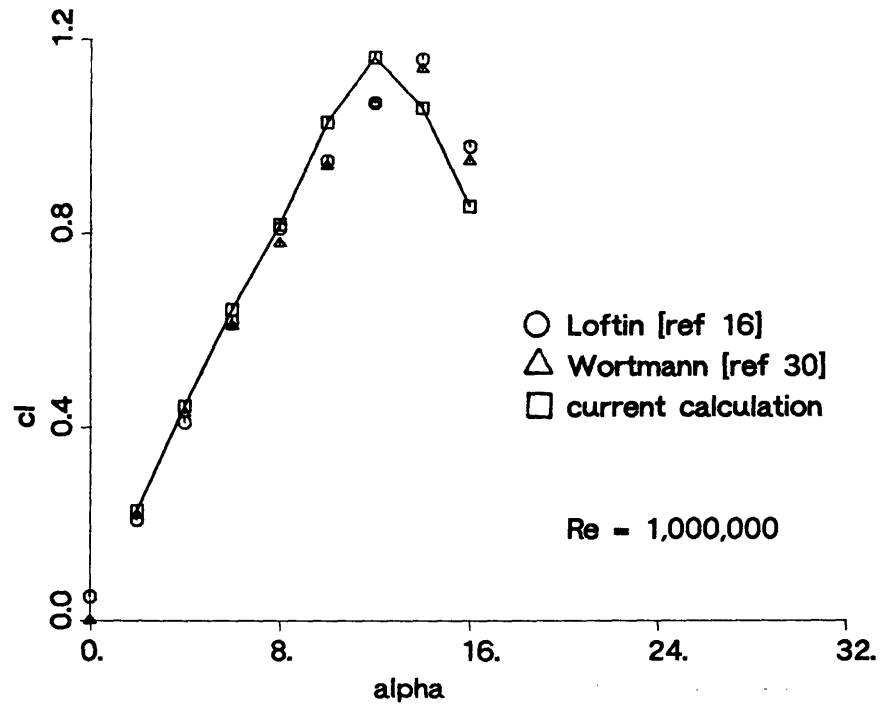

Figure 30: Predicted and experimental curves of lift coefficient, c_ℓ, versus angle-of-attack, NACA 0012, Re=1,000,000.

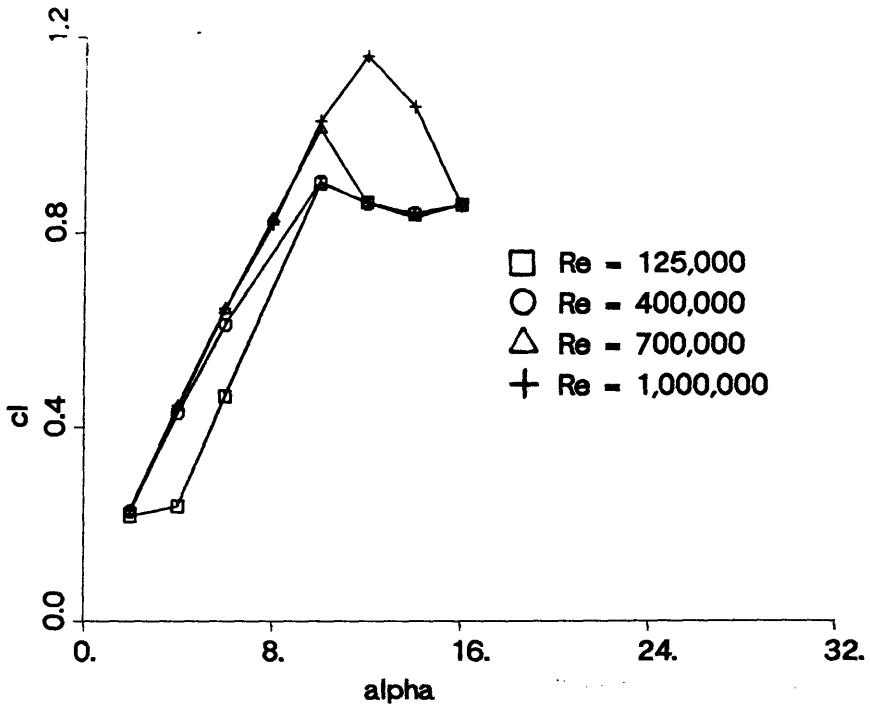

Figure 31: Predicted curves of lift coefficient, c_ℓ, versus AOA, NACA 0012, Re=125,000, 400,000, 7000,000 and 1,000,000.

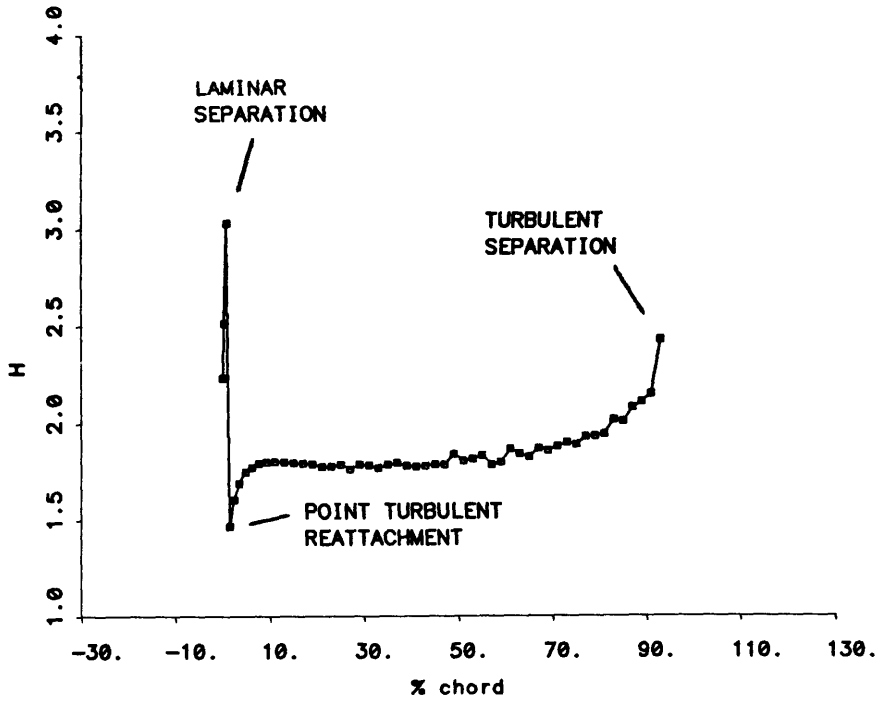

Figure 32: Chordwise distribution of shape factor, H, NACA 0012, AOA= 10°, Re=700,000.

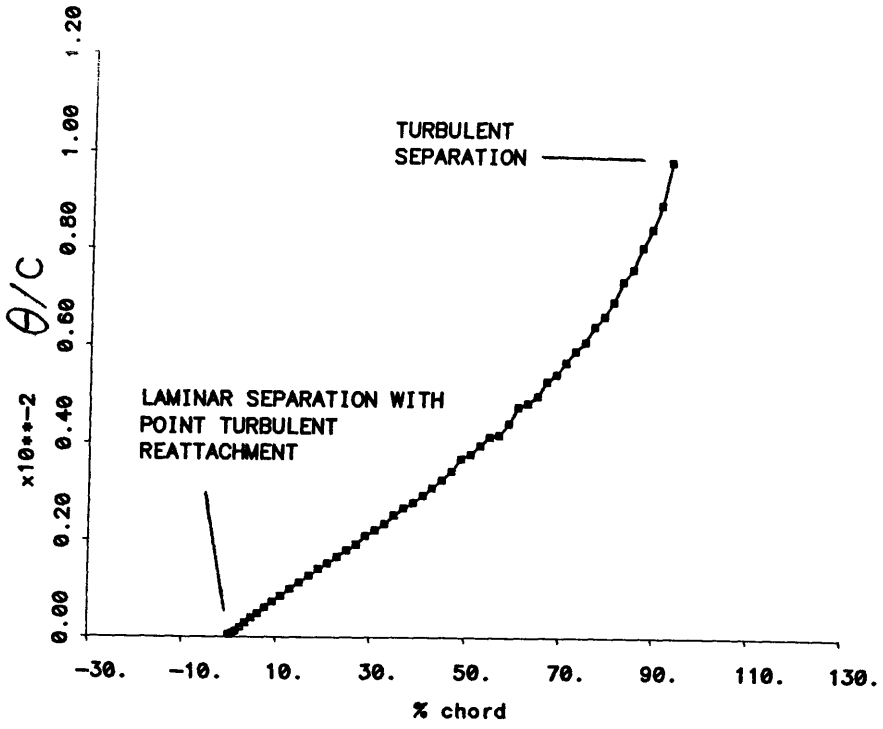

Figure 33: Chordwise distribution of momentum thickness, θ, NACA 0012, AOA= 10°, Re=700,000.

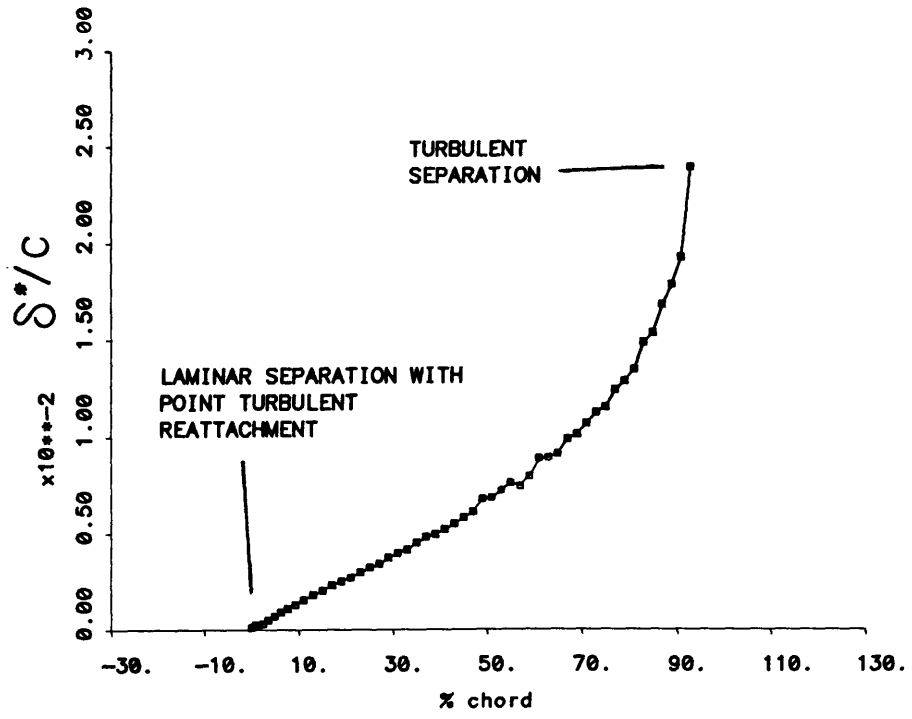

Figure 34: Chordwise distribution of displacement thickness, δ^*, NACA 0012, AOA= 4°, Re=700,000.

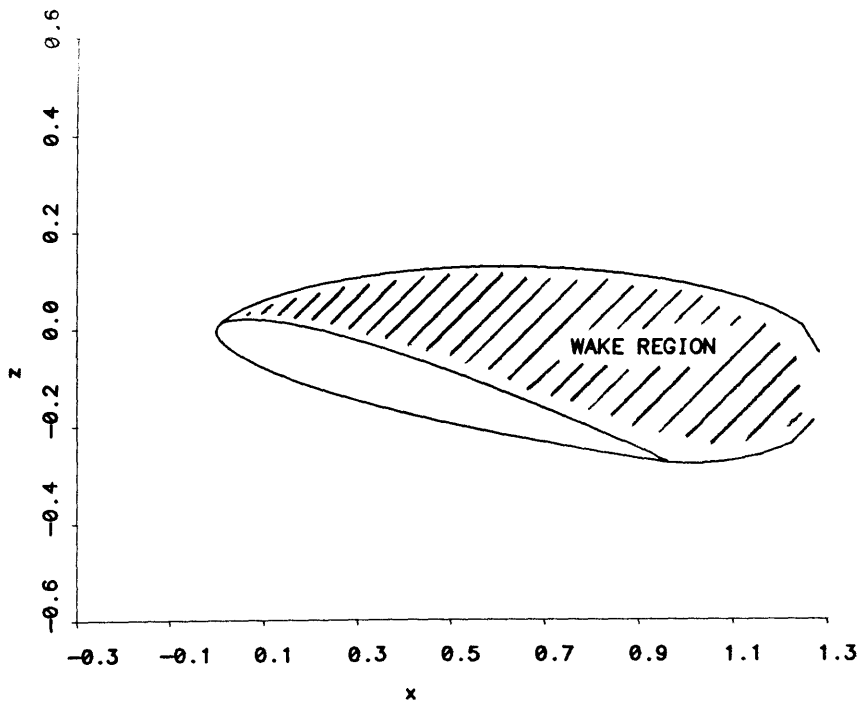

Figure 35: Wake shape, NACA 0012, AOA= 16°, Re=700,000.

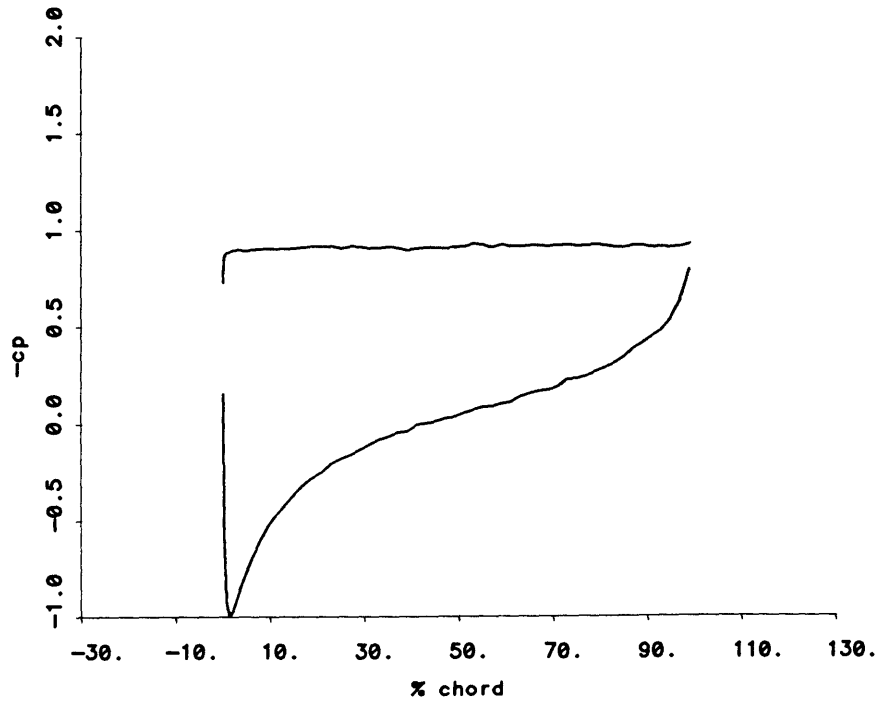

Figure 36: Pressure distribution, NACA 0012, AOA= 16°, Re=700,000.

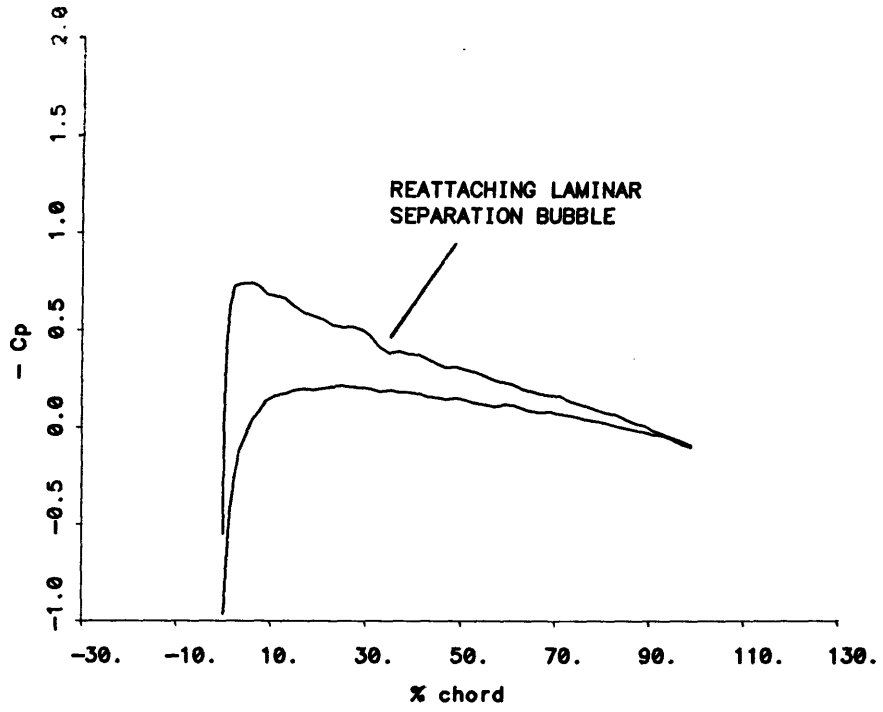

Figure 37: Effect of reattaching laminar separation bubble on pressure distribution, NACA 0012, AOA= 2°, Re=700,000.

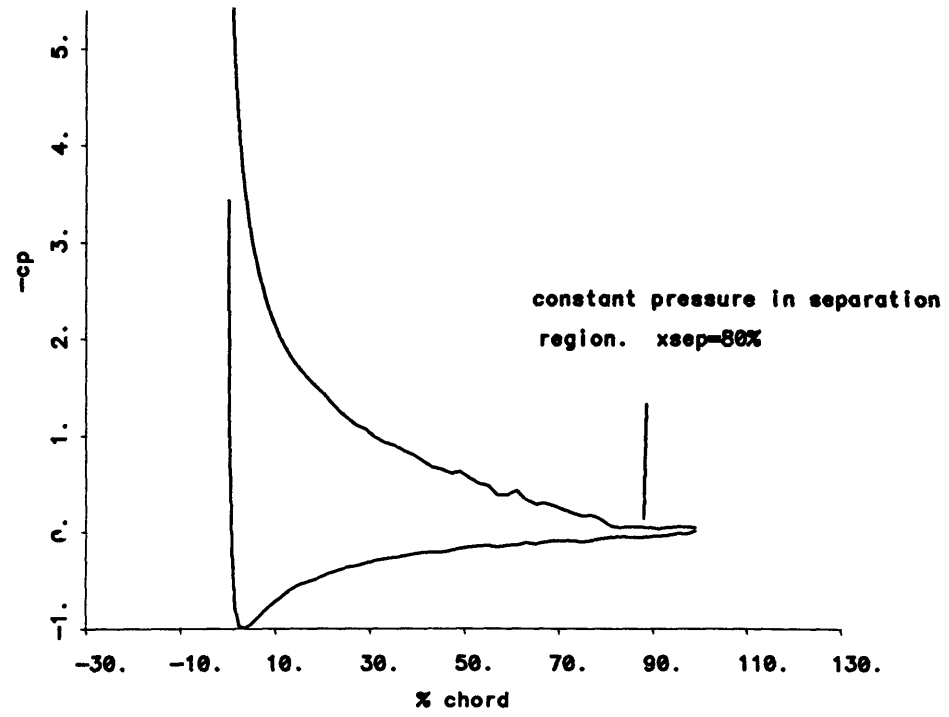

Figure 38: Pressure distribution with trailing edge separation, NACA 0012, AOA= 12°, Re=1,000,000.

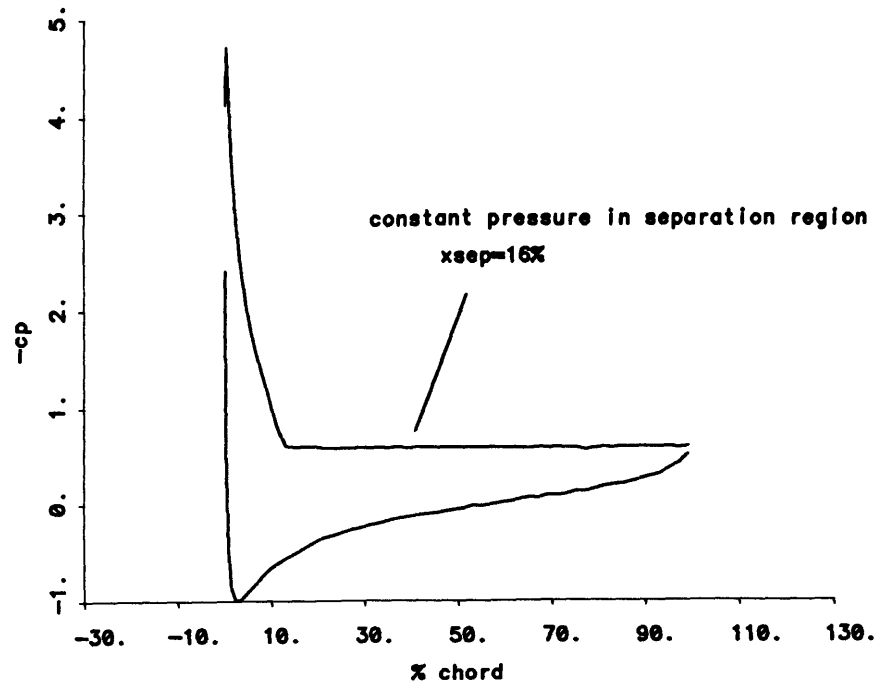

Figure 39: Pressure distribution with leading edge separation, NACA 0012, AOA= 16°, Re=1,000,000.

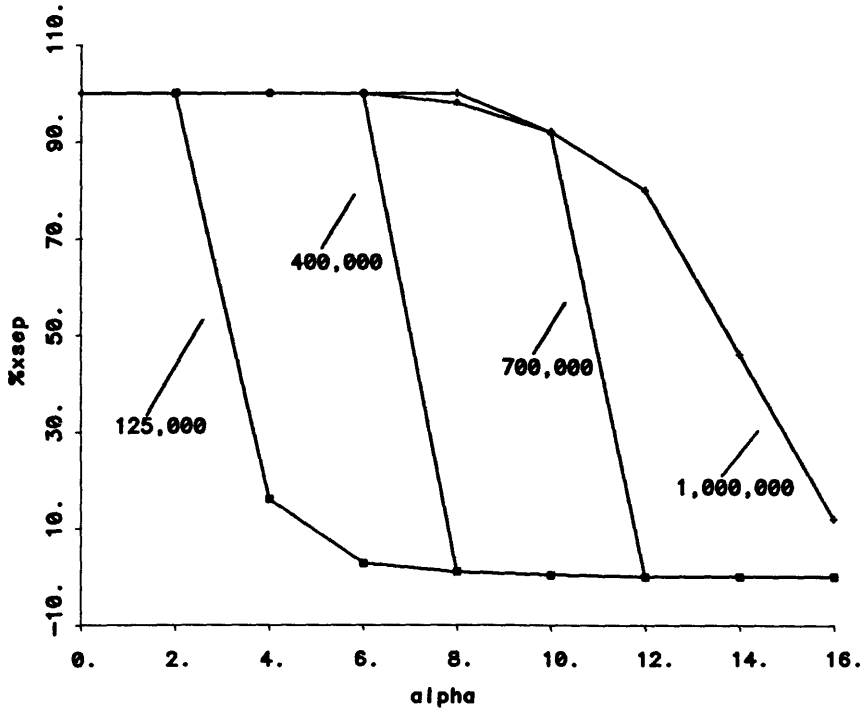

Figure 40: Chordwise separation location, x_{sep}, versus angle-of-attack as a function of Reynolds number, NACA 0012.

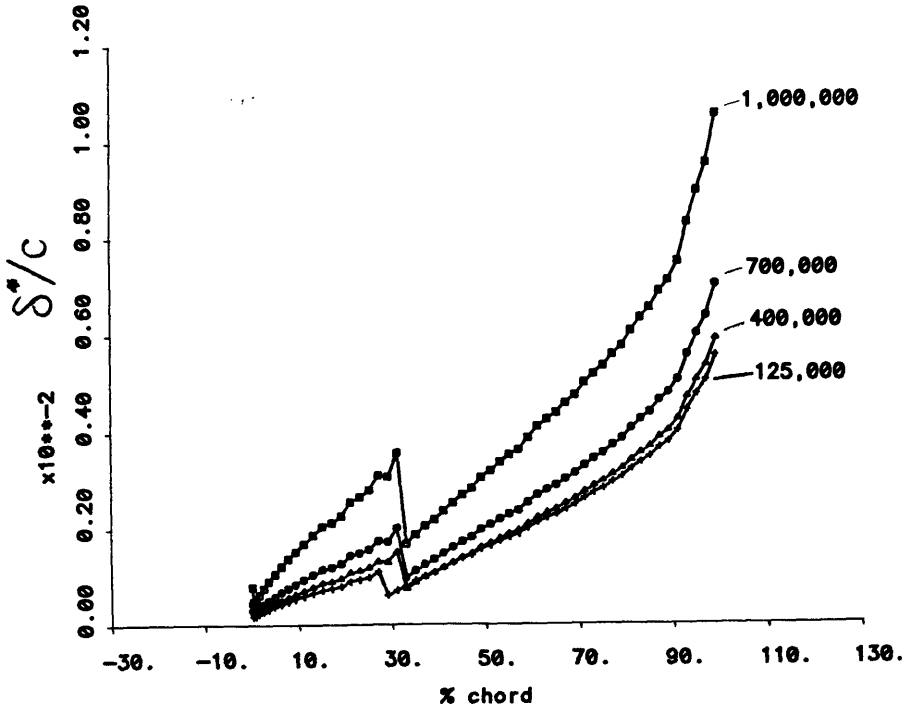

Figure 41: Distribution of displacement thickness, δ^*, as a function of Reynolds number, NACA 0012, AOA= 2°.

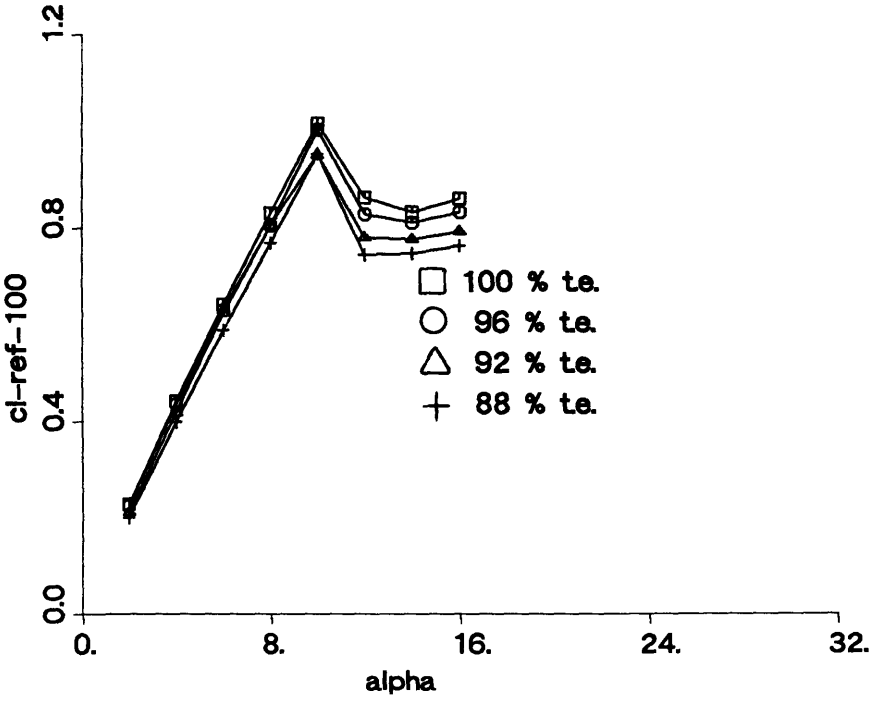

Figure 42: Lift coefficient, $[c_\ell]_{ref-100}$, (referenced to full section) versus AOA as a function of trailing edge bluntness, NACA 0012 reference, Re=700,000.

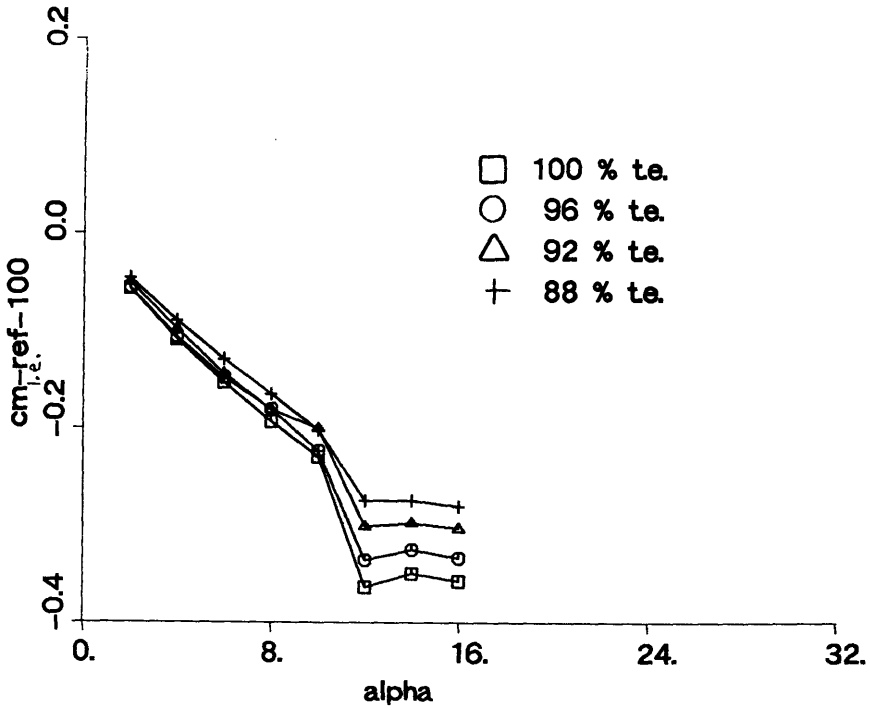

Figure 43: Moment coefficient, $[c_{m_{l.e.}}]_{ref-100}$, (referenced to full section) versus AOA as a function of trailing edge bluntness, NACA 0012 reference, Re=700,000.

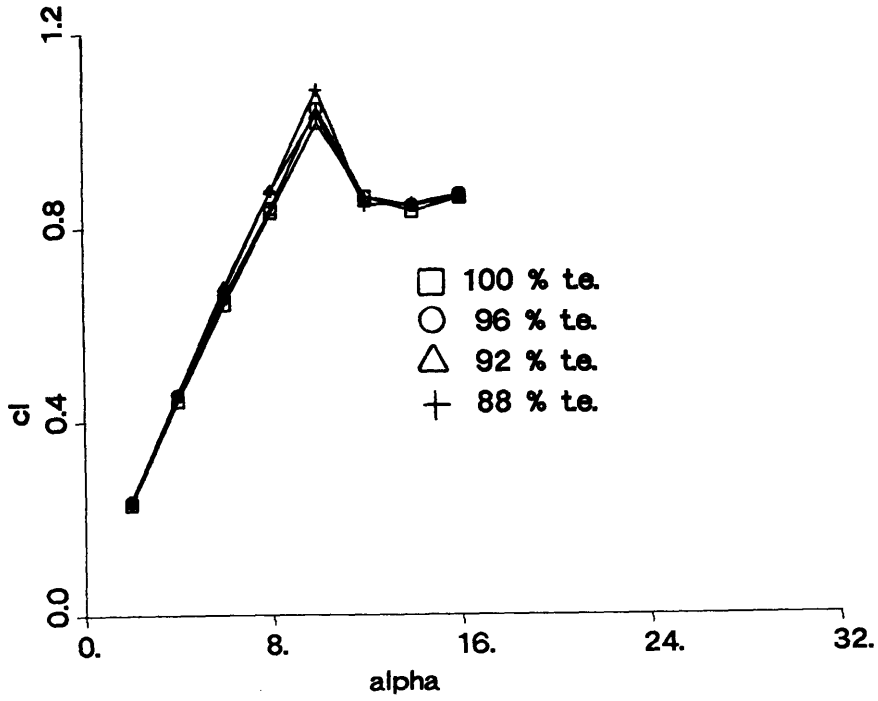

Figure 44: Lift coefficient, c_ℓ, (referenced to reduced chord) versus AOA as a function of trailing edge bluntness, NACA 0012 reference, Re=700,000.

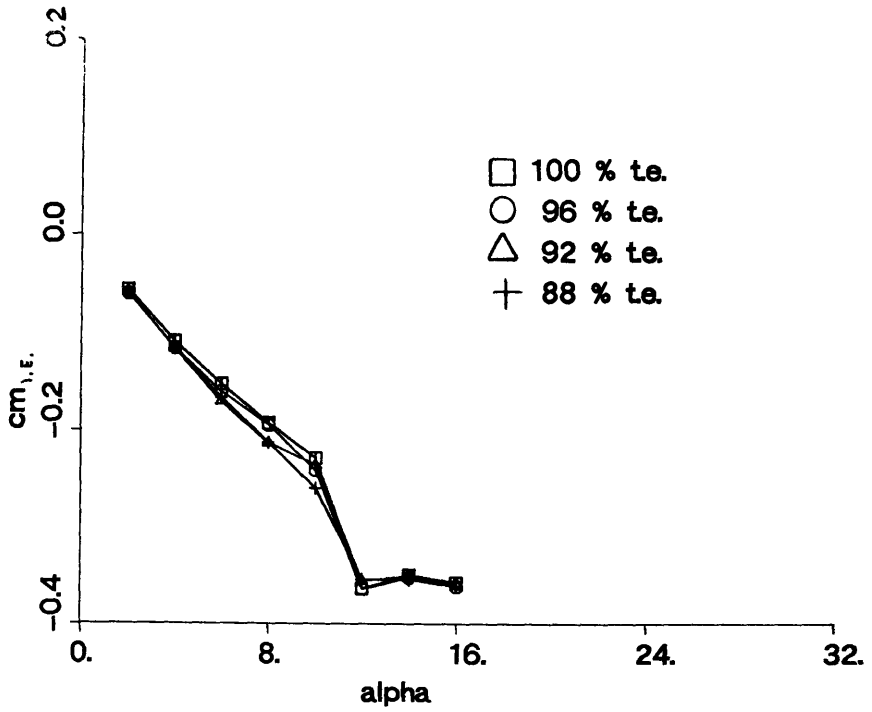

Figure 45: Moment coefficient, $c_{m_{l.e.}}$, (referenced to reduced chord) versus AOA as a function of trailing edge bluntness, NACA 0012 reference, Re=700,000.

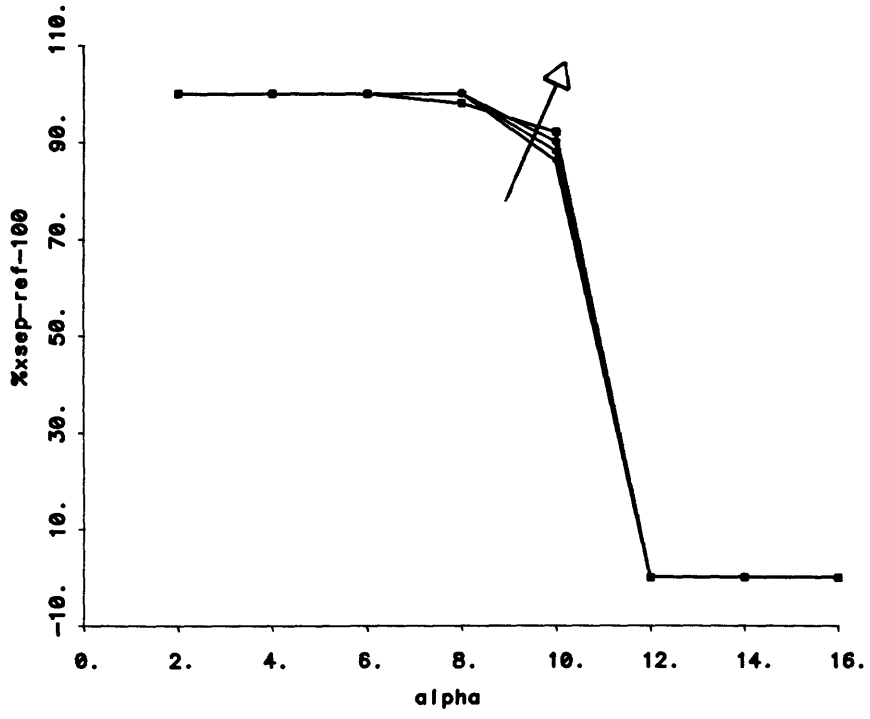

Figure 46: Separation location, $x[_{sep}]_{ref-100}$, (referenced to full section) versus AOA as a function of trailing edge bluntness, NACA 0012 reference, Re=700,000.

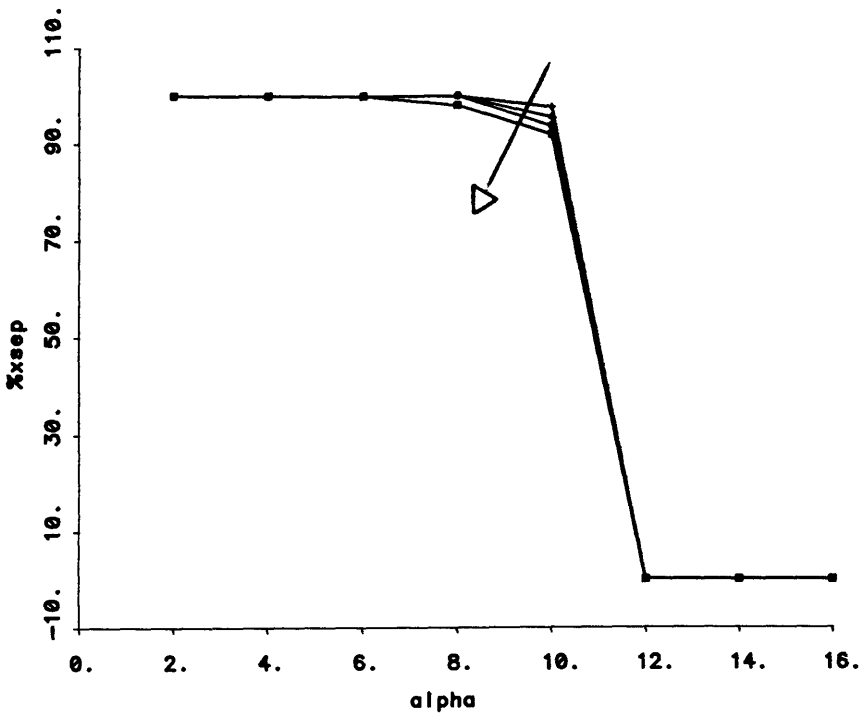

Figure 47: Separation location, x_{sep}, (referenced to actual reduced chord) versus AOA as a function of trailing edge bluntness, NACA 0012 reference, Re=700,000.

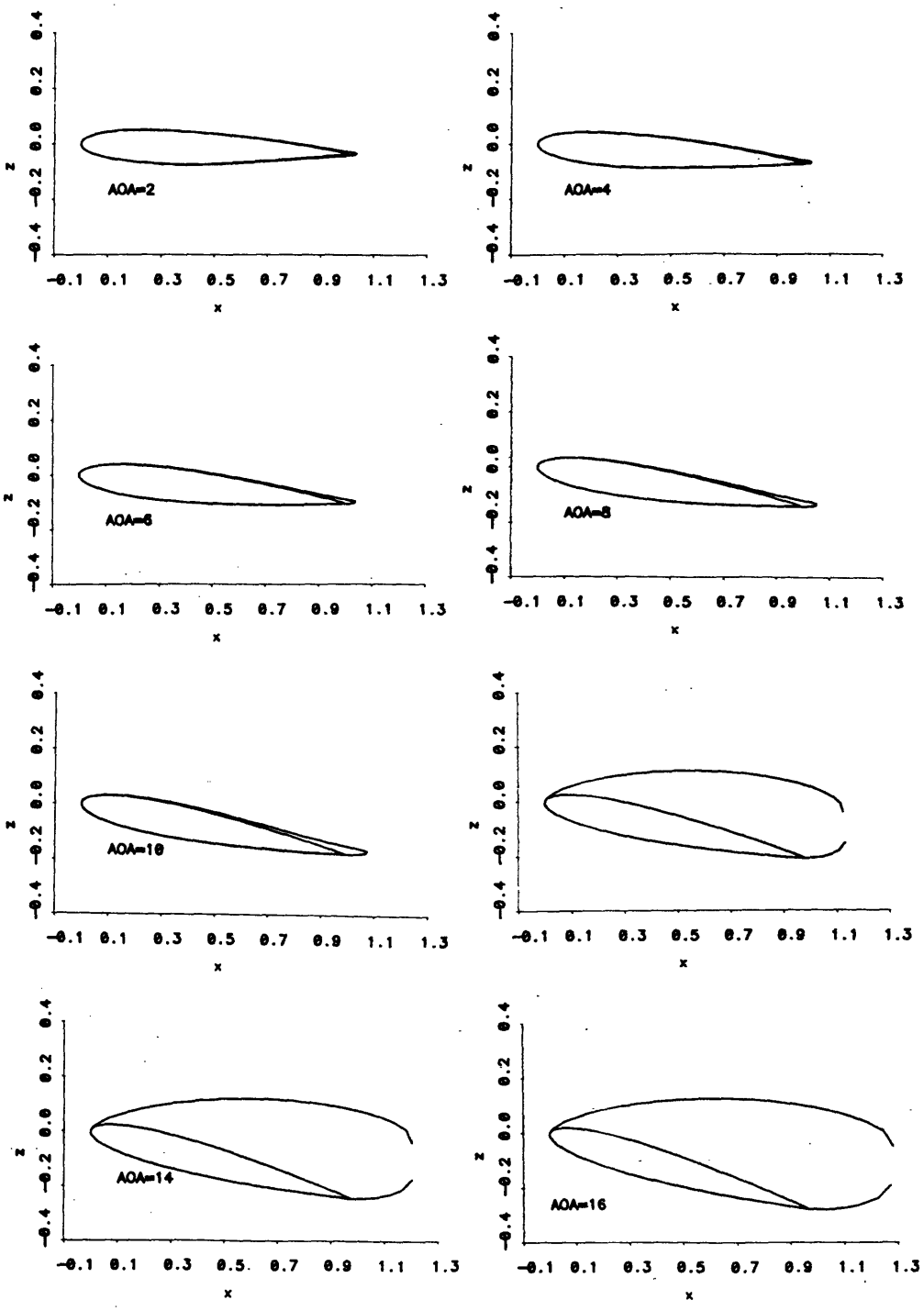

Figure 48: Wake shapes, NACA 0012, Re=700,000, AOA= 2° - 16°.

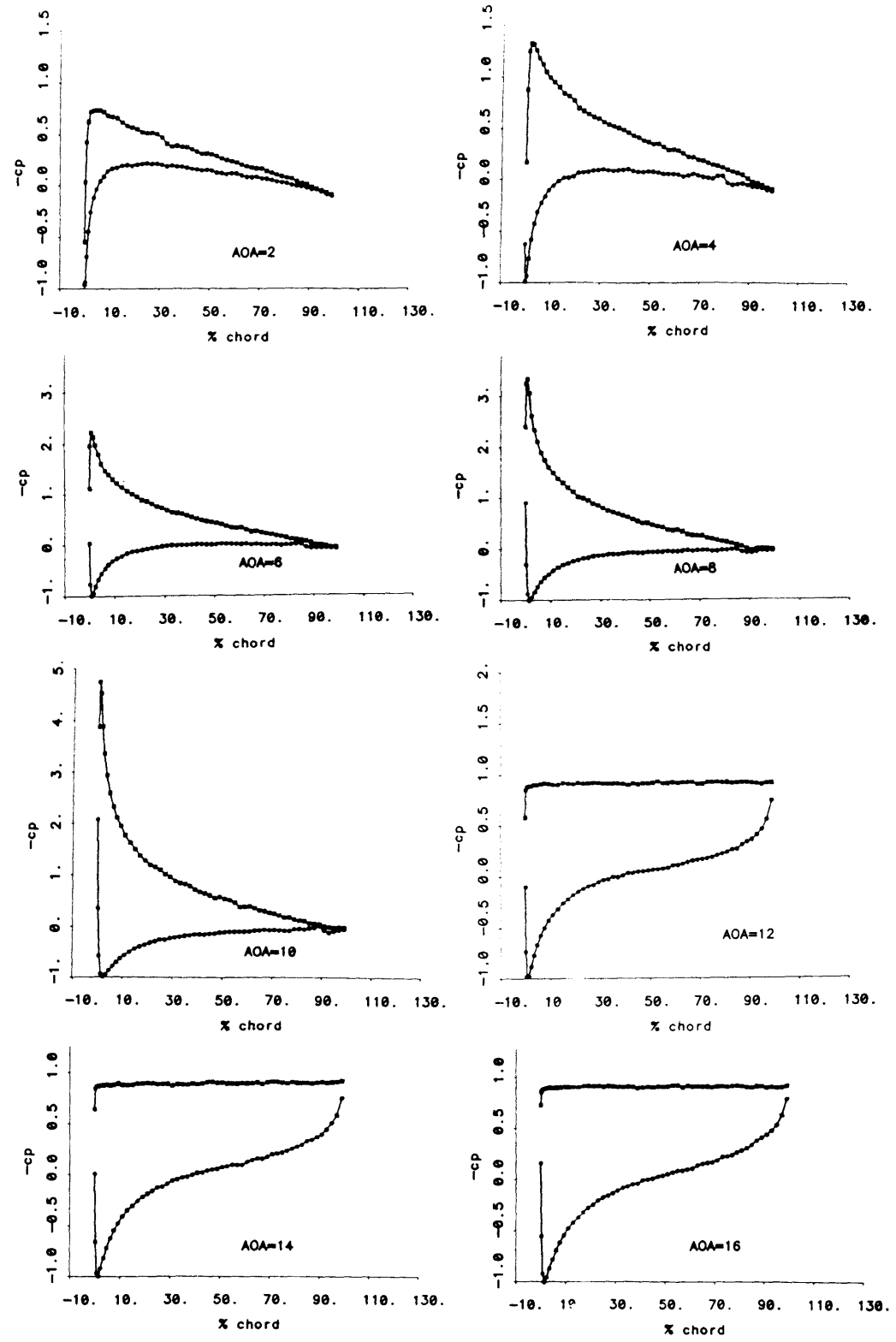

Figure 49: Pressure distributions, $c_p(x)$, NACA 0012, Re=700,000, AOA= 2° - 16°.

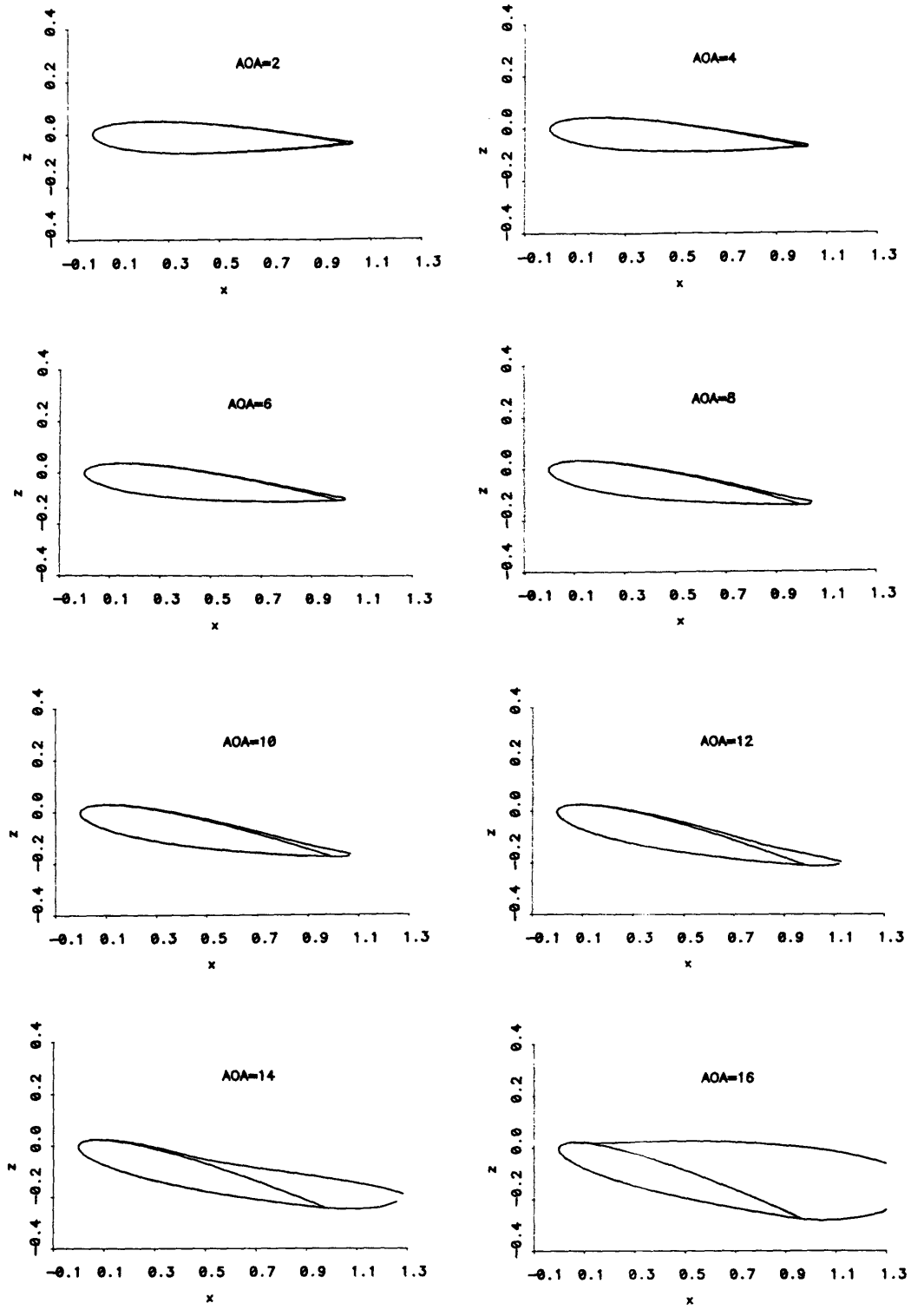

Figure 50: Wake shapes, NACA 0012, Re=1,000,000, AOA= 2° - 16°.

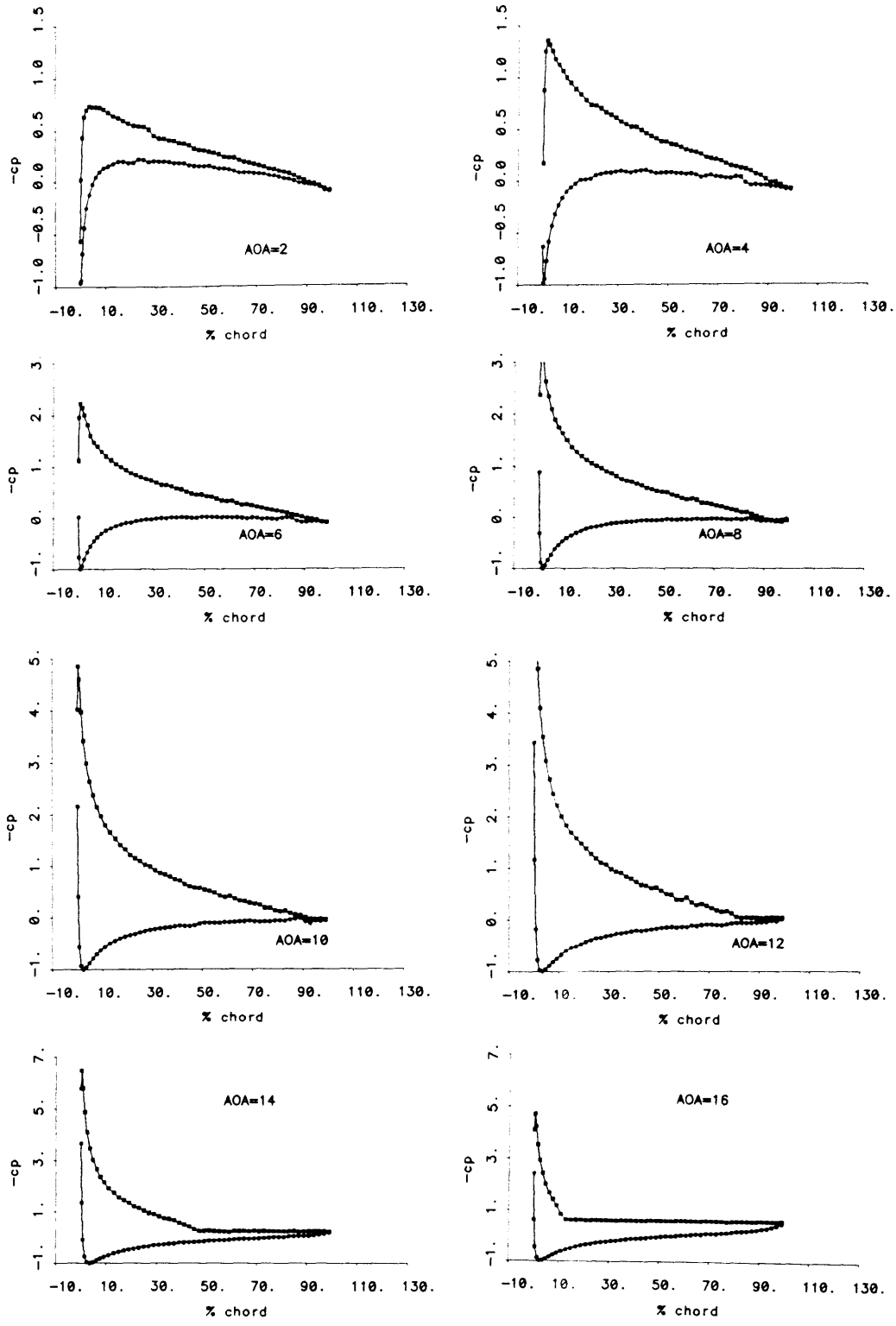

Figure 51: Pressure distributions, $c_p(x)$, NACA 0012, Re=1,000,000, AOA= 2° - 16°.

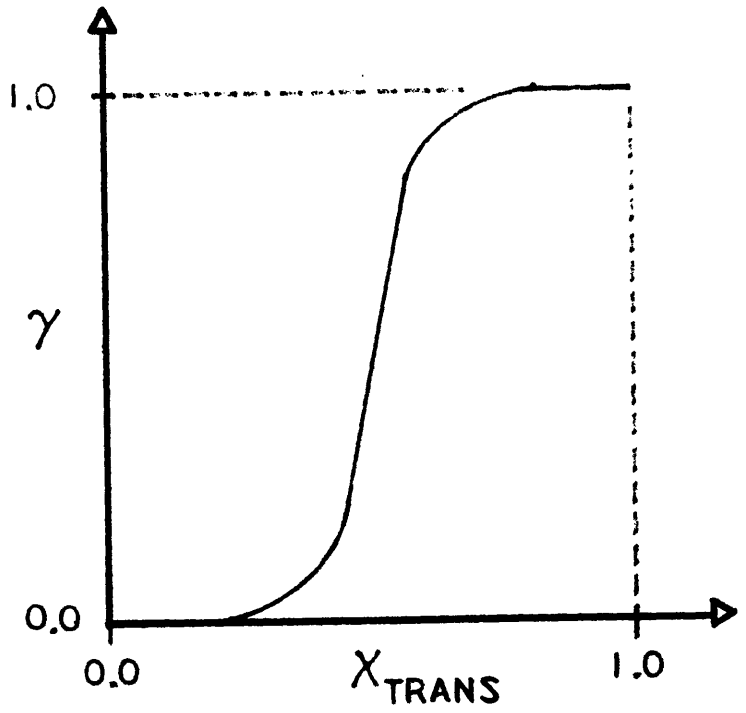

Figure 52: Laminar-Turbulent intermittency function, γ, for proposed transition model.

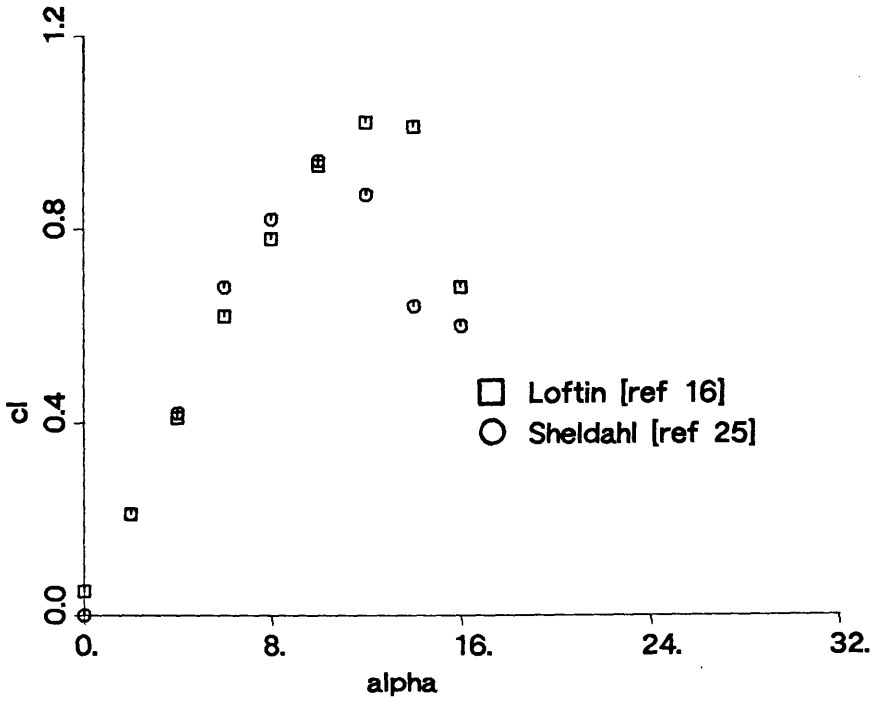

Figure 53: Experimental curves of lift coefficient, c_ℓ, versus angle-of-attack, NACA 0012, Re=700,000, from references [13] and [21].

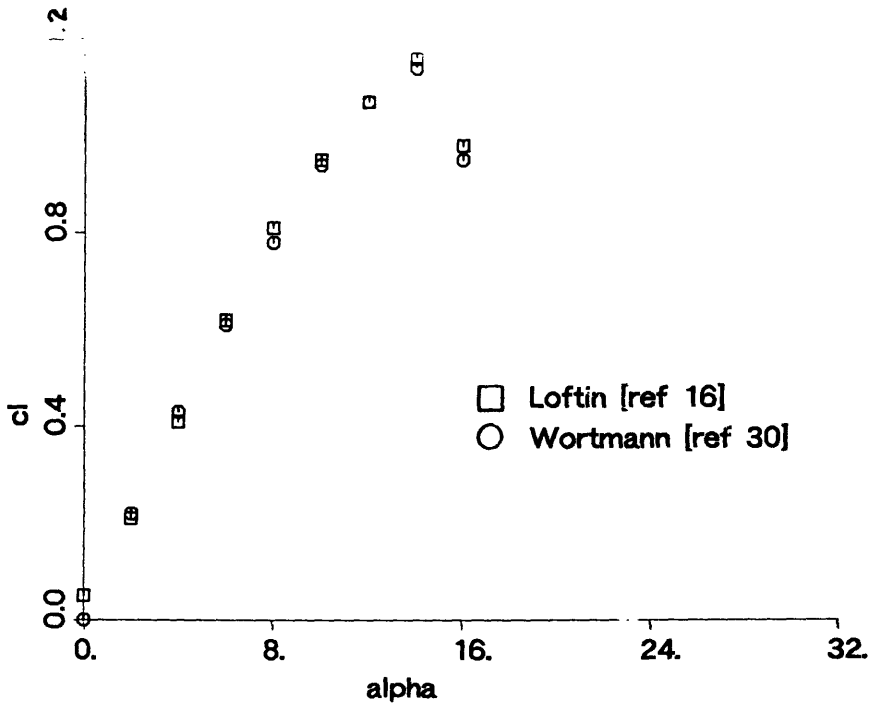

Figure 54: Experimental curves of lift coefficient, c_ℓ, versus angle-of-attack, NACA 0012, Re=1,000,000, from references [13] and [30].

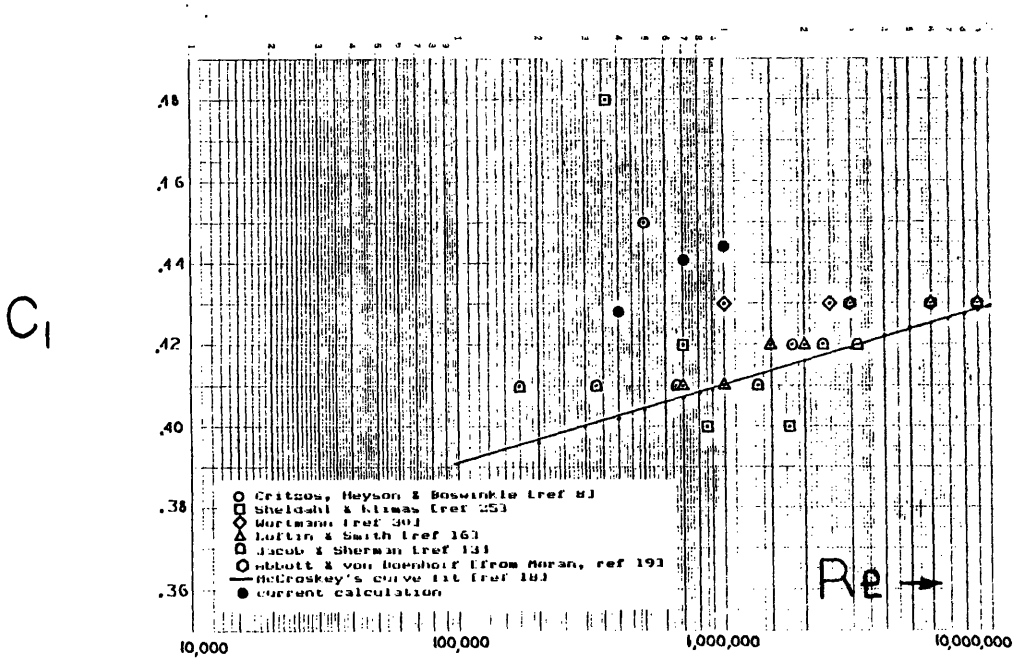

C_l

Figure 55: Lift coefficient, c_ℓ, versus Reynolds number, NACA 0012, AOA= 4°, sources as specified.

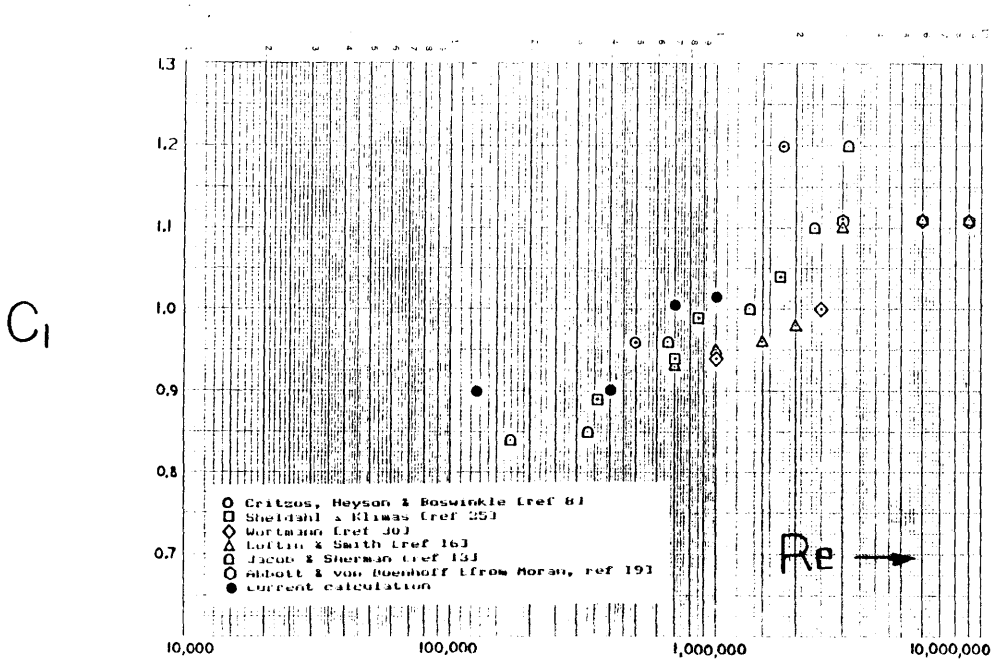

Figure 56: Lift coefficient, c_ℓ, versus Reynolds number, NACA 0012, AOA= 10°, sources as specified.

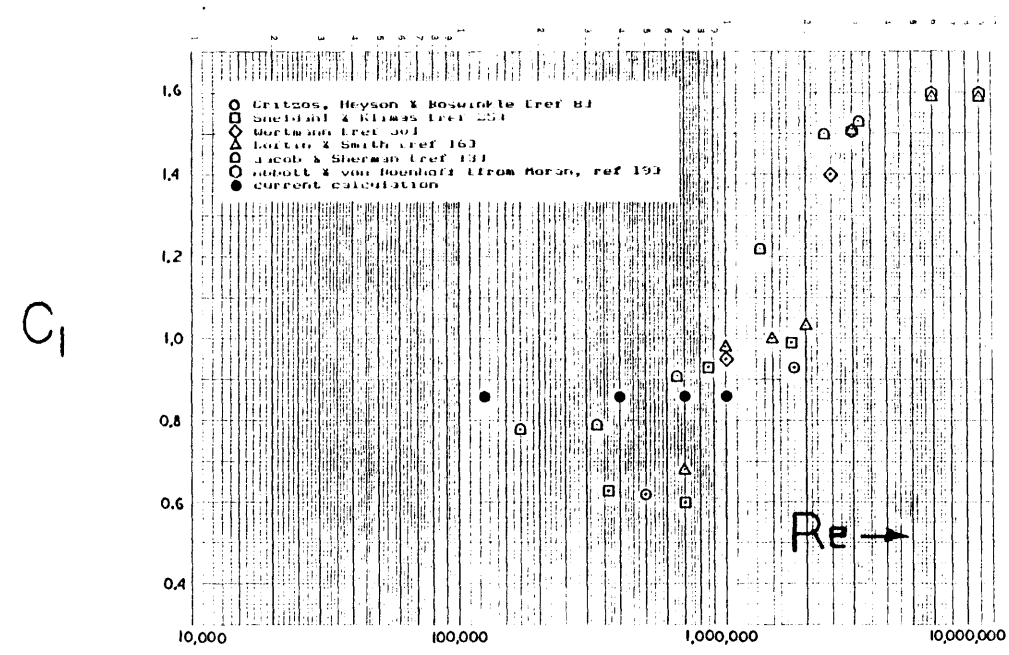

Figure 57: Lift coefficient, c_ℓ, versus Reynolds number, NACA 0012, AOA= 16°, sources as specified.

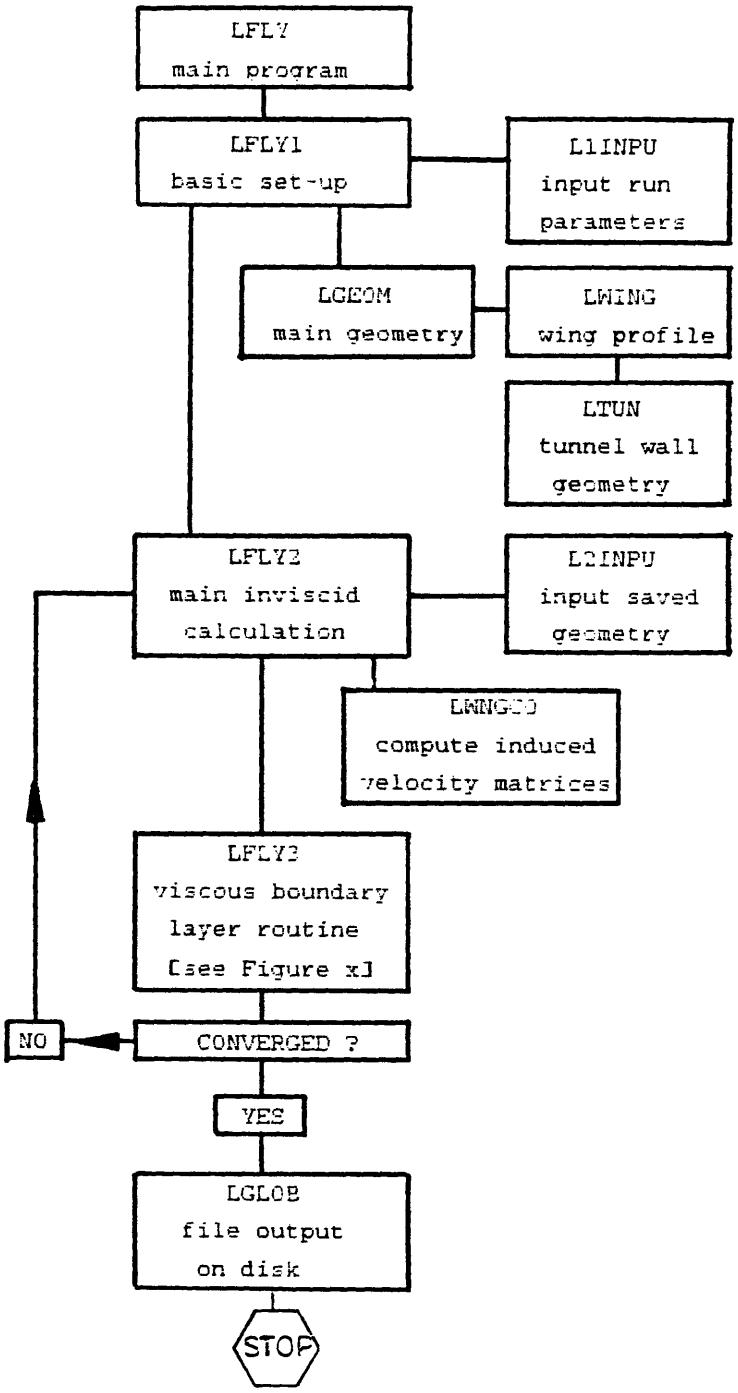

Figure 58: Flow chart of global viscid-inviscid flow model.

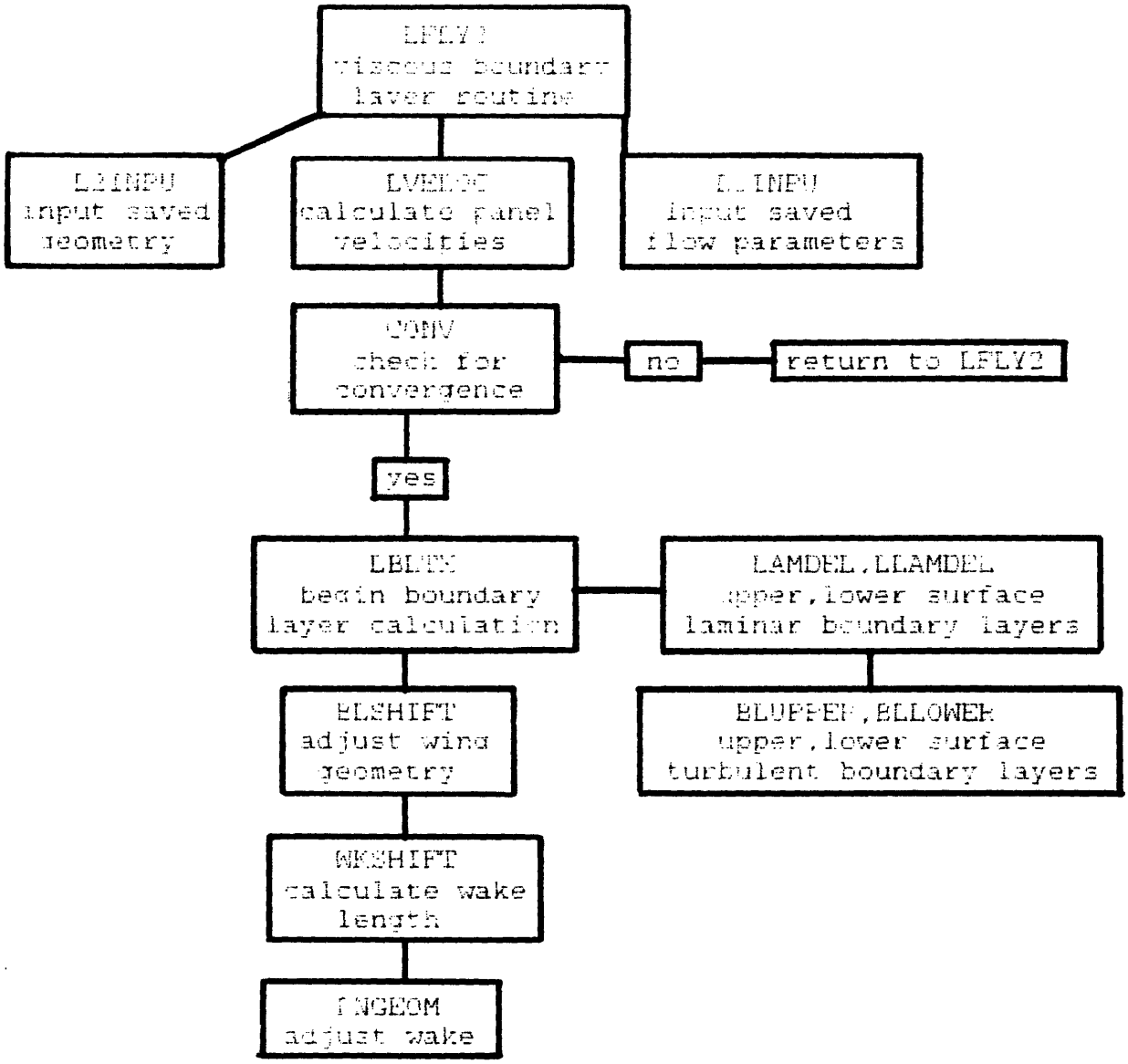

Figure 59: Flow chart of boundary layer routine.